Università degli Studi di Padova
Centro interdipartimentale "Centro Ricerche Fusione"

Universidade de Lisboa
Instituto Superior Técnico (IST)

JOINT RESEARCH DOCTORATE IN FUSION SCIENCE AND ENGINEERING
Cycle XXVIII

Study of plasma-wall interaction by fast cameras and numerical models

Coordinator: Prof. Paolo Bettini
Supervisors: Prof. Leonardo Giudicotti
Dr. Paolo Innocente

Doctoral student: Nicolò Visonà

Aut viam inveniam aut faciam.

Contents

Contents **v**

Abstract **ix**

1 Magnetically confined fusion plasma **1**
1.1 Thermonuclear fusion 1
1.2 Fusion plasma 3
1.2.1 Burning creteria 4
1.2.2 Magnetic confinement 7
1.2.2.1 MHD theory 8
1.2.2.2 MHD equilibrium and instability 10
1.2.3 Toroidal magnetic configurations 11
1.2.3.1 Tokamak 12
1.2.3.2 RFP 12
1.2.3.3 Stellarator 14
1.2.4 RFX-mod 15
1.2.5 The future of fusion: ITER 17

2 The plasma edge **20**
2.1 Edge configurations 20
2.1.1 Limiter 22
2.1.2 Divertor 23
2.2 The Scrape-Off Layer 24
2.3 Recycling 26
2.4 Asymmetries in the field at the edge: superthermal electrons . 28

3 Advanced divertor simulations **32**
3.1 Introduction 32

3.2 Snowflake divertor . . . 34
3.3 The simulation code . . . 36
3.3.1 EDGE2D . . . 37
3.3.2 EIRENE . . . 40
3.4 Numerical simulations . . . 40
3.5 Data overview and main results . . . 42
3.6 Conclusions . . . 45

4 Plasma-wall interactions in the visible spectrum 48
4.1 Introduction . . . 48
4.2 Experimental setup . . . 50
4.2.1 LISA samples . . . 50
4.2.2 Camera setup . . . 53
4.2.3 Camera measurement formula . . . 55
4.2.4 Background and diffusion correction . . . 57
4.3 Results . . . 59
4.3.1 Analysis of recycling of different materials . . . 60
4.3.2 Estimate of neutrals path parallel to the wall . . . 64
4.4 Conclusions . . . 66

5 Infrared measurements 70
5.1 Introduction . . . 71
5.2 Infrared thermography . . . 71
5.2.1 The infrared spectrum . . . 71
5.2.2 Blackbody radiation emission . . . 72
5.2.3 Non-blackbody emission . . . 74
5.2.4 Thermographic measurements . . . 78
5.3 Inverse Heat Conduction Problem . . . 80
5.3.1 THEODOR code . . . 81
5.3.2 TtoP3D . . . 82
5.3.3 Validation of the software tools . . . 83
5.4 Experimental setup . . . 88
5.4.1 Samples . . . 89
5.4.2 Plasma conditions . . . 90
5.4.3 IR camera setup . . . 91
5.4.4 IR camera calibration . . . 92
5.5 Data analysis . . . 95
5.5.1 Software tools integration . . . 96

5.5.2 Time synchronization 97
5.5.3 Magnetic reconstruction 98
5.5.4 Parallel heat flux properties 103
5.6 Results 105
5.6.1 Plasma position 110
5.6.2 Heat decay length 114
5.6.3 Heat fluxes 120
5.7 Conclusions 127

Conclusions **131**

Bibliography **138**

Abstract

The present thesis is the product of three years of research in the field on magnetically confined nuclear fusion, that has the ultimate goal of demonstrating the possibility of obtaining clean energy from fusion of light nuclei.

One of the current problems in this field deals with the interaction between the plasma and the wall of the containing device. Heat and particle fluxes impinging on the first wall can damage the machine structure and, on the other hand, particles expelled by plasma facing materials can degradate the performance and threat the very goal of reaching controlled fusion.

The activity carried out during the Ph.D. concerned the study of plasma-wall interactions, focusing on three main topics. The first was a numerical study of advanced magnetic configurations to mitigate heat load and power density deposited on the divertor plates of FAST, a tokamak proposed as a satellite experiment for ITER.

The following activity has ben done at RFX-mod, a Reversed-Field Pinch magnetic confinement experiment located in Padova, Italy. The plasma interaction with tungsten covered samples has been studied to investigate the

properties of the material for its possible employment in a machine upgrade. As last activity, heat fluxes of the plasma edge have been measured through the instertion of graphite samples in limiter configuration, measuring the heat decay length for the first time in an RFP.

The work is organized as follows.

Chapter 1 gives a general introduction to fusion plasmas, magnetic confinement and main toroidal configurations studied. A short presentation of RFX-mod is given along with a quick glance to ITER.

Chapter 2 gives a more detailed introduction to the topic of plasma edge, introducing concepts that are at the basis of the work presented later, as the divertor and the limiter configuration. Physical phenomena as recycling and superthermal electrons are also introduced here.

Chapter 3 describes numerical simulations in the framework of preliminary studies for the proposed FAST tokamak. A quasi-snowflake divertor configuration has been studied and compared against a standard divertor using the EDGE2D/EIRENE code.

Chapter 4 presents experimental measurements of surface properties of tungsten covered and full graphite samples. The activity was carried out at RFX-mod with a fast visible camera that measured the samples interactions with the plasma and a comparative analysis has been performed.

Chapter 5 describes the investigation of heat flux properties of the plasma edge of the RFP through graphite samples inserted as limiters in the RFX-mod plasma. The measured temperature has been converted to

heat flux with two software tools, that have been benchmarked. Heat fluxes and the measured heat decay length have been analyzed and correlated with plasma parameters.

Conclusions are presented in the last chapter with an overview of possible future developments.

Prefazione

La tesi presentata è il risultato di tre anni di ricerca nel settore della fusione nucleare a confinamento magnetico, che ha come obiettivo di dimostrare la possibilità di ottenere energia pulita dalla fusione di atomi leggeri.

Uno dei problemi attuali in questo campo riguarda l'interazione tra il plasma e la parete del dispositivo che lo contiene. Infatti i carichi termici e i flussi di particelle che incidono sulla prima parete possono danneggiare la struttura della macchina e, d'altra parte, le particelle rilasciate dai materiali che si affacciano al plasma possono influire negativamente sulle prestazioni e sul raggiungimento stesso dell'obiettivo della fusione controllata.

L'attività svolta durante il periodo del dottorato di ricerca si è concentrata sullo studio dell'interazione plasma-parete, focalizzandosi su tre argomenti principali. Il primo è stato uno studio numerico di configurazioni magnetiche avanzate per ridurre sia l'intensità che la densità del flusso di calore incidente sul divertore di FAST, un tokamak proposto come esperimento satellite di ITER.

Successivamente l'attività è stata svolta su RFX-mod, un'esperimento

situato a Padova di confinamento magnetico in configurazione Reversed-Field Pinch. Si è studiata sperimentalmente l'interazione del plasma con dei provini ricoperti di tungsteno per analizzare le proprietà di questo materiale e valu-tarne il possibile impiego per future modifiche dell'esperimento. Come ultima attività sono stati misurati i flussi termici nel bordo del plasma tramite l'inserimento di campioni di grafite in configurazione limiter, misurando la lunghezza di decadimento del calore per la prima volta in un RFP.

Il lavoro è presentato come segue.

Il **Capitolo 1** dà un'introduzione generale ai plasmi da fusione, al confinamento magnetico e alle principali configurazioni toroidali studiate. Viene fatta una breve introduzione a RFX-mod insieme ad uno sguardo a ITER.

Il **Capitolo 2** fornisce un'introduzione all'argomento del bordo plasma, introducendo concetti che sono alla base del lavoro presentato di seguito, come le configurazioni di divertore e limiter. Sono anche introdotti fenomeni fisici come il riciclaggio e gli elettroni sopratermici.

Il **Capitolo 3** descrive le simulazioni numeriche fatte nel contesto di studi preliminari per il tokamak proposto FAST. Una configurazione quasi-snowflake è stata studiata e confrontata a una di divertore standard usando il codice EDGE2D/EIRENE.

Il **Capitolo 4** presenta misure sperimentali di proprietà superficiali di provini ricoperti di tungsteno e di pura grafite. L'attività è stata svolta a RFX-mod con una telecamera veloce nel visibile che ha misurato le interazioni con il plasma ed è stata svolta un'analisi comparativa.

Il **Capitolo 5** descrive l'indagine sulle proprietà del flusso di calore del bordo del plasma di un RFP attraverso l'inserimento di campioni di grafite in configurazione limiter nel plasma di RFX-mod. La temperatura misurata è stata convertita in flusso termico da due software che sono stati standardizzati. I flussi termici e la lunghezza di decadimento del calore misurata sono stati analizzati e correlati con i parametri di plasma.

Le **Conclusioni** sono presentate nell'ultimo capitolo insieme ad una panoramica sui possibili sviluppi futuri.

Chapter 1

Magnetically confined fusion plasma

1.1 Thermonuclear fusion

Nuclear fusion happens when two light nuclei collide to form a heavier one, releasing energy and other particles: the output energy is the difference between the binding energy of the product nucleus and the starting ones. For such a reaction to happen, the light nuclei must have enough kinetic energy to overcome the Coulombian repulsive barrier between them which, increasing as Z^2, makes the lightest nuclei the most suitable for this purpose. The main reactions are:

$$ {}^{2}_{1}\mathrm{D} + {}^{2}_{1}\mathrm{D} \rightarrow {}^{3}_{1}\mathrm{T}(1.0\mathrm{MeV}) + \mathrm{p}(3.0\mathrm{MeV}) \tag{1.1.1} $$

$$ {}^{2}_{1}\mathrm{D} + {}^{2}_{1}\mathrm{D} \rightarrow {}^{3}_{2}\mathrm{H}(0.8\mathrm{MeV}) + \mathrm{n}(2.5\mathrm{MeV}) \tag{1.1.2} $$

$$ {}^{2}_{1}\mathrm{D} + {}^{3}_{1}\mathrm{T} \rightarrow {}^{4}_{2}\mathrm{He}(3.5\mathrm{MeV}) + \mathrm{n}(14.1\mathrm{MeV}) \tag{1.1.3} $$

$$ {}^{2}_{1}\mathrm{D} + {}^{3}_{2}\mathrm{He} \rightarrow {}^{4}_{2}\mathrm{He}(3.6\mathrm{MeV}) + \mathrm{p}(14.7\mathrm{MeV}) \tag{1.1.4} $$

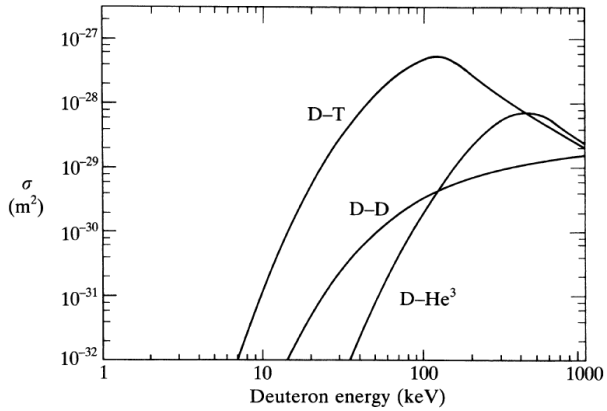

Figure 1.1.1: Cross-sections and energy threasholds of typical laboratory fusion reactions

In fig.1.1.1 the cross section of the above reactions as a function of the energy is displayed, showing that the D-T reaction is the one with the highest cross section at any energy, thus being the most suitable candidate for a fusion reactor. Deuterium is spread in nature and is a non-exhaustible resource since the 0.015% of all hydrogen atoms are actually deuterium. Tritium instead is an unstable isotope with a relatively short radioactive half-time of 12.3

years, but fortunately it can be obtained from lithium by these reactions:

$$ {}^{6}_{3}\mathrm{Li} + {}^{1}_{0}\mathrm{n} \rightarrow {}^{4}_{2}\mathrm{He} + {}^{3}_{1}\mathrm{T} + 4.8\mathrm{MeV} \tag{1.1.5} $$

$$ {}^{7}_{3}\mathrm{Li} + {}^{1}_{0}\mathrm{n} \rightarrow {}^{4}_{2}\mathrm{He} + {}^{3}_{1}\mathrm{T} + {}^{1}_{0}\mathrm{n} + 2.5\mathrm{MeV} \tag{1.1.6} $$

A lithium blanket is foreseen inside a fusion reactor to provide all the tritium necessary to the fusion reactions.

1.2 Fusion plasma

At the high temperatures involed in the D-T reactions, matter is in the plasma state. A plasma is a quasi-neutral ionized gas with high electrical conductivity and low collisionality[1, 2].

A quasi-neutral ionized gas is a gas where ions are separated from electrons but still global electrical neutrality is mainteined, although allowing local electrical fluctuations which spatial extent are smaller[3] then di *Debye length*, defined as:

$$ \lambda_D = \sqrt{\frac{\varepsilon_0 T_e}{n_e e^2}}, \tag{1.2.1} $$

where T_e is the electron temperature and $n_e$the density. These fluctuations are shielded by other charges in a time scale given by the plasma frequency, defined as:

$$\omega_p = \sqrt{\frac{n_e e^2}{m_e \varepsilon_0}}, \tag{1.2.2}$$

where $m_e$is the electron mass. In a plasma, the condition of high electrical conductivity is obtained by the condition that the Debye length must be much smaller than the typical macroscopic length of the plasma, so:

$$\lambda_D \ll L. \tag{1.2.3}$$

Low collisionality means that long range collective effects dominate over single particles coulombian interactions, which is translated into the fact that Λ_D, which is the number of particles in a sphere with radius λ_D, must be much grater than 1:

$$\Lambda_D = \frac{4\pi}{3} \frac{\varepsilon_0^{3/2} T_e^{3/2}}{n_e^{1/2} e^3} \gg 1. \tag{1.2.4}$$

1.2.1 Burning creteria

A fusion reactor should be a source of energy, so the plasma operation should have a positive energy balance, producing more energy from nuclear reactions than that consumed. Such an energy balance can be written as a function of the power coming from nuclear reactions P_n , the power lost by *bremmstrahlung* radiation P_b, the power lost by trasport mechanisms P_t, and the energy conversion efficiency η, as:

$$P_b + P_t \leq \eta(P_b + P_t + P_n). \tag{1.2.5}$$

Converting this balance in terms of specific plasma parameters, it is possible to obtain the *Lawson criterion*[4], which expresses the condition under which a fusion plasma is an energy production source:

$$n\tau_e \geq \left(\frac{\eta}{1-\eta} \frac{W_{D-T}}{4} < \sigma\upsilon >_T - b\sqrt{T} \right)^{-1}, \tag{1.2.6}$$

where τ_e is the particles confinement time, $W_{D-T} = 17.59MeV$ is the energy released from a D-T reaction, $< \sigma\upsilon >_T$is the average over the Maxwellian velocity distribution of the product of the reaction cross section and the reactants velocity, and b is a constant that depends on the effective charge Z_{eff}.

A more modern concept is that of plasma ignition. In this case, energy losses are balanced by the kinetic energy of the reactions products that is transferred to the plasma by collisions: α particles carry an energy of $3.5MeV$, while neutrons are not taken into account since they cannot be confined and escape the plasma. The new energy balance becomes:

$$P_b + P_t \leq P_\alpha \tag{1.2.7}$$

and the Lawson criterion becomes the *ignition criterion*:

$$n\tau_e \geq 3T \left(\frac{W_\alpha}{4} < \sigma\upsilon >_T - b\sqrt{T} \right)^{-1}, \tag{1.2.8}$$

W_α being the energy of a single α particle, thus $W_\alpha = W_{D-T}/5$.

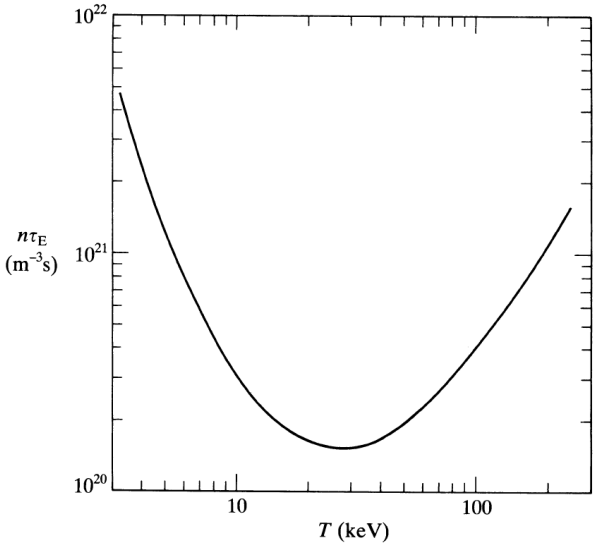

Figure 1.2.1: Dependence of the ignition curve from temperature

The ignition curve expressed by disequation 1.2.8 is plotted in fig. 1.2.1 as a function of temperature, where it is possible to see that it has a minimum for $T \simeq 20keV$. In an interval around this minimum, it is possible to rewrite the formula in the form of the *triple product*:

$$n\tau_e T \geq 3 \cdot 10^{21} m^{-3} s \cdot keV, \tag{1.2.9}$$

which is the present criterion for ignition, giving a condition for the plasma to be *confined enough* to yeld a bositive energy balance.

1.2.2 Magnetic confinement

On Earth there are only to ways to confine a fusion plasma with the caracteristics exposed so far: *inertial confinement* and *magnetic confinement*. In the first approach, a small D-T solid pellet is hit by high-power lasers which make it implode and create a high density plasma that last for times of the order of nanoseconds. In magnetic confinement, that is the framework of this work, the plasma is obtained by inducing a strong current in a low density gas and then confined by externally imposed electromagnetic fields.

Magnetic confinement origins from the Lorentz force experienced by an electric particle entering a uniform magnetic field, causing it to spin around the magnetic field line along a helical trajectory with Larmor radius:

$$r = \frac{mv_\perp}{|q|B} \tag{1.2.10}$$

and cyclotron frequency:

$$\omega = \frac{|q|B}{m}, \tag{1.2.11}$$

being m the particle mass, q its electrical charge, $v_\perp$its perpendicular velocity with respect to the magnetic field B. It is possible to see that the magnetic field has no effect on the velocity component parrallel to the field, $v_\parallel$.

At the beggining, a linear geometry was studied for magnetic confinement, giving rise to the zeta and theta pinch, but particles losses at the end

of the line were to large to allow fusion conditions. The problem was solved by binding the linear system into a toroidal one: end losses were removed altogether but the curved and non-uniform magnetic field introduced gave rise to important instabilities. The curvature of the field and its non-uniformity dive rise to a vertical drift:

$$v_d \propto \frac{1}{q}\frac{B \times \nabla B}{B^3} \tag{1.2.12}$$

which dependends on the charge and thus induced a charge separation between positive ions and electrons. This separation creates an electric field inside the plasma that in turn creates an outward drift:

$$v_{E\times B} = \frac{E \times B}{B^2} \tag{1.2.13}$$

that causes the plasma to be unstable in this configuration. This instability is overcome by introducing another component of the magnetic field perpendicular to the first one, namely a poloidal component, obtaining a twisted field.

1.2.2.1 MHD theory

The theoretical basis underneath plasma confinement is the *MagnetoHydroDinamic (MHD)*[2] theory, in particular the resistive MHD equations are used to describe a large number of macrosopic phoenomena. The plasma is treated as an electrically conducting fluid in a magnetic field and its behaviour is de-

scribed by the combination of the hydrodinamic equations and the Ohm's law, under the conditions of charge quasi neutrality, $n_i \approx n_e$, and that length scales larger than λ_D (eq. 1.2.1) and time scales larger than $1/\omega_p$(eq. 1.2.2). In this context, Maxwell's equations yeld the following set of equations for coninuity, motion, energy, induction and generalized Ohm's:

$$\frac{\partial \rho}{\partial t} + \nabla \cdot (\rho \mathbf{v}) = 0 \tag{1.2.14}$$

$$\rho \left(\frac{\partial \mathbf{v}}{\partial t} + \mathbf{v} \cdot \nabla \mathbf{v} \right) = \mathbf{j} \times \mathbf{B} - \nabla \mathbf{p} + \frac{1}{\mu_0 \eta} \mathbf{E} \tag{1.2.15}$$

$$\frac{\partial \epsilon}{\partial t} + \nabla \cdot (\epsilon \mathbf{v}) = -\mathbf{p} \nabla \cdot \mathbf{v} + \mu_0 \eta \mathbf{j}^2 + \nabla \cdot (k_B \nabla \mathbf{T}) \tag{1.2.16}$$

$$\frac{\partial \mathbf{B}}{\partial t} = \nabla \times (\mathbf{v} \times \mathbf{B}) + \frac{\eta}{\mu_0} \nabla^2 \mathbf{B} \tag{1.2.17}$$

$$\mathbf{E} + \mathbf{v} \times \mathbf{B} = \eta \mathbf{j} \tag{1.2.18}$$

where ρ is the fluid mass density, $\mathbf{v}$ the velocity, η the resistivity, $\mathbf{p}$ the pressure and ϵ the internal energy density. The generalized Ohm's law (eq. 1.2.18) has been already simplified ommitting negligible terms.

1.2.2.2 MHD equilibrium and instability

The equilibrium of a toroidal configuration is found from eq. 1.2.15 imposing plasma quasi neutrality in stationary $\left(\frac{\partial}{\partial t} = 0\right)$and static ($v = 0$) conditions, obtaining the equation that balances the magnetic force and the thermal expansion force, the so called *force-balance equation*:

$$\mathbf{j} \times \mathbf{B} = \nabla \mathbf{p}. \tag{1.2.19}$$

In toroidal geometry, this equation describes magnetic surfaces with constant pressure, since $\mathbf{B} \cdot \nabla \mathbf{p} = \mathbf{0}$, and parallel to the current density, since $\mathbf{j} \cdot \nabla \mathbf{p} = \mathbf{0}$. These surfaces are nested and the innermost (collapsed) one is the magnetic axis.

MHD theory predicts that instabilities can appear when one of the quantities involved in the MHD equations udergoes even small variations. There are different kinds of instabilities and some of them can grow and cause all the plasma to be unstable, becoming of real concern for plasma performance.

A perturbation $\tilde{\mathbf{A}}$ of a quantity $\mathbf{A}$ in a toroidal plasma can be written in its Fourier components as:

$$\tilde{\mathbf{A}}(r,t) = \sum_k \tilde{A}_k(r) e^{i(\mathbf{k}\cdot\mathbf{r} - \omega t)} = \sum_{\mathbf{k}} \tilde{k}(r) e^{i(m\theta + n\varphi - \omega t)} \tag{1.2.20}$$

where$k = (k_r; k_\theta; k_\varphi) = (k_r; m/r; n/R_0)$ is the wavevector in toroidal coordinates and m and n the poloidal and toroidal mode numbers. Each

$(m; n)$ couple represents a helical perturbation of the plasma, which has an angular frequency ω that is, in general, a complex quantity, $\omega = \omega_R + i\omega_I$: its real part describes the propagation velocity, while the imaginary part represents an exponential growth (if $\omega_I > 0$) or damping (if $\omega_I < 0$) of the perturbation amplitude. A helical magnetic perturbation can become unstable if the wavevector $\mathbf{k}$ is in resonance with the magnetic field, i.e. when $\mathbf{k} \cdot \mathbf{B} = 0$, where $B = (0; B_\theta; B_\varphi)$ is the equilibrium magnetic field. A perturbation with $\mathbf{k} \cdot \mathbf{B} \neq 0$ would bend the mean magnetic field, and it would be thus energetically unfavored. The resonance condition can be written as:

$$\mathbf{k} \cdot \mathbf{B} = \frac{m}{r} B_\theta + \frac{n}{R_0} B_\varphi = 0 \rightarrow q(r) = -\frac{r}{R_0} \frac{B_\varphi(r)}{B_\theta(r)} = -\frac{m}{n}, \tag{1.2.21}$$

showing that helical instabilities can only grow at radial positions where $q(r)$ equals a rational value: for this reason, these positions are called resonant radii.

1.2.3 Toroidal magnetic configurations

Among all possible magnetic configurations, three gave the best confinement performances so far and are therefore extensively studied: the Tokamak, the Stellarator and the Reversed Field Pinch. A brief explanation is presented below.

1.2.3.1 Tokamak

The tokamak[5] (literally: "toroidal chamber with magnetic coils") configuration was proposed by Tamm and Sakharov, two Russian scientists, in 1952 and was realized by Artsimovich[6]. The magnetic field needed for confinement comes from both the magnetic field produced by external coils and the induced plasma current. Besides the main toroidal field $\mathbf{B}_\phi$, also a verical component ($\mathbf{B}_z \lesssim \mathbf{B}_\phi$) and a poloidal component ($\mathbf{B}_\theta \sim \mathbf{B}_\phi/10$) are needed for stabilization. $\mathbf{B}_\phi$ and $\mathbf{B}_z$are externally imposed by magnetic coils, while $\mathbf{B}_\theta$is originated by the plasma current, I_p, that is induced by a transformer using the plasma as a secondary conductor.

An important quantity is the safety factor q, defined as a function of the minor radius r:

$$q(r) = \frac{r}{R}\frac{B_\phi(r)}{B_\theta(r)}, \tag{1.2.22}$$

that is bounded for stability reasons to be larger than 1 both on axis and at the plasma edge. It can be shown that:

$$q(r) > 1,\ q(0) \geq 1,\ \frac{q(a)}{q(0)} \geq 3. \tag{1.2.23}$$

1.2.3.2 RFP

The Reversed Field Pinch[7, 8] (RFP) was first studied in the UK, where the first device ZETA has been operated between 1954 and 1968. The RFP

configuration exploits the same confinement principle as tokamak, differing by the amplitude of the magnetic field components and its behaviour, which makes it a near minimum energy state to which the plasma relaxes. In this case, the toroidal and poloidal component are comparable ($B_\theta \sim B_\phi$) and the toroidal component *reverses* at the edge changing sign with respect to the plasma core, as shown in fig. 1.2.2.

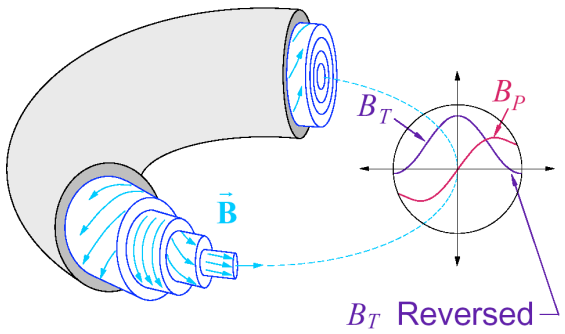

Figure 1.2.2: RFP magnetic field

Another way to see the difference between the RFP and the tokamak is to compare the relative safety factors, as seen in fig. 1.2.3. The difference of the relative amplitudes of the magnetic field components for the two cases results in having $q_{tok} > q_{RFP}$ and it is possible to notice where the toroidal field of the RFP changes sign near the plasma edge, changing sign to the safety factor too.

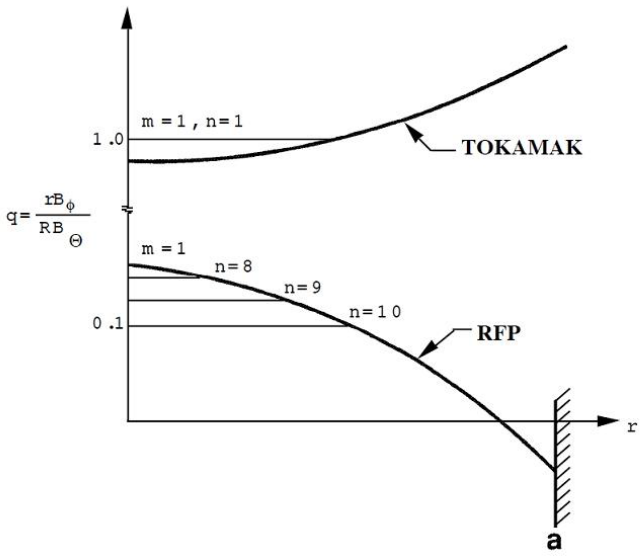

Figure 1.2.3: Comparison of safety factor q as a funcion of plasma radius for tokamak and RFP

1.2.3.3 Stellarator

The stellarator[9] was first designed in 1951 by Lyman Spitzer at Princeton[10]. Unlike the previous two, it is a non-axisymmetric configuration and has no current flowing in the plasma. The magnetic field is helical and is entirely produced by external magnetic coils, which have a very complex design, as shown in fig. 1.2.4. The absence of a plasma current is a big advantage to steady state operation, but the challenge is to design and realize such magnetic coils.

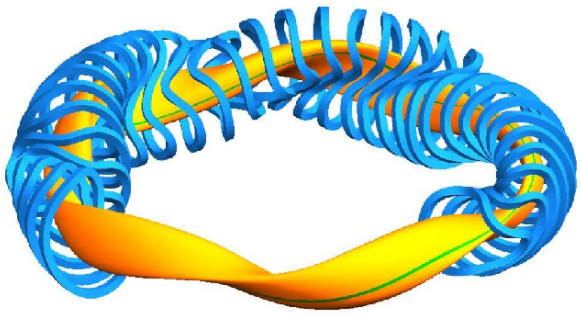

Figure 1.2.4: Design of the stellarator W7-X

1.2.4 RFX-mod

The activity presented in this work has been carried out at RFX-mod[11, 12], the Reversed Field eXperiment located in Padova, that has been operated from 2004, upgrading the original RFX[13], to the end of 2015 when it has been shut down for a second upgrade, RFX-mod^2. The experiment is integrated in the larger ITER project (described in §1.2.5) and gives its contribution to exploring fusion as a possible alternative source of clean energy.

An important feature of RFX-mod is that it is capable of produce plasma both in the RFP and the tokamak configuration. Another notable feature of the device is the set of 192 independent saddle coils secifically designed for the active control system of local plasma perturbations, which played a very important role in the achievement of a plasma current of 2 MA. The main parameters of the machine are presented in table 1.2.1.

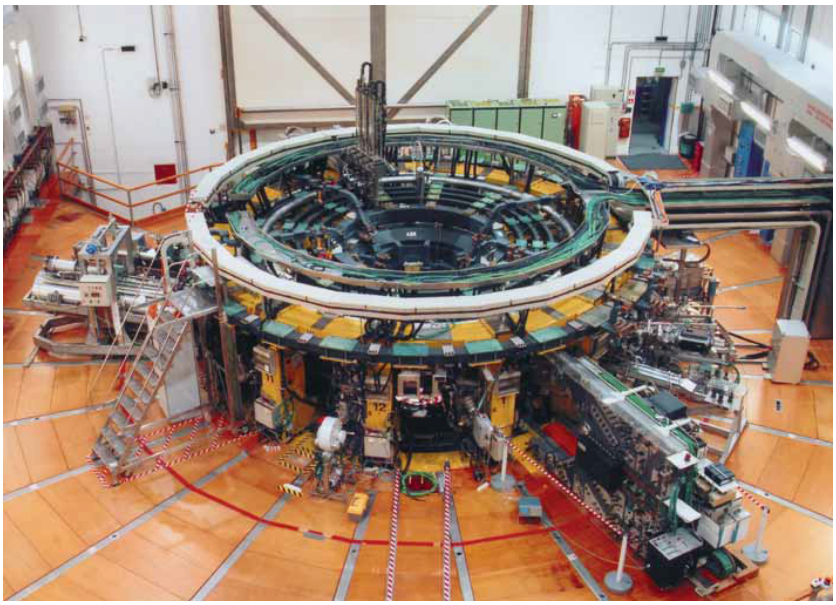

Figure 1.2.5: RFX-mod

Major radius	2 m
Minor radius	0.459 m
Toroidal magnetic field	$\leq$0.7 T
Plasma current	$\leq$2 MA
Discharge duration	$\leq$1.5 s???
Plasma density range	$\sim 1 \div 10 \cdot 10^{19}\,\mathrm{m}^{-3}$
Plasma volume	$\sim 10\,\mathrm{m}^3$

Table 1.2.1: Main parameters of RFX-mod

1.2.5 The future of fusion: ITER

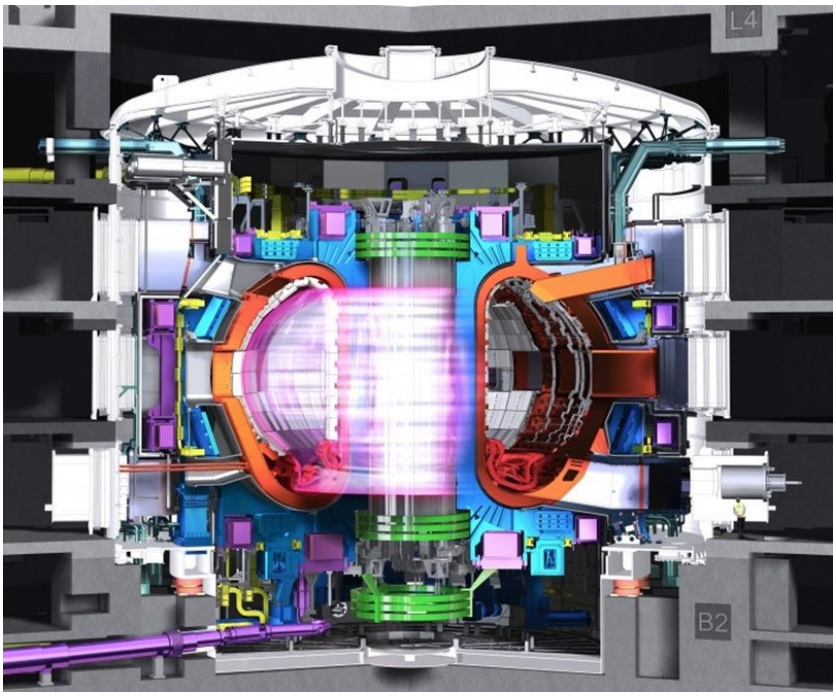

Figure 1.2.6: ITER design

ITER[14, 15], the acronym for International Thermonuclear Experimental Reactor, is the latest and most important experiment presently under construction in Cadarache, France. It represents the joint effort of the European Union, China, India, Japan, Korea, Russia and USA towards demonstrating the possibility of using fusion as a clean source of energy. ITER will be the largest tokamak ever built, with ten times the plasma volume of the largest machine operating today, and it is meant to be the connection between the present scientific experments and a future commercial power plant. A design of the machine is presented in fig. 1.2.6.

Output power	500 MW
Q	$\geq$10
Major radius	6.2 m
Minor radius	2 m
Toroidal magnetic field	5.3 T
Plasma current	$\leq$15 MA
Discharge duration	$\leq$1000 s
Plasma density range	$\sim 10^{20}\,\mathrm{m}^{-3}$
Plasma volume	$\sim 840\,\mathrm{m}^3$
Electron temperature	~ 8.8 eV

Table 1.2.2: Main parameters of RFX-mod

ITER should have a net production of energy in stationary conditions: it should produce 500 MW of fusion power from 50 MW of input power, having an energy gain factor of $Q \geq 10$, for long pulses of 400 to 600 s. The main parameters of the machine are liste in table .The fusion reaction that will make this possible will be D-T reaction, so ITER will also be demonstrating that a *burning blasma* can be achieved and sustained and that tritium can be extracted from the lithium blanket in the vacuum vessel. It will also be a technological challenge to design and test materials, diagnostics and all the systems capable of operating for sufficient time under such extreme conditions as those created in these conditions. A final goal but of primary importance is that of demostrating that such a fusion machine can be operated in safe conditions with negligible consequences for the environment.

A list of the parameters of the machine is presented in table 1.2.2.

Chapter 2

The plasma edge

This chapter is an introduction to the main properties of the plasma edge that will be applied and analyzed in the following chapters of this work. In section 2.1, a brief overview on plasma edge configurations is given, followed by the description of the physics of the plasma layer that interacts with the wall in section 2.2 and by the description of the main mechanism of particle exchange in section 2.3. In the last section, 2.4, the phenoemenon of superthermal electrons in the RFP is presented.

2.1 Edge configurations

A key aspect of the fusion plasmas presented in this work is that they are confined by a magnetic field, not by contact with some solid boundary. This is only true in an ideal case because a plasma can and will touch its physi-

cal container due to many factors as MHD instabilities deforming the plasma column, imperfect magnetic confinement, particles stochastic scatter perpendicularly to the direction of the magnetic field and so on.

Two distinct regions are present in the plasma depending on the magnetic field lines geometry: the plasma core and the external region, namely the scrape-off layer (SOL). The core is the the region where the plasma is perfectly confined by magnetic surfaces defined by magnetic field lines closing on themselves; in the SOL, the magnetic field lines intersect the vacuum chamber so the magnetic surfaces hit the first wall (FW) and therefore can no longer confine the plasma. The core and the SOL are separated by the last closed magnetic surface (LCMS), or flux surface (LCFS).

There is an entire field of research devoted to study how the plasma interacts with the FW of the machine from the point of view of heat fluxes, particle exchange, etc., because the behaviour of the FW can influence directly the performances of the whole plasma. Also, the heat fluxes involved when the plasma hits the wall can be as high as tens of MW/m^2 and the FW needs to be capable of handling such power. Furthemore, the continuous particles flux to the wall leads to erosion and sputtering of the plasma facing components (PFC), releasing impurities from the wall that can migrate to the core degradating the plasma performance.

In order to control the plasma-wall interactions (PWI), two configurations of the FW have been developed to force these interactions to happen in specific places: the limiter and the divertor.

2.1.1 Limiter

The first and simplest configuration was obtained by inserting solid objects from the FW into the plasma, the limiter. By using a limiter configuration, It is possible to force all the interaction to happen there, protecting the rest of the FW from unwanted heat and particle loads, and to clearly define the LCFS since all outer magnetic lines hit the limiter [16]. A sketch of this configuration is presented in fig. 2.1.1.

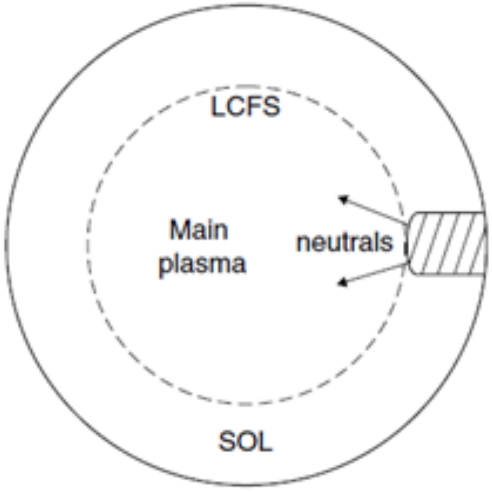

Figure 2.1.1: Limiter configuration

Since the limiter is the designed target of high heat and particle fluxes, it has to be made of specific materials capable of handling such exhaust, as carbon or high Z elements as molybdenum or tungsten. A big disadvantage is that it is subject to a high erosion rate and particles emitted by sputtering from the limiter enter directly the plasma and can degrate its peformance increasing power emission losses (proportional to Z^2).

2.1.2 Divertor

A more sophisticated configuration is achieved modifying the magnetic geometry of the plasma edge, directing the open field lines of the SOL to the plates of the divertor away from the plasma core, as shown in fig. 2.1.2. Creating to regions for the confined plasma and the power and particles exhaust overcomes the main issue of the limiter.

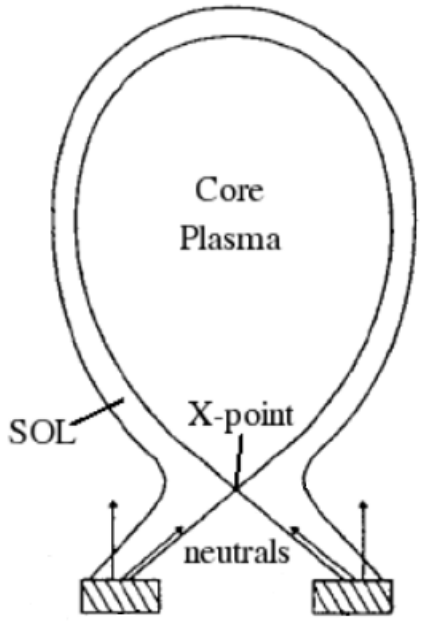

Figure 2.1.2: Divertor configuration

The change in the magnetic topology creates a special point where the poloidal field vanishes, the X-point, which defines the *separatrix* and the *private flux region* under it. The separatrix is the magnetic line passing through the X-point, dividing the plasma core from the SOL, thus corresponding to

the LCFS. The private flux region is a special region because receives particles and heat only from the SOL and is a region characterized by enhanced recycling from the divertor plates that increases impurities screening.

2.2 The Scrape-Off Layer

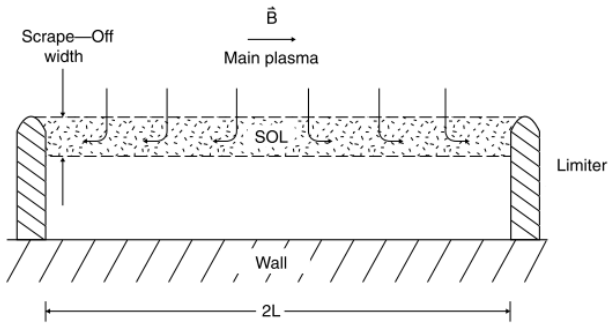

Figure 2.2.1: Scrape-off layer of a plasma in limiter configuration

In a limited plasma (fig. 2.2.1), charged particles move along the magnetic field lines with a velocity ($v_{\parallel}$) comparable to their thermal velocity, but also have a cross-field component ($v_{\perp}$) directed towards the FW which is much slower than $v_{\parallel}$ because is generated by perpendicular diffusion. When a particle exits the LCFS will hit the limiter before the FW because $v_{\parallel} \gg v_{\perp}$. The particles flux $\Gamma_{\perp}$ entering the SOL from the core can be written as:

$$\Gamma_{\perp} = n v_{\perp} = -D_{\perp} \frac{dn}{dr}, \tag{2.2.1}$$

where n is the particles density, $D_{\perp}$the perpendicular diffusion coefficient and

r the radial distance from the LCFS towards the FW. The density gradient can be rewritten as a function of the SOL thickness l_{SOL}, obtaining:

$$\Gamma_{\perp} = nv_{\perp} = D_{\perp}\frac{n}{l_{SOL}} \tag{2.2.2}$$

The parallel flux is given by:

$$\Gamma_{\parallel} = nv_{\parallel}. \tag{2.2.3}$$

Since electrons are much faster than ions, a negative charge region is created on the limiter which in turns creates an *ambipolar* electric field that accelerates the ions, preventing negative charge accumulation. A positive charge region created in the plasma in front of the negative one, the *Debye sheath*, in order to shield the charge inhomogeinity, with the typical dimension of the Debye length $L_s \sim 10^{-5}$ m. The electric shielding is not perfect and a residual electric field, the *pre-sheath*, remains in the plasma accelerating the charges symmetrically towards the limiters, creating a *stagnation point* at half distance between them where $v_{\parallel} = 0$. From there, particles are accelerated up to the limiter which is at a distance L_c that is half of the connection length, where the parallel velocity reaches the isothermal sound speed that is its maximum given by the *Bohm criterion* [17]:

$$v_{\parallel} = c_s = \sqrt{\frac{k(T_e + T_i)}{m_i}}. \tag{2.2.4}$$

Starting from these expressions for the velocity components, it is possible

to estimate the SOL thickness l_{SOL} by matching the relative times obtained by the ratio of the known distances and velocities. It is easy to obtain the following relationship:

$$l_{SOL} = \sqrt{\frac{D_{\perp} \mathrm{L}_c}{c_s}}. \tag{2.2.5}$$

2.3 Recycling

Magnetic confinement is based on the fact that a charged particle moving in a magnetic field has a drift velocity parallel to it due to the Lorentz force, so by shaping the field it is possible to contain the displacement of such particle. In a fusion plasma, many other factors interfere with this confinement and the main things that influence particles transport are Coulomb scattering between charged particles, the toroidal geometry that curves the magnetic field, particles trapped in banana orbits, ambipolar diffusion and turbolence. All these effects contribute also to a diffusion of particles perpendicularly to the magnetic surfaces, thus in the direction from the magnetic axis towards the edge, where they can escape the plasma and hit the first wall.

This flux of particles towards the first wall can results in different phenomena depending on the particles energy: if the flux is too energetic the wall can melt or sublimate, physical or chemical sputter can be induced from the surface or neutral atoms of the species constituting the plasma can be extraced from the wall. This last, called *recycling*, is by far the predominant

effect and is characterized by the *recycling coefficient*, R, that is the ratio of the particles flux out of the wall to the incident flux:

$$R = \frac{\Gamma_{wall \rightarrow SOL}}{\Gamma_{SOL \rightarrow wall}}. \tag{2.3.1}$$

From a general point of view, the physical mechanism that describes the particles interactions with the wall is the same described for the limiter case in section 2.2. The consequences of these interactions are different between ions and electrons depending on their mass difference, but both lead to the emission of neutral atoms from the surface.

When a plasma electron hits the first wall, it will mainly be absorbed by the surface and will recombine with an ion. The neutral atom created is usually weakly bounded to the surface and so is likely to be expelled by the material by thermal emission or as a consequence of the impact by another particle.

An impinging ion (or neutral) will undergo one or more elastic or inelastic scattering and can be either backscattered to the plasma or remain trapped inside the material. In the first case, it will most likely recombine with an electron of the surface and re-enter the plasma as a neutral atom, where it will be ionized again. In the second case, it can diffuse back to the surface or can remain trapped as an ionized impurity inside the solid structure possibly causing important lattice modifications that can lead to severe material degradation.

The atoms extracted from the surface are by large measure those which constitute the plasma (H, for example) because of the mechanism just explained, only a small fraction is constituted by atoms of the surface material (as carbon) and an even smaller one by other impurities trapped in the wall. When these neutrals re-enter the plasma they undergo a scattering process by plasma particles and are ionized mainly due to electronic impact. The atom can be excited by a collision with a particle that does not have enough energy to ionize it, or can be originated by recombination between an ion and an electron. In the case of a neutral hydrogen atom, about 50% of the times when it passes from an excited state to the minimum energy level, it experiences the transition from the level n=3 to n=2 that corresponds to the emission of a photon with a determined energy corresponding to the wavelength $H_\alpha = 6561$ Å.

2.4 Asymmetries in the field at the edge: superthermal electrons

A strong asymmetry in the edge current density is present in the edge of the RFP but not in the tokamak's one. This phenomenon was first observed in 1990 at ZT-40M [18] using an electron energy analyser (EEA) and a portion of high energy electrons was found to carry a large fraction of the edge current density (parallel to the poloidal field at the edge) with an energy flux of 250 MW/m^2. Following measeurements found that the temperature of these

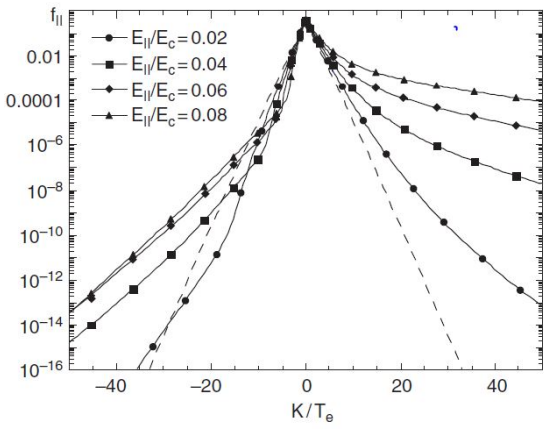

Figure 2.4.1: Example of an EEDF deformation

electrons is comparable to that of core [19, 20, 21] instead of the edge temperature, and the asymmetry between the parallel and anti-parallel directions was between 3 and 12 [22, 23, 24]. These so called superthermal electrons are described as a deformation of the electronic energy distribution function (EEDF), represented by a high energy tail at the end of it. Superthermal electron density (and so the heat flux carried by them) is inversely proportional to the density, since in a high density plasma they undergo more collisions that make it more unlikely for them to reach the plasma edge, at least with a significant portion of their starting energy. Their production has been found to be a stationary process during a discharge, so as the EEDF deformation, so the underneath mechanism needed to be understood. An example of the EEDF distorsion is presented in fig. 2.4.1, where the Maxwellian distribution is modified for different values of the electric field fluctuations at the edge [25].

The origin of superthermal electrons is not clear yet, even if different theories have been proposed: the two most diffused are the kinetic dynamo theory (KDT) and the MHD dynamo. According to the former, these highly energetic electrons diffuse from the core to the edge due to the magnetic field stochasticity induced by tearing modes [26, 27], while according to the latter, they can be described by the presence of a dynamo field created by a non-linear superposition of core-resonating tearing modes [25, 28, 29]. Both these models describe fluctuations in the electric field at the edge, creating a net field which accelerates electric particles in opposite directions and thus defining an electron and an ion drift side, and an EEDF deformation with the presence of superthermal electrons; the difference between the two is in the shape of the modified tail and the relative weigth of these electrons. Other possible explanations involve the generation by Landau damping of kinetic Alfvén waves [30] and the acceleration of electrons on reconnection events driven by the dynamo tearing modes [31]. A comparison between experimental results and theory is not made because it goes beyond the purpose of this thesis.

Chapter 3

Advanced divertor simulations

This chapter presents numerical simulations perfomed on order to compare the quasi-snowflake configuration to a standard divertor, in the context of preliminary studies for the proposed FAST tokamak. The concept of the snowflake configuration is introduced in section 3.2, while the code used for the simulations is described in section 3.3. The description of the activity carried out is presented in section 3.4 and the main results obtained are discussed in section 3.5.

3.1 Introduction

The divertor configuraton is used in all most advanced tokamaks because of its ability to handle power and particle exhaust with positive implications for the overall plasma performance. Nevertheless the loads involved in next

generation machines as ITER and DEMO are too high for the divertors now in use, so many improvements and alternatives are now at study.

Plasma current	6.5 MA
Toroidal magnetic field	7.5 T
Major radius	1.82 m
Minor radius	0.64 m
Elongation	1.7
Triangularity	0.4
Density	$2 \cdot 10^{20}$ m^{-3}
Flat-top phase length	13 s
H&CD power	40 MW

Table 3.1.1: FAST reference scenario parameters

In this framework, the snowflake configuration [32, 33] is being studied experimentally and numerically as a promising alternative to the present standard divertor configuration. The analysis presented in this work was made in the contest of divertor studies for the proposed FAST tokamak [34, 35, 36] carried out with the EDGE2D-EIRENE code.

FAST (Fusion Advanced Studies Torus) was a designed tokamak proposed by the Italian Association on Fusion Research conceived as a ITER satellite facility, with particular attention to the power exhaust handling problem. The parameters foreseen for the reference scenario [37] are summarized in table 3.1.1.

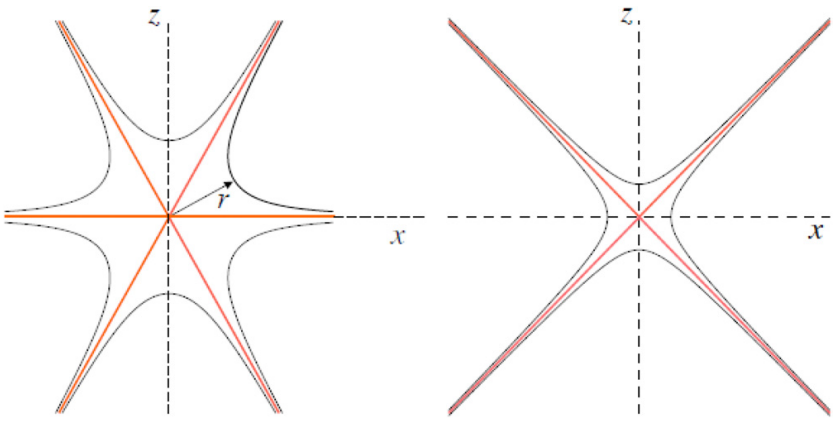

Figure 3.2.1: Difference between the SF configuration and the SD at the X-point

3.2 Snowflake divertor

The snowflake (SF) is a proposed alternative for the divertor magnetic configuration in response to the problem of particle and power exhaust in a fusion reactor framework. The magnetic configuration is changed from the standart divertor (SD) by modifying the magnetic field of the divertor region generated by the magnetic coils. The X-point of a SD is where the poloidal magnetic field B_{pol} is null, which is transformed into a second order null in the SF, being a null for both B_{pol} and its first derivative. A direct consequence is that the separatrix is no longer split into 4 sectors (X-point) but into 6 sectors, as presented in fig. 3.2.1, where the comparison between SD and SF at the X-point is shown; it is also possible to see that the SF derives its name from its similarity with a snowflake.

This modified geometry has different positive consequences on the flux

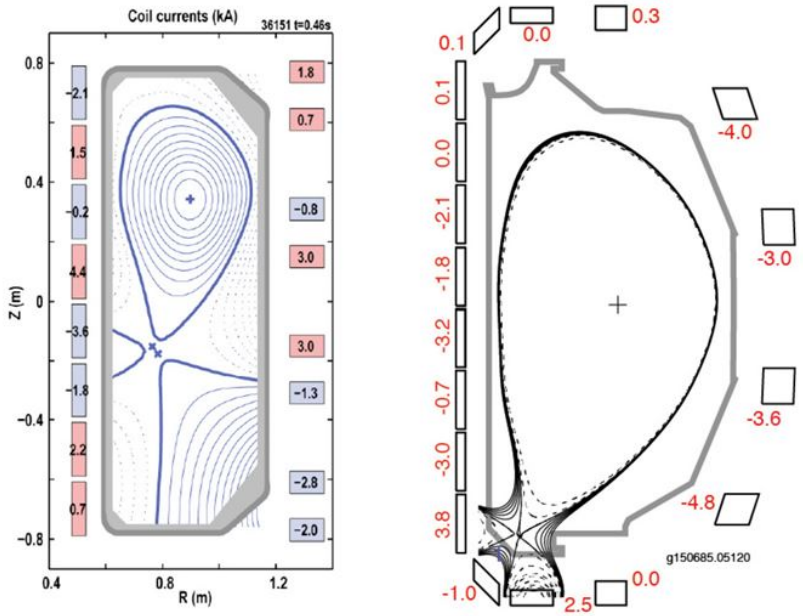

Figure 3.2.2: Plasma equilibrium of SF configuration at TCV (left) and DIII-D (right)

directed on the divertor targets. The higher order null of the poloidal field creates a wider region near the X-point where the field is weak, enhancing flux surfaces separation that causes the lowering the incident power density on the divertor plates because the impinging flux is spread on a wider region. In that weak field region, field lines run almost only in the toroidal direction with a consequent increase of the connection length and the particles dwell time in the scrape-off layer (SOL) [38] allowing deeper cross-field diffusion and more interactions between charged and neutral particles, which in turn increases local charge exchange near the strike point that enhances radiative volumetric losses [39]. Finally, the increased number of the separatrix branches allows the power flux to be splitted on different regions of the

targets, reducing the overall power density. So, in comparison with a standard divertor, reduced peak heat loads and lower incident power densities are expected with a snowflake divertor. The feasibility of such a configuration has been demonstrated by experiments [40, 41, 42] and the plasma equilibria obtained at TCV and DIII-D are shown in fig. 3.2.2.

A major drawback of the snowflake configuration is that it is unstable and needs a higher magnetic field generated by the divertor coils in order to be stabilized, which in turn lowers the maximum plasma current achievable during the discharge. A stable configuration that preserves most of the advantages is a quasi-snowflake (QSF) in which the second order null is split into two separate nulls that are located within tens of centimeters away from each other. One of these nulls is then identified with the X-point while the other can fall outside the vacuum chamber, reintroducing a 4-branch separatrix but mantaining the flux expansion property.

3.3 The simulation code

A first comparison between the SD and the SF under plasma conditions compatible with the proposed FAST tokamak had already been carried out with a simple and versatile code as TECXY [38]. This is a bidimensional code based on Braginskii-like equations with a quite exhaustive physics modelling that has been widely used in many other experiments [43, 44, 45, 46, 47]. The main limits of TECXY are the use of a simplified divertor geometry

that has to be perpendicular to the incident poloidal field lines, the neglect of the private region in calculations and an approximate analytical treatment of neutrals dynamics. Preliminary results showed a power load mitigation in the SF divertor plates higher than expeted, pushing for a further analysis carried out using a more sophisticated and complete modelling tool as the EDGE2D/EIRENE code, described in sections 3.3.1 and 3.3.2.

The activity done in this context is a mid-step between simpler preliminary and more complete and rigorous simulations done with two very different codes, so the focus was on setting parameters of EDGE2D/EIRENE trying to obtain results comparable with those from TECXY and pushing further these simulations by using real geometry divertor plates. The results obtained in this work qualitatively confirmed those predicted by TECXY.

In the context of this thesis, only an introductory presentation to the code will be given while a rigorous explanation of the physical model and all the relative equations can be found in [48].

3.3.1 EDGE2D

EDGE2D is a multi-fluid bidimensional code specially developed to study plasma edge behaviour in tokamaks. It was first developed at JET [49] for modelling divertor configurations and is now one of the most used codes (combined with the EIRENE module) along with SOLPS, against which it has been benchmarked giving very similar results [50].

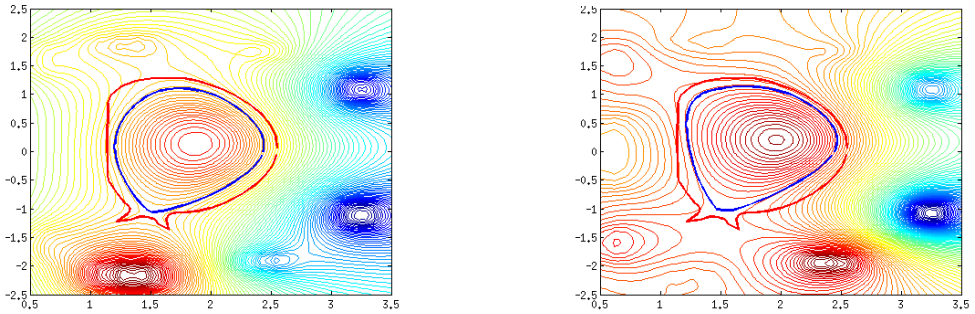

(a) Standard divertor (b) Quasi-snowflake divertor

Figure 3.3.1: Plasma equilibrium comparison for SD and QSF

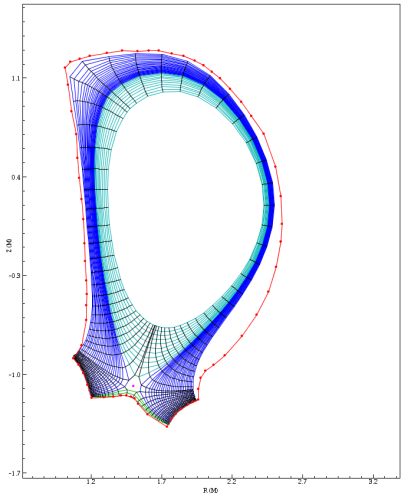

Figure 3.3.2: QSF geometry used

EDGE2D solves simplified fluid equations for particle, energy and momentum conservation for hydrogenic and impuruty ions, while particle and energy sources due to neutrals are handled by the 3D Monte Carlo module EIRENE described in section 3.3.2.

The code also allows the simulation of impurity injection, localised wall

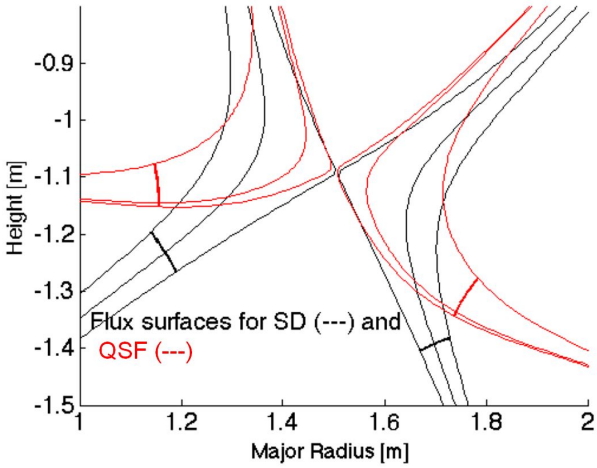

Figure 3.3.3: Flux surfaces on the standard (black) and quasi-snowflake divertor (red)

pumping and particle recycling from the wall. The conservation equations are treated by means of the Braginskii equations, with classical transport parallel to the magnetic field and anomalous in the perpendicular direction.

The code accepts as input the plasma equilibrium reconstruction, the ones used in the two cases of the SD and the QSF studied in this context are shown in fig. 3.3.1. Starting from this equilibrium reconstruction, it is possible to create a bidimensional mesh of the region of the plasma to be simulated; the grid used for the QSF case is shown in fig. 3.3.2, where the different colors are for the different areas of the plasma: the plasma core is in light blue, the SOL is in dark blue, the private region in green, the X-point in pink and the first wall edge is in red. Finally, the different flux surfaces obtained for the configurations are compared in fig. 3.3.3.

3.3.2 EIRENE

At the plasma edge, collisions between neutral atoms can be ignored due to the low density and so neutrals dynamics can be described by a kinetic model. This part is tackled by EIRENE, a Monte Carlo code first developed by D. Reiter in the early 80's [51]. It is a multi-speces neutral gas transport code which simultaneously solves a system of time dependent or stationary linear kinetic transport equations [52]. A key aspect for the integration with fluid codes as EDGE2D, is that it solves these equations in the same spatial domain as the fluid code using the plasma background calculated by it.

When EDGE2D calls the EIRENE module, a set of neutral atoms is created and represented by a Marcov chain [53] that keeps track of position, velocity and particle species along all the paths followed by the neutrals. The code is also coupled with an external atomic and molecular database of the relative cross-sections of the different possible reactions that a nuclear atom can undergo: ionisation, charge exchange, radiative or dissociative recombination and dissociative excitation or ionisation. The result of these simulations is passed back to EDGE2D as external source terms to be added to the plasma fluid equations.

3.4 Numerical simulations

The activity focused on the comparison between standard single-null and quasi-snowflake divertor configuration in reactor relevant conditions. The

EDGE2D code

The different computational meshes used for the two cases are shown in fig. 3.4.1, where the zoom is in the divertor region.

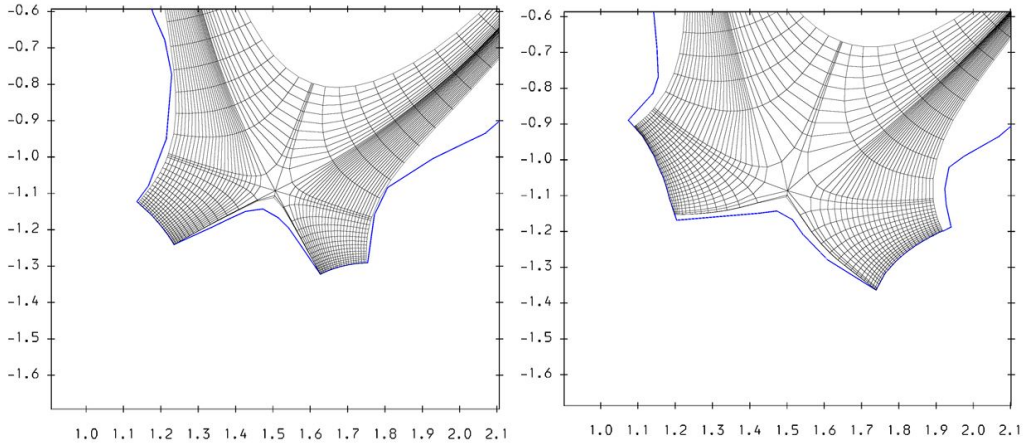

(a) Standard divertor (b) Quasi-snowflake divertor

Figure 3.4.1: Computational meshes

Gas	D
FW & divertor material	W
$n_{e,LCMS}$	$0.5 \div 1.3 \cdot 10^{20}\ \mathrm{m}^{-3}$
P_{SOL}	30 MW
$D_{\perp}$	$0.5\ \mathrm{m}^2/s$
$\chi_{\perp}$	$1\ \mathrm{m}^2/s$
Albedo	$0.92 \div 0.9985$

Table 3.4.1: Simulations parameter ranges

A step has been made here considering real divertor geometries instead of the formerly used geometry perpendicular to the incident magnetic field lines. The different performances of the SD and SF configurations were analysed in a standard H-mode deuterium plasma varying plasma parameters as

electron density, number of neutrals handled by EIRENE, wall recycling and impurities seeding. The parameter ranges explored during the simulations are summarized in table 3.4.1.

3.5 Data overview and main results

At first, a density scan was performed using a real geometry design considering the particle sink (the pumping port of a real experiment) as being in the private flux region and the recycling coefficient of the first wall and the divertor plates equal to 0.9985.

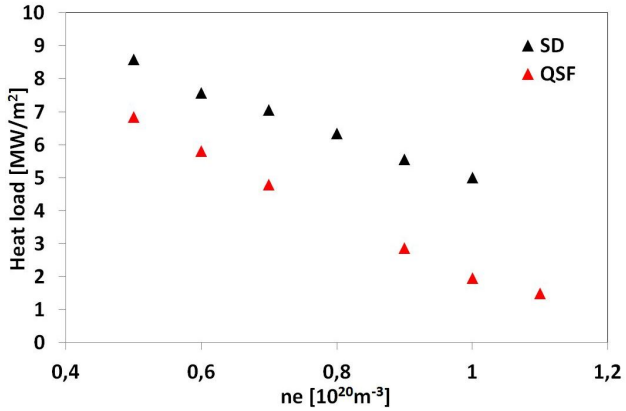

Figure 3.5.1: Heat loads plotted against electron density

In fig. 3.5.1 the heat load on the divertor targets is plotted against electron density, showing that the SF configuration offers a power load mitigation of about 20÷60% for the considered cases.

How this power is distributed onto the divertor plate is shown in fig. 3.5.2, where the incident power is plotted versus the distance from the strike

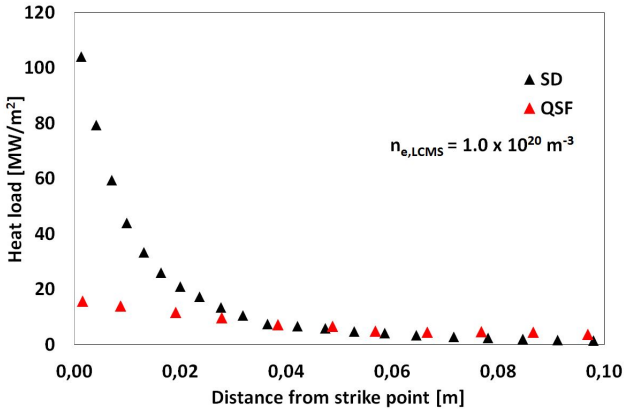

Figure 3.5.2: Heat load on the divertor target plotted against distance from the strike point

point for the case $n_e = 10^{20}\ m^{-3}$. It is possible to note that the SF yields a large reduction in the intensity of the heat peak at the strike point and a smoother heat decay along the target, resulting in a heat decay length $\lambda_{q,div}$ more than twice as large as the SD case. The reduction of the heat peak and the flattening of the heat profile in the SF is helped by the large interaction of the plasma with the neutrals in the divertor region. This also results in the increase of volumetric losses by 20÷40% (fig. 3.5.3) in the form of large re-ionization and radiative losses that can in addition have the positive consequence of reducing target erosion [54].

The very different way in which TECXY and EIRENE treat neutrals dynamics was reflected in a large difference in the neutral density at the outer divertor target. These differences would probably be due to how EDGE2D controls the plasma density at the outer mid-plane, assuming that the neutrals flux to the mid-plane is negligible. At first an attempt was made by

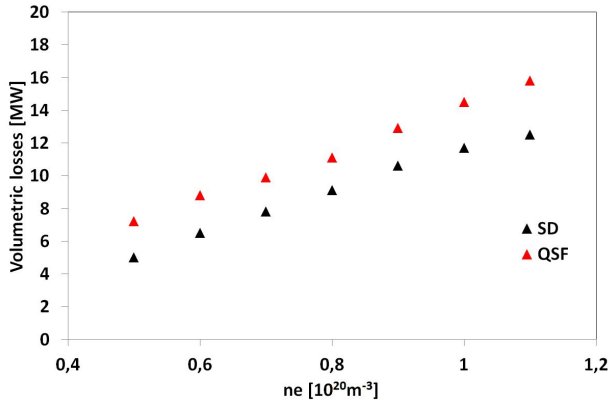

Figure 3.5.3: Volumetric losses

changing the directly involved flux particle into the SOL, $\Gamma_{\perp}$, but the best results where obtained applying a feedback control on the gas puffing and changing the pumping flux. Still an unsatisfactory difference in the neutrals density remained, which was up to five times larger in the EDGE2D/EIRENE case compared to TECXY. Finally an albedo scan was performed varying wall recycling and pumping coefficient, finding a good agreement between the two codes for a recycling value of 0.92 (compared to the starting 0.9985), value at which the neutrals flux to the mid-plane starts being no longer negligible.

The injection of neon impurities has also been simulated as gas puffing in the divertor region for the case $n_e = 0.5 \cdot 10^{20}\, m^{-3}$ allowing the Ne puffed flux to span in the range $\Gamma_{Ne} = 1 \cdot 10^{19} \div 1 \cdot 10^{21}\, s^{-1}$. A numerical summary of the results obtained is presented in table 3.5.1, where all quantities refer to the outer divertor plate.

According to these simulations, the SF configuration radiates more power than the SD and even if W radiates efficiently, its production is confirmed to

	n_e $[10^{19}m^{-3}]$	T_e $[eV]$	P_{load} $[MW]$	P_{SOL} $[MW]$	f_{rad} [%]	$n_{Ne/D}$	Z_{eff}	Γ_{Ne} $[10^{19}s^{-1}]$
SD	3.5	30.8	24.8	5.0	16.6	0.002	1.002	1
	3.5	30.8	24.7	5.0	16.8	0.02	1.018	5
	3.4	30.0	24.5	5.1	17.7	0.087	1.077	50
	3.3	33.4	24.4	5.4	18.1	0.235	1.207	100
SF	1.9	59.0	22.1	7.6	25.3	0.005	1.007	1
	1.9	57.4	21.9	7.8	25.9	0.045	1.042	5
	1.9	61.0	21.2	8.3	27.7	0.215	1.191	50
	1.7	47.1	20.6	9.1	30.2	0.448	1.387	100

Table 3.5.1: Simulations arameter ranges

be negligible and almost all the input power goes into the SOL.

Since it emerges that only one third of the Ne particles remains in the divertor region, it seems that the puffed Ne is not enough to lower the power load. This leeds to the fact that the total load on the divertor plate exceeds the maximum reference value of 18 MW/m^{-2} that is the maximum power that a W mono block can handle.

3.6 Conclusions

The snowflake is an innovative divertor magnetic configuration proposed to respond to the problem of high power and particle exhaust foreseen in fusion reactor conditions. The benefits of this configuration, compared to the standard X-point divertor, are a power load mitigation and a lower power density on the divertor targets. Numerical simulations have been carried out

to verify these predictions in the context of divertor studies for the FAST proposed tokamak.

Previous simulations with the simpler code TECXY gave a power load mitigation larger than expected, so further analysis was performed using a sophisticated and complete software tool as the EDGE2D/EIRENE code. Realistic divertor geometries were introduced as well as computational meshes based on FAST magnetic equilibrium reconstrution. A comparison between the quasi-snowflake configuration and the standard divertor has been carried out varying plasma density, recycling coefficient and Ne impurity puffing.

EDGE2D/EIRENE and TECXY are in substantial agreement for the results found, even if some adjustments had to be done due to the different treatment of neutrals dynamics.

Results show power load mitigation up to 60% and increase of volume losses up to 40% with respect to the standard divertor, confirming the snowflake configuration as a viable improvement for power exhaust handling. Ne puffing does not show the expected benefits as it does not contribute to a power mitigation on the target, the reason in probably in the low input flux set for cases studied.

Chapter 4

Plasma-wall interactions in the visible spectrum

This chapter describes the analysis performed with a fast visible camera in order to investigate surface properties of graphite and tungsten samples exposed to the RFX-mod's plasma. Section 4.1 gives a general overview of the activity motivation and goals, while the detailed description of experimental conditions and data analysis procedure is found in section 4.2. Main results are presented and discussed in section 4.3.

4.1 Introduction

In the framework of possible improvements for RFX − mod^2, the replacement of the present graphite first wall with a metallic one has been experimentally

explored. Tungsten is the material forseen for a large part of the ITER first wall [55, 56] due to its significant capabilities of handling the plasma power and particle exhaust: its very high melting point could allow high heat loads and its lattice properties limit particles entrapment and could allow a better impurity and density control improving the overall plasma performance. Its properties are being explored in present experiments to test its employment in fusion conditions [57, 58, 59].

At RFX-mod, a first wall made of bulk tungsten was not feasible due to its high specific weight and cost, so W-coated graphite samples were considered as an alternative solution. An experimental campaign was performed in order to test different coatings, obtained with different methods by external suppliers, and to find the most suitable for the machine upgrade. The first part of the campaign focused on the set up of a sample discharge to be reapeted, with a magnetic perturbation locked on the samples position in order to maximize the plasma-samples interaction, while with the main part of the campaign consisted in exposing all samples to the same plasma conditions and test the different coatings in plasma conditions.

In this context, an attempt was made to estimate the relative recycling coefficients of graphite and tungsten by using a fast camera in the visible range, which measures the light emitted by recombination and ionization of neutral atoms extracted from the materials; this emission is also a good indicator of the intensity of plasma-wall interactions during the discharge. A crucial part of the analysis has been to properly take into account all the components

that contribute to the total measured intensity, namely reflections from the surroundings, neutrals diffusion and different background material.

4.2 Experimental setup

4.2.1 LISA samples

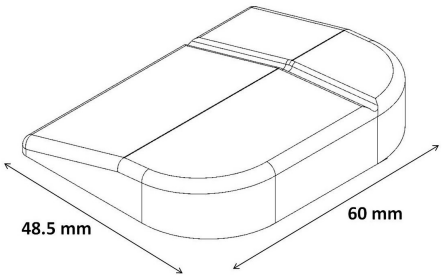

Figure 4.2.1: Sample design

Figure 4.2.2: Samples alignement

The samples used during the experimental campaign are identified by the acronym LISA, standing for Large Instrumented SAmples, because they allow the insertion of two thermocouples from the back surface to measure their bulk temperature. They have been manufactured by reshaping original tiles of the FW to obtain the geometric design presented in fig. 4.2.1.

In order to be exposed to the plasma, the samples have been inserted in the vacuum chamber through a pipe using a remote handling tool. They are designed to be in continuity with the rest of the wall, as shown by fig. 4.2.2, an image taken by a periscopic camera used for maintenance service showing

the good alignement with the tiles nearby.

Figure 4.2.3: Partially coated sample

The samples analyzed are divided into three categories according to the different surface treatments:

- full 5890-PT graphite, the same as RFX-mod's FW;
- bulk graphite with a 10 μm W thin film on all the surface obtained with the High Power Impulse Magnetron Sputtering (Hi-PIMS) PVD tecnique;
- bulk graphite with a 15-20 μm W thin film on part of the surface, as shown in fig. 4.2.3, obtained with the Combined Magnetron Sputtering and Ion Implantation (CMSII) tecnique.

Due to the requirement of contuity with the FW and to the fact that the insertion pipe is located between to tiles raws, as shown by the design in

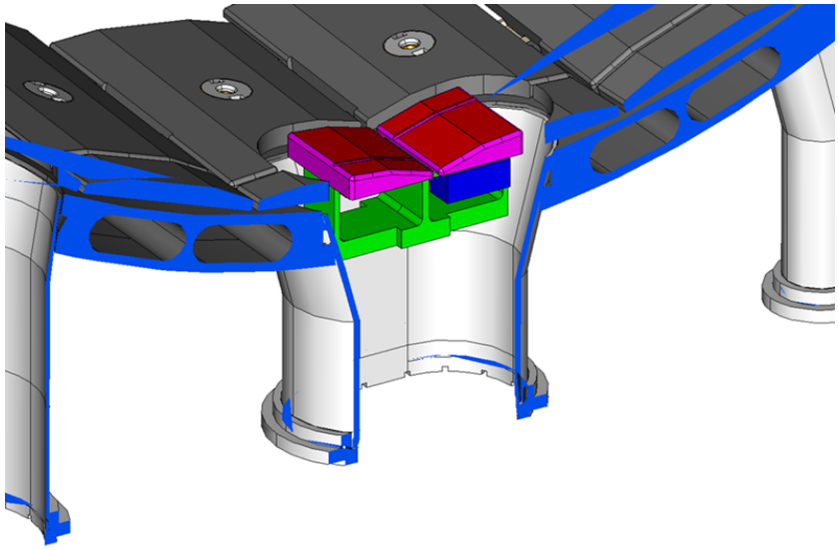

Figure 4.2.4: Design of the samples insertion

fig.4.2.4, the samples have a flat and a sloping region. The figure also shows that two samples were inserted a time, adjacent by the sloping region with their flat surfaces on opposite sides of the pipe. It is to be noted that this disposition defines an inner and an outer sample, with respect to the torus main axis. Different samples combinations were exposed to the plasma allowing to estimate specific correlations:

- inserting two samples of the same material (all graphite or all tungsten) was aimed at evaluating spatial correlation of the interaction, comparing the neutrals emission by the same material at the two different locations. The distance between the main areas of the two samples is $\sim$5 cm;

- inserting both partially coated samples allowed spatial correlation of

the interaction comparing the behaviour of the same material at different locations (comparing the flat areas of the two samples) and the correlation between different materials at almost the same location (comparing the flat area covered with W with the adjacent graphite on the same sample);

- inserting a sample of full graphite and one partially covered allowed to compare the relative behaviour of tungten and graphite both on the same sample at almost the same location and with the other sample a few centimeters away.

4.2.2 Camera setup

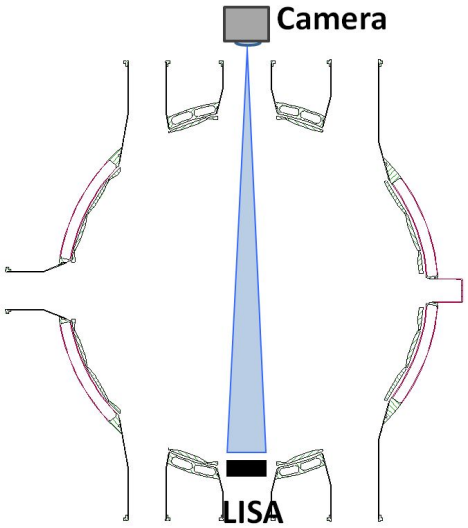

Figure 4.2.5: Sketch of the fast camera view

Camera model	Photron FASTCAM-1024PCI
Resolution	$128 \times 16 \div 1024 \times 1024$
Frame rate	$60 \div 109500$ FPS
Sensor size	17.4×17.4 mm
Sensor type	Monochrome
Sensor pitch	17 μm
Lens mount	C mount
Focal length	25 mm
$F_{\#}$	$f/1.6$
Spatial resolution	1 mm

Table 4.2.1: Camera parameters

The Photron FASTCAM-1024PCI fast camera has been mounted just outside a window in the vacuum chamber with direct frontal view of the samples, as shown in fig. 4.2.5. Its specifications are listed in table 4.2.1. The camera was set to record 512×512 images at a 1 kHz frequency as a compromise between frame rate and dimension of the stored data. The maximum resolution achievable by this camera was 1024×1024 @ 1 kHz, but smaller portions of the detector could be selected in order to reach a frame rate as high as 100 kHz.

By default, the camera always streams the images to a local PC, connected with the acquisition system, which starts recording when receiving a trigger syncronized with the experiment; this signal was a TTL sqaure wave that was previously split by an optical decoupler into two equal signals for the visible and the IR cameras . After the end of a discharge the PC starts transferring the data to the acquisition system.

4.2.3 Camera measurement formula

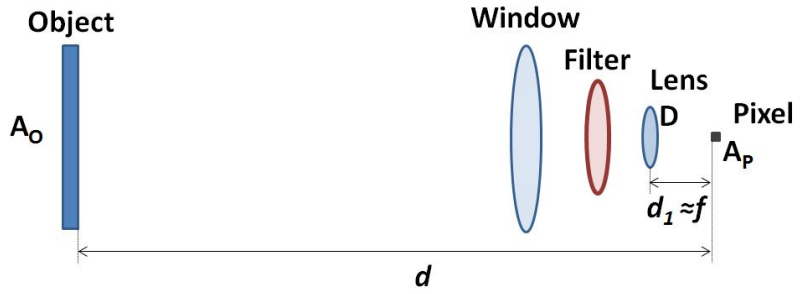

Figure 4.2.6: Schematic of a general measurement with the camera

The detector of the camera measures the intensity $I(\lambda)$ of the incident radiation, which is made up of several components that need to be taken into account. Given the simplified experimental condition represented by fig. 4.2.6, the surface of the object that is seen by every pixel is given by:

$$L_o^2 = \left(L_p \frac{d}{f} \right)^2 \tag{4.2.1}$$

where L_o and L_p represent the linear dimensions of the object's and the pixel's surface, d is the distance between the object and the detector and f is the lens's focal lengh. Only a small fraction of all the radiation emitted from the object is collected from the camera, precisely that inside the solid angle Ω seen by the lens:

$$\Omega = \frac{\pi}{4} \frac{D^2}{d^2} \tag{4.2.2}$$

in the approximation that the $d \gg f$. Given the power emitted by the

source P_s, the total power on a pixel of the detector is the product of these components and of the transmittance $T_F(\lambda)$ of a filter that can be inserted in the optic system:

$$P_p = T_F(\lambda)\Omega L_o^2 P_s. \tag{4.2.3}$$

Introducing now the camera F-number $F_\#$, defined as the ratio of the lens's focal lengh f to the diameter of the entrance pupil D [60]:

$$F_\# = \frac{f}{D}, \tag{4.2.4}$$

and combining the previous equations, it is possible to rewrite the incident power as:

$$P_p = \frac{\pi}{4} T_F(\lambda) \frac{L_o^2}{F_\#^2} P_s. \tag{4.2.5}$$

This power is integrated over the shutter opening time $\Delta t = 1/S_T$, and the camera output is proportional to this value by a conversion constant $K_T(\lambda)$, which also includes the area of the pixel. Finally the intensity of a pixel can be written as a function of wavelength as:

$$I(\lambda) = K_T(\lambda) \frac{\pi}{4} \frac{1}{F_\# S_T} T_F(\lambda) P(\lambda). \tag{4.2.6}$$

It is possible to invert the formula in order to obtain the value of the source power from the pixel value:

$$P(\lambda) = \frac{4}{\pi} \frac{F_{\#} S_T}{K_T(\lambda) T_F(\lambda)} I(\lambda). \tag{4.2.7}$$

4.2.4 Background and diffusion correction

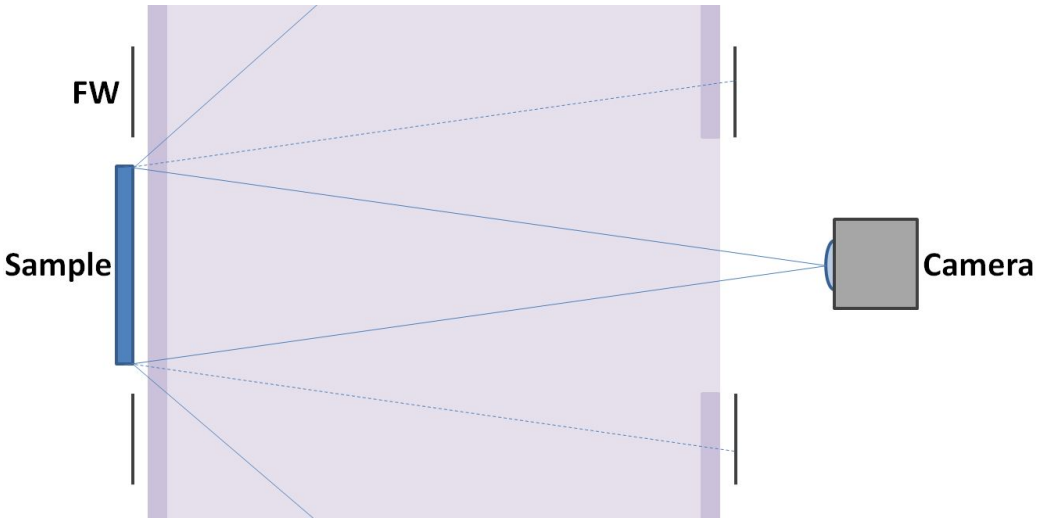

Figure 4.2.7: Schematic of experimental conditions

In the actual experiment, the situation is more complicated than described in the previous section because the plasma needs to be taken into account as well as the fact that the light measured by the camera is not emitted by the samples but by neutral atoms in front of them. The general measurement situation is depicted in fig. 4.2.7 where the outer plasma region of the plasma is in a different colour (dark purple) to highlight that it is the region where almost all neutrals are confined because they are emitted from the wall and are almost immediatly ionized. Many factors can interfere with the measurement and therefore need to be taken into account as part

of the calibration procedure, as reflections from other sources in the vacuum chamber and plasma emission.

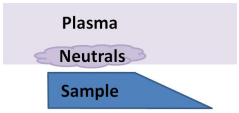

Figure 4.2.8: Background correction

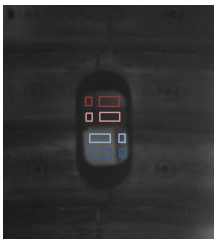

Figure 4.2.9: Areas considered for analysis

The main problem is that the samples surfaces are rough as a consequence of the thin film deposition and plasma interactions, so they can reflect ligth coming from angles much wider (solid lines in 4.2.7) than the camera field of view (dotted lines). This consideration is particularly relevant to the tungsten case because it has a very high reflectance and is then extremely sensitive to external sources of radiation. To give an idea, in section 5.4.4 it is shown that the tungsten reflectance in the IR range is above 80%. This complicates the image analysis because introduces an uncontrollable source of error that can not be discriminated from the actual local interaction of the samples.

In order to overcome this issue, a possible method based on the comparison between the flat and the sloping areas of a sample has been investigated and will now be introduced, recalling that the H_α emission recorded by the camera is due to neutrals that are expelled from surface and enter the plasma,

so it is a phenomenon strictly linked to local interactions. The first hypothesis introduced is that these two areas reflect almost the same plasma portion because the tilt between the two is only 10°; the second hypothesis is that the sloping surface has a much lower interaction with the plasma than the flat one, being less exposed to it by geometrical reasons, and thus is a weaker neutrals source (fig. 4.2.8). Under these conditions, the signal measured on the sloping surface would quantify the reflections from other sources in the vacuum chamber and could be subtracted to the signal of the flat surface in order to obtain a measure of only the neutrals in front of the samples. The light emission of the plasma in front of the camera is automatically removed when subtracting the contribution from the sloping area.

The image obtained from the camera has been then divided into eight areas corresponding to the central pixels of the different areas to be considered, as shown in fig. 4.2.9.

4.3 Results

The experimental campaign carried out at RFX-mod resulted in about 90 RFP H_2 plasma shots, half of which dedicated to the discharge set up. In the remaining $\sim$ 40 shots, samples have been exposed to $1 \div 1.5$ MA H_2 discharges, with an electron density in the range $1 \times 10^{19} \div 1 \times 10^{20}$ m^{-3}. Even though similar plasma conditions were applied, the interaction with the samples was not constant, resulting in pixel values either too low to be

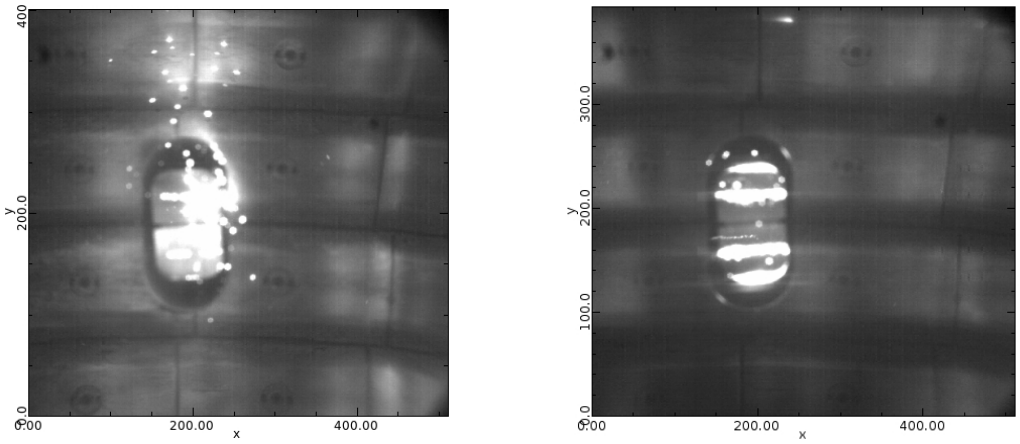

(a) #34420 (b) #34427

Figure 4.3.1: Strong plasma-samples interaction on the corners

distinguished by the background or too high, often reaching pixels saturation. The most common issue that interfered with the image analysis was a strong interaction between the plasma and the corners of the samples, as shown in fig. 4.3.1, that caused delamination of the thin film and ablation of surface atoms; this phenomenon was a strong light emitter that dominated the samples area, preventing a proper analysis. After removing all frames, or entire discharges, that were not suitable for this analysis, only 14 discharges have been considered.

4.3.1 Analysis of recycling of different materials

In the following, the analysis of visible light emission of the samples will be presented. When referring to a material, the discussion is meant to be about the main area of the sample, while it will be specified if the side area is being

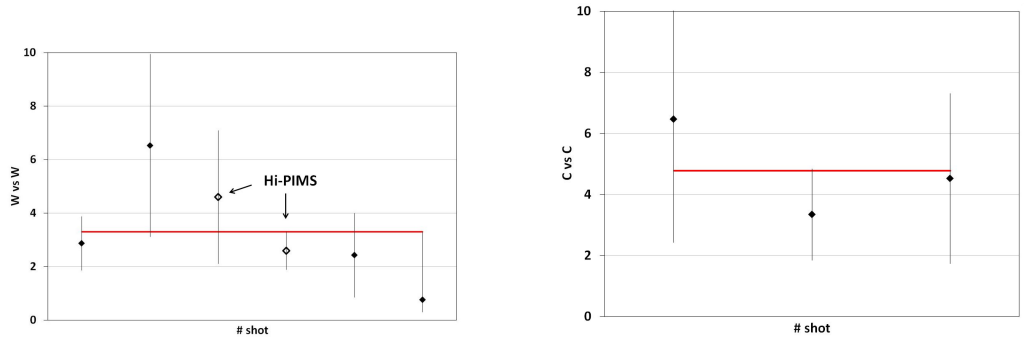

(a) Tungsten, main areas (b) Graphite, main areas

Figure 4.3.2: Comparison between two samples of the same material

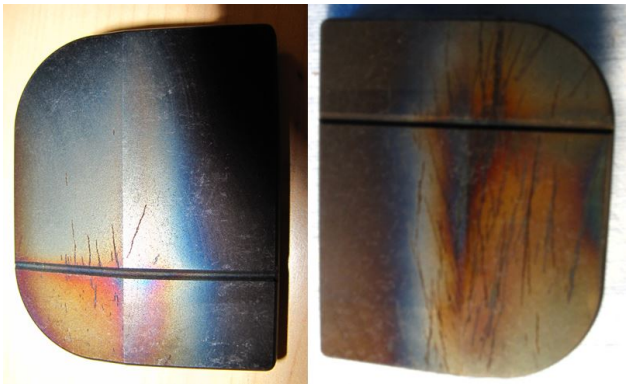

Figure 4.3.3: Outer (left) and inner (right) samples after exposure

considered, according to fig. 4.2.3 as a reference for the distinction. The data points shown in the graphs represent the average value of the considered quantity during the whole discharge, after that single points too dispersed had been removed.

As a first step, the case of two samples of the same material has been considered, for example when both are in full tungsten (fig. 4.3.2a). The ratio between the main areas of the two samples has been analyzed and the

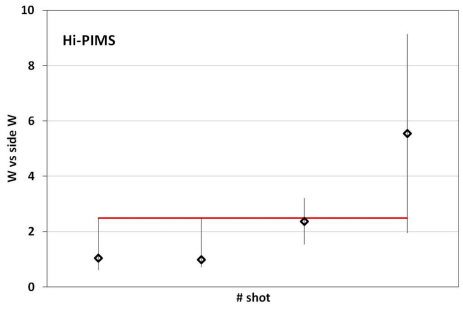

(a) Tungsten, main area vs side area

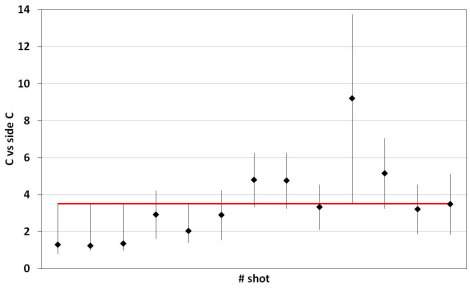

(b) Graphite, main area vs side area

Figure 4.3.4: Comparison of the two areas on the same sample, same material

results, presented in fig. 4.3.2, show an average value of (3.30 ± 2.02). The same procedure has been applied to the case of both full graphite samples (fig. 4.3.2b), obtaining an average value of (4.77 ± 1.57). These values are far away from the ideal value of 1 and show that two samples of the same material do not have the same interactions with the plasma, in particular the inner sample seems to be always more interacting the the outer. This fact is supported by post-exposure analysis on the samples, the case of two full graphite samples is shown in fig. 4.3.3. It is also worth noting that samples obtained with different tecniques show the same behaviour in this context (fig. 4.3.2a).

Another spatial correlation for the same material has been studied considering the ratio between the main area and the smaller side area of the same sample. In this case more experimental points are considered for the graphite because a full graphite sample was also inserted with a partially covered one. The average value for the tungsten is (2.48 ± 2.14) while for the

graphite is (3.51 ± 2.16). Also in this case the obtained values are sensitively higher than the 1. A possible consideration may be done looking again at fig. 4.3.3: the most intense and damaging interaction with the plasma happens at the split between the two areas and possibly this is the cause of such an asymmetry.

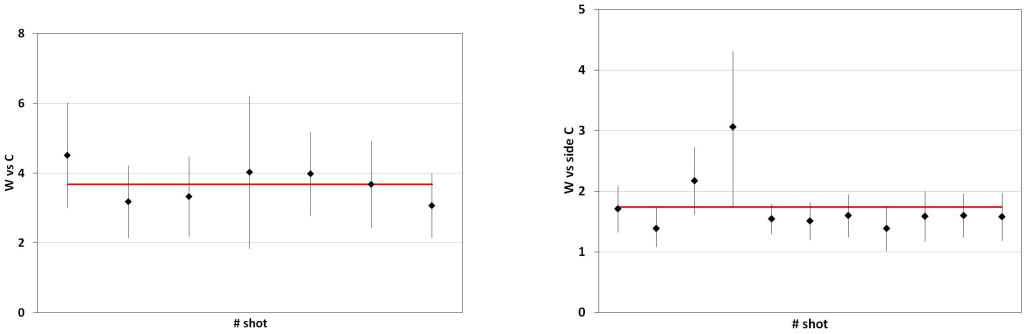

(a) W vs graphite, different samples (b) W vs graphite, same sample

Figure 4.3.5: Comparison between tungsten and graphite

Finally the two materials have been compared, considering tungsten versus the graphite of the main area of the other sample (fig. 4.3.5a) or the one on the side area of the same sample (fig. 4.3.5b). The values obtained are (3.68 ± 0.52) for the two samples and (1.74 ± 0.49) for the same sample. The large discrepancy between the due cases may be due to the different interaction experienced by the inner and outer samples, but in both cases the tungsten is firmly the most interacting one. This results is in contrast with literature and other experiments, which show that tungsten has improved recycling properties compared to graphite. The cause of this deviation from established knowledge is not clear yet: it can be due to sputtering from the

thin film resulting in enhanced (instead of mitigated) neutrals interaction with the plasma, to the large dispersion of the obtained data impying large errors in the numerical analysis, or possibly to a wrong account of contributions to the measurement from the sources of radiation.

4.3.2 Estimate of neutrals path parallel to the wall

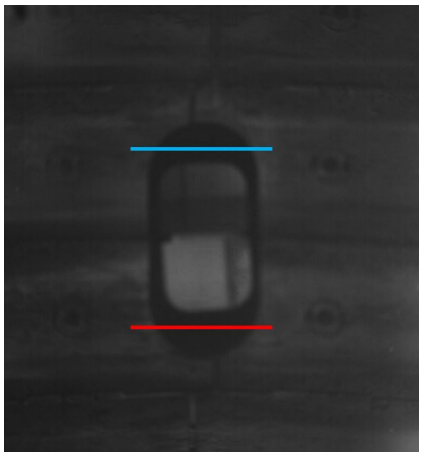

Figure 4.3.6: Outer (left) and inner (right) samples after exposure

Neutrals are emitted by the surface in all directions and can travel a certain distance before being ionized by the plasma. An approximation made in the previous analysis, introduced in section 4.2.4, is that only neutrals in front of the surface are cosidering, neglecting neutrals diffusion in the direction parallel to the surface. An experimental evaluation of the distance travelled in the parallel direction has been made with the fast camera, with the aim of being an introductive observation of the phenomenon. The discharge considered is #34431.

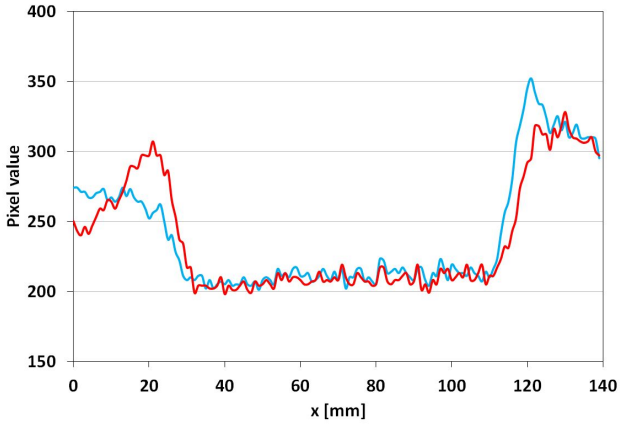

Figure 4.3.7: Outer (left) and inner (right) samples after exposure

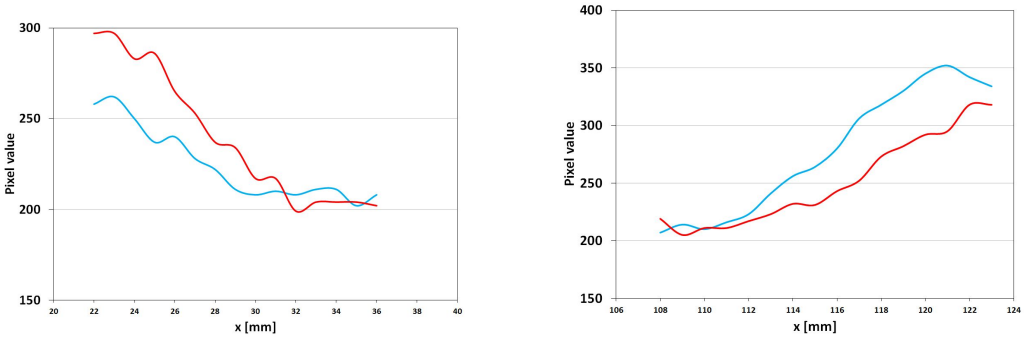

(a) W vs graphite, different samples

(b) W vs graphite, same sample

Figure 4.3.8: Comparison between tungsten and graphite

The H_α profiles analyzed are represented by the two coloured lines in fig. 4.3.6, corresponding to the bottom of the pipe through which samples are inserted in the vacuum chamber; these lines start from the graphite first wall and cross the pipe. The resulting signals measured by the camera are shown in fig. 4.3.7, where it is seen that they have the same behaviour with two peaks at the edges, corresponding to the beginning of the wall, and a central stationary region corresponding to the background value. Peak values

are different because different interactions with the plasma are expected at different locations, while the background value is roughly constant because is due to the bottom of the pipe and to the light emission of all the poloidal section if the plasma seen by the camera.

The focus of this analysis is on the transition between these regions, that are zoomed in fig. 4.3.8, where it is possible to note that although the H_α emission decreases with different slopes depending on the peak values (the higher the peak, the higher the slope), all four transitions seem to be complete in the same space, roughly corresponding to $\sim$1 cm.

A more exhaustive analysis should be undertaken in order to verify if these observations fit with other experimental parameters, as the density.

4.4 Conclusions

Tungsten is the material foreseen for large part of the ITER first wall because it can handle large heat fluxes and retain a small amount of impurities, with positive implications for the overall plasma performance. In the framework of preliminary studies for machine improvements at RFX-mod, tungsten covered samples have been exposes to the plasma to test their properties in experimental conditions. A fast visible camera was used to monitor H_α emission in front of the samples to evaluate recycling properties of the material compared to analogous full graphite samples. This light emission is proportional to the neutral atoms expelled by the surface material and is a good

indicator of a plasma-wall interaction.

Data analysis presented serious obstacles because tungsten is a higly reflective material and isolating the H_α emission due to the plasma-sample interaction from reflections from other locations is not trivial. A method that could properly take into account all factors has been discussed and applied to the analysis.

Another relevant issue has been the intense localized interaction that took place between the plasma and the edges of the tungsten thin film, that often caused layer delamination and material ablation with consequent more intense light emission from those atoms. This frequently resulted in saturated images or portions of them, limiting very much the possible analysis.

Results found that the intensity of the interaction with the plasma depended on the position of the sample: the samples on the inner side of the torus underwent larger interactions than those on the outer side, only a few centimeters away. This has been confirmed also by post-mortem analysis on the samples.

The relative behaviour of tungsten and graphite has also been considered, finding that tungsten is up to four times more interacting than graphite. This means a larger neutrals emission from the tungsten surface than from graphite, in contrast with the expected behaviour described in literature. The reason of this discrepancy has not been understood yet but it is possibly due to the thin film deposition tecnique that caused such strong and localized interactions.

Finally, a method is shown to estimate the average length travelled by the neutrals in the direction parallel to the wall. A very small number of cases has been considered as an introductory step, but the indication so far is that this distance does not depend on the intensity of the interaction and is of the order of 1 cm.

Chapter 5

Infrared measurements

This chapter is dedicated to the activity carried out at RFX-mod to set up an infrared measurement system and to analyze data collected during an experimental campaign in which samples have been exposed in limiter configuration to investigate heat flux properties of the plasma edge. A general introduction on infrared thermography is given in section 5.2. Section 5.3 is dedicated to the inverse heat conduction problem and to the software tools used to tackle it, while in section 5.4 the description of the experimental conditions is exposed. Section 5.5 describes the data analysis procedure and results are presented and discussed in section 5.6

5.1 Introduction

The study of plasma-wall interactions (PWI) is useful in the perspective of a fusion reactor because the behavior of the first wall (FW) influences directly the whole plasma and the achievable fusion power. In particular the FW has to be able to manage the intense, hot plasma exhaust. Experiments have been carried out in RFX-mod in order to investigate the plasma edge of the circular shaped reversed field pinch (RFP) configuration from a heat flux point of view analysing the heat distribution on specially designed graphite samples inserted as limiters. An infrared camera has been set up and used to evaluate the temporal and spatial heat flux distribution from temperature measurement.

5.2 Infrared thermography

5.2.1 The infrared spectrum

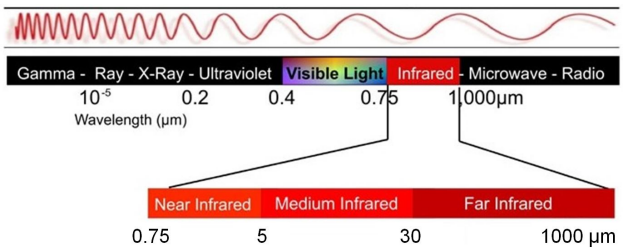

Figure 5.2.1: Electromagnetic spectrum

Experiments involving infrared radiation have been performed since 1777

by Landriani but its discovery is attibuted to astronomer Sir William Hershel in 1800 [61]. He reproduced Newton's experiment of the light refraction through a prysm and measured the temperature of all its monocromatic components with a darkened thermometer noting that the peak temperature was reached far after the red edge of the visible spectrum. This was the first time that the electromagnetic spectrum (fig. 5.2.1) was recognized to expand beyond the visible part.

The infrared (IR) spectrum is divided into arbitrary sub-categories depending on the convention used, an example is reported in table 5.2.1. In particular, the 8-15 μm range is called the "thermal imaging" or "thermal infrared" region because it is where sensors can obtain a comletely passive image of objects with only slightly higher temperature than room temperature, as the human body.

Designation	Abbreviation	Wavelength [μm]
Near-infrared	NIR	$0.7 - 5$ μm
Mid-infrared	MIR	$5 - 30$ μm
Far-infrared	FIR	$30 - 1000$ μm

Table 5.2.1: IR spectrum division scheme

5.2.2 Blackbody radiation emission

Every object emits IR radiation as a consequence of the thermal agitation of its molecules and the higher the temperature the higher the frequency of the emitted light.

An objects emitting radiation at all wavelengths is called *blackbody*, because it absorbs all incident radiation at any wavelength according to Kirchhoff's law [62]. The power W_{bb} emitted from a blackbody follows the *Planck's law* [63]:

$$W_{bb}(\lambda, T) = \frac{2\pi hc^2}{\lambda^5(e^{hc/\lambda kT} - 1)} \times 10^{-6}\ [W/m^2, \mu m], \tag{5.2.1}$$

where h is Planck's constant, c the speed of light, k Boltzmann's constant, T the blackbody temperature in Kelvin and λ the wavelength in μm. Eq. 5.2.1 can be plotted as a function of λ for various temperature, as shown in fig. 5.2.2, obtaining a family of curves with the properties that the maximum of a single curve increases with the temperature and the wavelength at which it occurs decreases with temperature.

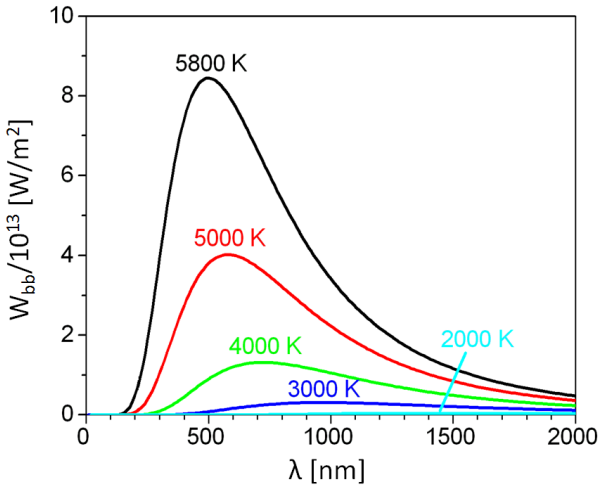

Figure 5.2.2: Blackbody spectral radiant emittance according to Planck's law for different temperatures

This second property can be seen differentiating eq. 5.2.1 with respect to λ and imposing the maximum condition. It is possible to obtain *Wien's displacement law*:

$$\lambda_{max} = \frac{2898}{T}[\mu m]. \tag{5.2.2}$$

This equation directly relates the temperature of the object to the dominant wavelenght of the emitted spectrum. For example, the peak of the sun's emittance occurs at about 500 nm, in the yellow light, corresponding to a surface temperature of about 6000 K. On the other hand, Sirius has a bluish-white light that is peaked at 270 nm, which corresponds to a surface temperature of about 11000 K.

If Planck's formula (5.2.1) is integrated on all wavelengths, the *Stefan-Boltzmann formula* is obtained, which relates the total radiant emittance $W_{bb}(T)$ of a blackbody to its temperature:

$$W_{bb}(T) = \int W_{bb}(\lambda, T)d\lambda = \sigma T^4[W/m^2]. \tag{5.2.3}$$

It can be shown that the portion of the emittance for $\lambda \leq \lambda_{\max}$ is only one fourth of the total.

5.2.3 Non-blackbody emission

Real objects almost never fulfill the conditions of the blackbody discussed so far, although they can approch this limit in some reduced spectral interval.

The physical phoenomenon that prevents a real object from behaving as a blackbody is the way in which it reacts to incident radiation: in general, a non-blackbody will absorbe, reflect and transmit different portions of it. It is important to note that the relative proportions of these parts may change depending on the materials, surface treatments and wavelength considered. So for non-blackbodies three quantities need to be introduced: α_λ is the spectral absorbance of the object at a certain λ, ρ_λ is its spectral reflectance and τ_λ is its spectral transmittance. For energy to be conserved, the following relation must be satisfied at all wavelengths:

$$\alpha_\lambda + \rho_\lambda + \tau_\lambda = 1. \tag{5.2.4}$$

Most materials though are opaque to radiation ($\tau_\lambda = 0$) so the above relations simplifies to:

$$\alpha_\lambda + \rho_\lambda = 1. \tag{5.2.5}$$

One final quantity to be introduced is emissivity ε, defined as the ratio between the radiant emittance of a body and that of a blackbody at the same temperature, gives the measure of how much an objects behaves differently from the ideal case:

$$\varepsilon_\lambda = \frac{W_{\lambda,obj}}{W_{\lambda,bb}}. \tag{5.2.6}$$

Objects can be subdivided into three categories according to the be-

haviour of ε_λ, i.e. their spectral emittance, as shown in table 5.2.2.

blackbody	$\varepsilon_\lambda = 1\ \forall\lambda$
greybody	$\varepsilon_\lambda = const. < 1\ \forall\lambda$
selective radiator	ε_λ varies with λ

Table 5.2.2: Classification based on emissivity

A corollary of Kirchoff's law is:

$$\varepsilon_\lambda = \alpha_\lambda \tag{5.2.7}$$

stating that for any material at any temperature, its emissivity equals its absorbance. In other words, if a material absorbes a certain portion of the electromagnetice spectrum, then it will emit in the same range of wavelengths.

Including eq. 5.2.6, the Stefan-Boltzmann formula can be rewritten in the case of non-blackbody radiation as:

$$W_{bb}(T) = \varepsilon\sigma T^4[W/m^2], \tag{5.2.8}$$

where two cases can be distinguished: if the object is a greybody, its emissivity is constant and the curve W_{bb} will follow that of a blackbody but reduced by a factor ε whereas the behaviour of a selective radiator can be disconnected from the other two. An example of how the spectral emittance depends on the emissivity of the radiant object is presented in fig 5.2.3.

It is important to note that the emissivity (and so the reflectance) is a

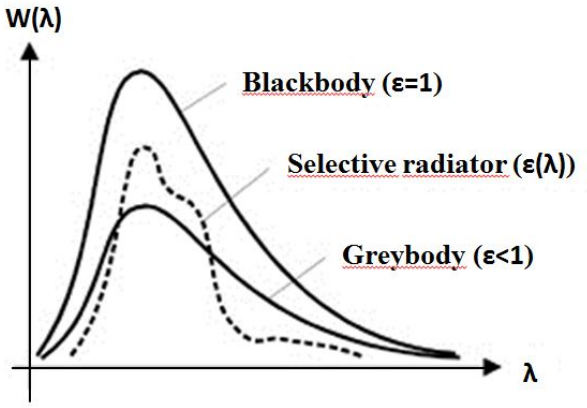

Figure 5.2.3: Blackbody spectral radiant emittance according to Planck's law for different temperatures

property of the surface of the material depending on its roughness, colour, degree of polishment and so on. The emissivity increases with the surface roughness and with the darkening of the colour, while it lowers for polished, lighter coloured, more reflectant surfaces. An example extracted from literature [64, 65, 66, 67] is presented in table 5.2.3, where the emissivities of different materials with different surface treatments are presented. The data presented are intended to be referred to the same spectral range and at the same temperature for all the examples of the same material.

Material	Surface specification	ε
Aluminum	anodized, black, dull	0.95
Aluminum	roughened	0.18
Aluminum	polished	0.05
Carbon	candle soot	0.95
Carbon	graphite, filled surface	0.98
Stainless steel	sandblasted	0.70
Stainless steel	untreated sheet	0.28
Stainless steel	polished sheet	0.14

Table 5.2.3: IR emissivity for different materials

5.2.4 Thermographic measurements

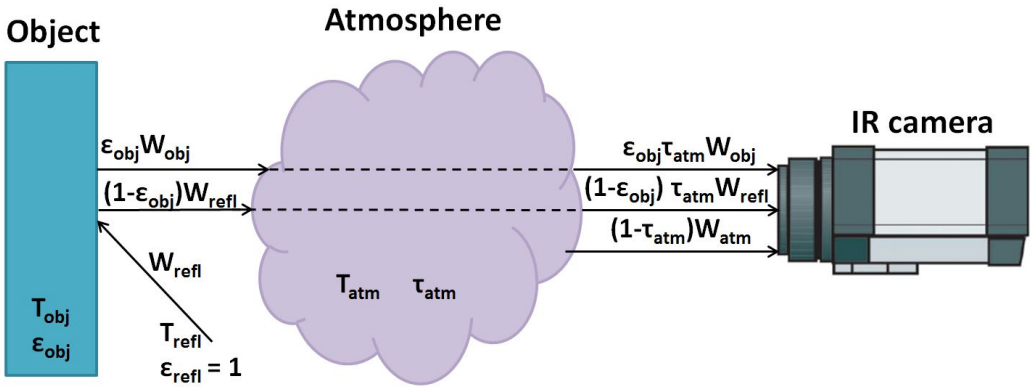

Figure 5.2.4: Schematic of a general thermografic measurement situation

Thermocameras can be used to measure the temperature of an object by means of the radiation it emits in the IR spectrum as described in the previous paragraphs, just like a normal camera can be used to determine the colour of an object. In both cases, the detector of the camera only measures the total incident radiation impinging on it, which however can be composed of several components that can tamper with the object of the measurement,

as shown in fig. 5.2.4.

In the general case, the total power incident on the detector is given by the following components:

- the power emitted from the object according to the greybody emission of formula 5.2.8 is $\varepsilon_{obj} W_{obj} = \varepsilon_{obj} \sigma T_{obj}^4$, then ir travels through the atmosphere being reduced by its transmission coefficient τ_{atm}, giving rise to the total term: $\varepsilon_{obj} \tau_{atm} W_{obj}$;

- the object also reflects the power emitted from its surroundings, $\rho_{obj} W_{refl}$, which again is dumped by the atmosphere and results in $(1-\varepsilon_{obj})\tau_{atm} W_{refl}$, where equations 5.2.5 and 5.2.7 have been used and two assumpions were made. The first is that all the environment is at the same temperature, which is not necessarily true especially in a plasma experiment condition, but since the object is very small compared to the surroundings, the power it receives can be averaged on all the half sphere it sees. The second assumption is that the surroundings emissivity is one, which is true according to the Kirchoff's definition of the blackbody that all incident radiation on its surface will eventually be absorbed by it.

- the power emitted by the atmosphere, assumed to have no reflectance, gives $\varepsilon_{atm} W_{arm} = (1 - \tau_{atm}) W_{atm}$.

Summing up these components yields the total incident power on the detector:

$$W_{tot} = \varepsilon_{obj}\tau_{atm}W_{obj} + (1-\varepsilon_{obj})\tau_{atm}W_{refl} + (1-\tau_{atm})W_{atm} \tag{5.2.9}$$

that can be solved to obtain the object's emitted power as:

$$W_{obj} = \frac{1}{\varepsilon_{obj}\tau_{atm}}W_{tot} + \frac{1-\varepsilon_{obj}}{\varepsilon_{obj}}W_{refl} + \frac{(1-\tau_{atm})}{\varepsilon_{obj}\tau_{atm}}W_{atm}. \tag{5.2.10}$$

This is the final formula to obtain the power emitted by an object from the power incident on the camera, given all the parameters of the surroundings.

5.3 Inverse Heat Conduction Problem

Once the temperature is recorded by the IR camera, the heat flux incident on the object observed is to be calculated. In a well-posed problem, as defined by J. Hadamard [68], a unique solution must exist that varies continuously with the initial conditions. A typical example of a well-posed problem is the heat diffusion equation, where the evolution of the temperature is described as a function of the incident heat, and is a direct problem:

$$\frac{\partial T}{\partial t} = \alpha\frac{\partial^2 T}{\partial x^2} + \frac{\dot{q}}{\rho c_p}, \tag{5.3.1}$$

where T is the surface temperature, q the heat flux, α the thermal diffu-

sivity that can be rewritten as a function of the thermal conductivity k, the mass density ρ and the specific heat capacity c_p as:

$$\alpha = \frac{k}{\rho c_p}. \tag{5.3.2}$$

If, as it is the case, one wants to solve eq. 5.3.1 for q, then the inverse problem is being tackled, that is to say that given the observations of the variation of the temperature T, one is trying to calculate the causal factor producing it. The solution to the inverse problem is given analitically only in few simple cases that generally require uniform initial conditions, uniform and constant heat loads applied and semi-infinite materials. These ideal conditions are never met in a fusion experiment where the heat flux on the wall rapidly varies in space and time. Different numerical methods can be applied to solve this task using infrared thermography alone [69] or combined with thermocouples [70].

5.3.1 THEODOR code

The inverse heat conduction problem has been solved using the code THEODOR [71], a software tool developed for this purpose that has been previously benchmarked against a finite element model [69, 72]. The code accepts as input the surface temperature map evolving in time and computes the heat flux distribution on a bi-dimensional slab geometry approximation for the target, defined by a line along the surface and the relative section on the

limiter. The code allows to take into account a thin dust layer that can have been deposited on the surface after a long exposure to the plasma, but this is not the case of the present study as the samples have never been used before and interacted with the plasma for a short number on discharges

An approximation in considering the bidimensional problem is that the surface diffusivity is neglected in the direction perpendicular to the selected slab. THEODOR was first aimed at studying heat loads on a tokamak divertor, a problem with toroidal symmetry which allows the simplification introduced considering only a slab but may not, a priori, fit experimental conditions as RFX-mod for two reasons. First, the graphite studied is isotropic and so has the same conductivity in all directions and, since the problem considered has no such symmetries as the divertor case, neglecting one of them seems unjustified.

5.3.2 TtoP3D

An alternative program has been developed to solve the inverse heat conduction problem to overcome the limits of THEODOR, namely the lack of access to the source code and a global 3D treatment of the limiter. TtoP3D (Temperature to Power 3D) is a very powerful and flexible tool that can be adapted to a large variety of situations because it can handle time- and space-dependent temperature maps on virtually any geometry with material properties (as the thermal conductivity) than can be change along different directions.

TtoP3D iteratively solves the direct problem of heat conduction presented in section 5.3 in the elements of a 3D mesh of customizable cell size, accepting directly the IR camera temperature map as input. At each time step, the heat flux computed at the previous time is given as input into the equations which are solved. According to the difference between the temperature obtained as a result of the equations and the that from the camera, the heat flux is modified and equations are solved again with the new initial conditions. This step is iteratively performed up to numerical convergence, normally reached within a few iterations.

The code has been tested with real experiment data and benchmarked against THEODOR, as shown in section 5.3.3.

5.3.3 Validation of the software tools

The newly developed code TtoP3D has been benchmarked against THEODOR evaluating the heat fluxes from the same temperature measurement of the discharge #36757. The most interesting quantity for the analysis is the average heat load on one side of the sample, the electron drift side has been chosen for this comparison. The fluxes presented here are the direct output of the codes, that is to say the total deposited heat flux q_{dep}.

Since THEODOR performs computations only in a slab geometry, it has been run iteratively for all the 50 raws that form the image and their average has been considered. TtoP3D can adopt both the bi- and three-dimensional geometry so it has been run in both cases: in 2D the same conventions as for

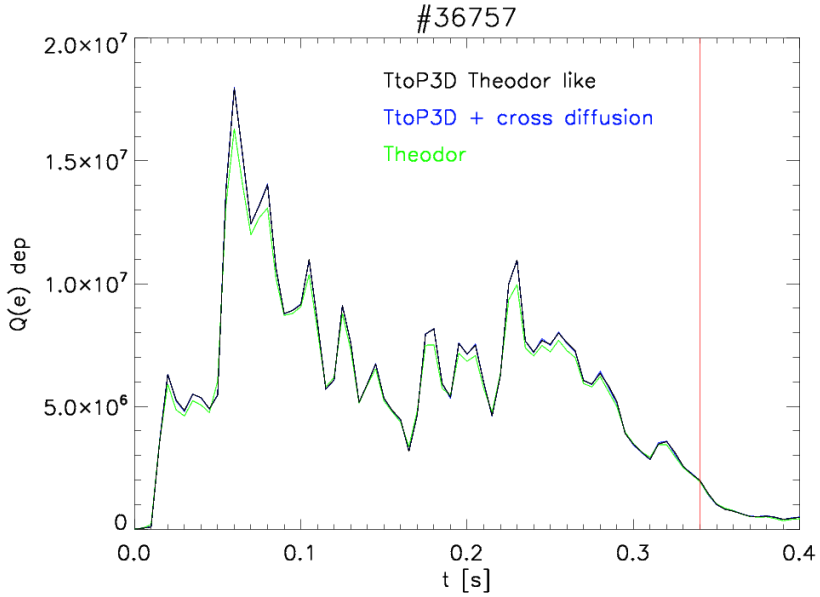

Figure 5.3.1: Comparison of the two codes for shot #36757

THEODOR have been adopted, so it will be referred to as THEODOR-like, while in the 3D case the complete heat map has been solved at once adding the heat diffusivity also in the third dimension, the one perpendicular to the 2D slabs.

The comparison of the three codes is presented in fig. 5.3.1, where the red line indicates the end time of the discharge. The two versions of TtoP3D are exactly superposed indicating that the cross diffusivity can be neglected without appreciably modifying the result of the computation. This code shows an estimated heat flux always higher than THEODOR, but the difference between the two is never larger than 10%. Fig. 5.3.2 shows a zoom of the end of the discharge, confirming the same behaviour of the three cases also in the cooling down phase; only a total time of 400 ms could be considered

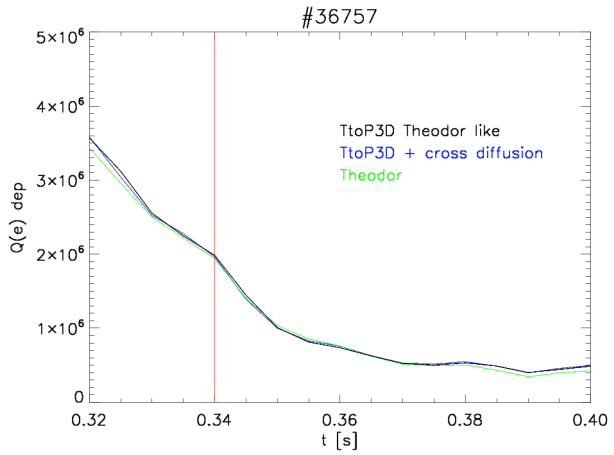

Figure 5.3.2: Comparison of the two codes for shot #36757 after the end of the discharge

because that was the recording time window pre-set for the IR camera.

A further step has been taken in comparing the results of the codes with the enineering code ANSYS: the heat fluxes calculated by THEODOR and TtoP3D from IR measurements have been imposed on a model of the limiter and the resulting temperature has been estimated and then compared to the IR starting values. The same three different cases have been distinguished with the only difference that, due to the computational time required, only a single slab has been considered for THEODOR and TtoP3D THEODOR-like, while the 3D case of TtoP3D was evaluated on the whole sample volume.

The comparison of the bidimensional case is presented in fig. 5.3.3, where the temperature calculated by ANSYS from the different heat fluxes inputs is plotted for a surface line at the time when the maximum temperature has been reached. The codes used show a good agreement with the measured

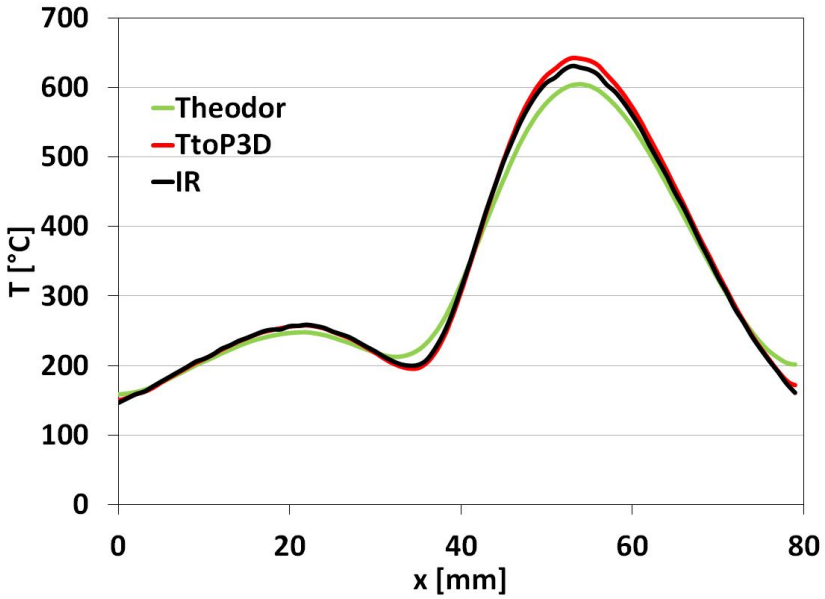

Figure 5.3.3: ANSYS comparison of the two codes with IR on a surface line, shot #36757

temperature from the IR, TtoP3D turned out to be more faithful to the its input data from the camera while THEODOR tends to smooth temperature variations obtaining a flatter profile. The three-dimensional case is compared in fig. 5.3.4, where the value now considered is the surface average temperature on the electron side, plotted versus the discharge time. It is possible to note the very good agreement between numerical simulations and experimental measurements.

The relative errors have been considered and are presented in fig. 5.3.5: in both cases the errors are higher at lower temperature but while THEODOR and TtoP3D agree within the 10% in the range used for heat calculations, TtoP3D shows a very good agreement with the IR measurements with an

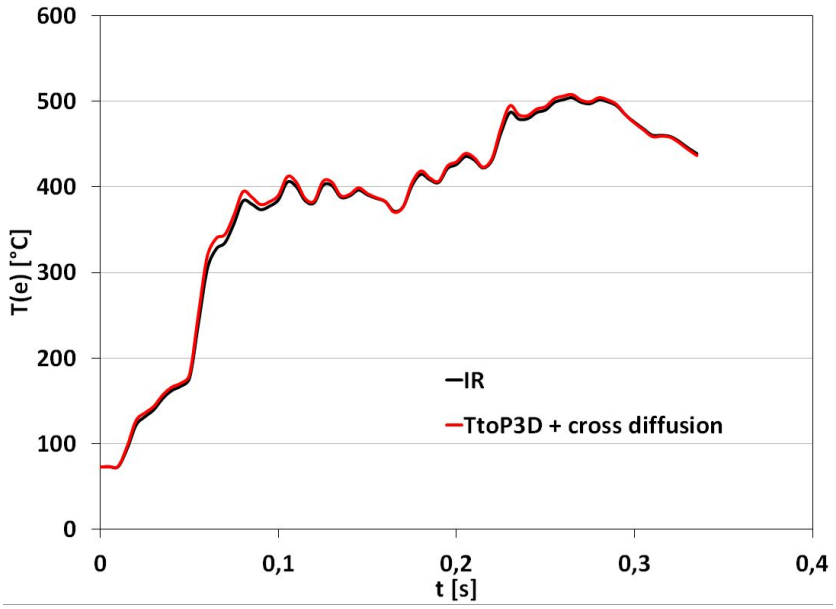

Figure 5.3.4: ANSYS comparison of TtoP3D for shot #36757 in 3D

average error lower than 2% for the most time of the discharge.

As a final analysis performed with ANSYS, the heat penetration depth has been analyzed by studying the heat diffusion inside the material. Fig. 5.3.6 shows the entire slab simulated by TtoP3D(2D) at the end of the discharge when all heat has been deposited on the surface. It is possible to see that the heat is complited absorbed by the sample and never reaches the opposite side of the material.

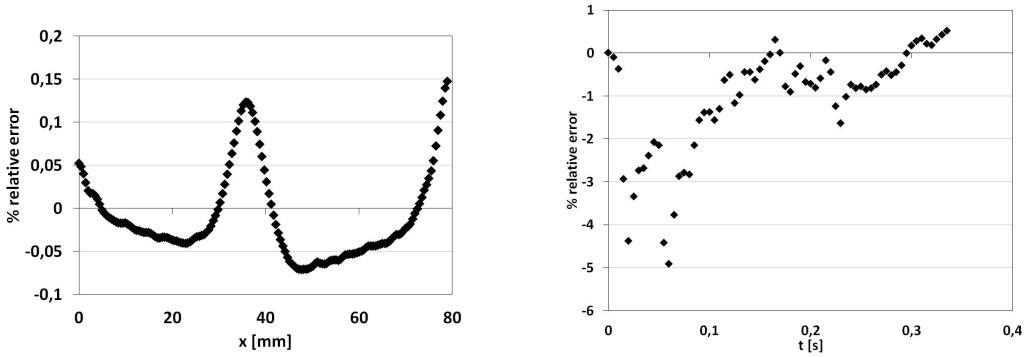

(a) TtoP3D(2D) vs THEODOR (b) TtoP3D(3D) vs IR

Figure 5.3.5: Relative error of the temperature calculated by ANSYS from the codes heat fluxes

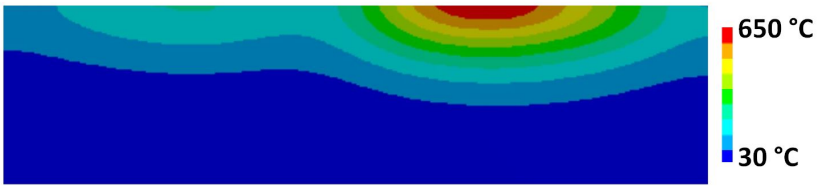

Figure 5.3.6: ANSYS comparison of TtoP3D for shot #36757 in 3D

5.4 Experimental setup

The edge of the RFP is a chaotic region dominated by instabilities, whose dynamics and properties are not yet completely understood. One of the aims of this thesis was to investigate the heat flux properties of the plasma edge at RFX-mod. For this purpose three different limiters were inserted in circular deuterium RFP plasma, recording the heat imprint with an infrared camera and then analysing it.

5.4.1 Samples

The samples exposed to the plasma were graphite tiles differing in shape and type of graphite:

- one roof-shaped (non-optimized geometry), with a corner in the center of the tile, made of RFX-mod standard graphite 5890-PT, fig. 5.4.1a
- one curved (optimized geometry), without any plasma incident corners, made of RFX-mod standard graphite 5890-PT, fig. 5.4.1b
- one curved (optimized geometry), made of graphite IG-15 with enhanced heat conductivity.

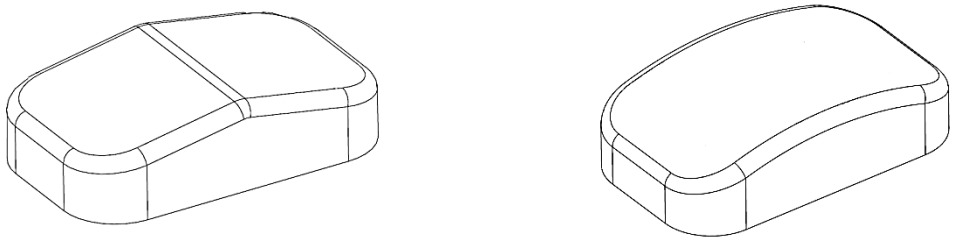

(a) Corner (b) Curved

Figure 5.4.1: Design of the two sample geometries

In table 5.4.1, relevant technical data are reported for the two different graphites used.

The samples were mounted at the top of a remote handling tool, inserted in the vacuum chamber through a pipe and aligned with the FW. The setup

sample #	Graphite	ρ [Mg/m^3]	C [J/(Kg*K)]	α [10^{-5}m^2/s]		
				0 °C	500 °C	1000 °C
1-2	5890PT	1.75	710	8	4.9	3.3
3	IG-15	1.9	710	10.5	7.4	4.2

Table 5.4.1: Graphites technical data

design is the same of the experiments with the LISA samples exposed in section , fig. . From this position the samples could be inserted up to 12 mm inside the chamber, increasing the interaction with the plasma and acting as limiters. Only the data relative to the samples with optimized curved geometry were considered in the analysis that follows.

5.4.2 Plasma conditions

Plasma current (I_p)	600÷1000 kA
Density (n_e)	$< 4 \cdot 10^{19}$ m^{-3}
Density (n_e/n_G)	<0.5
Process Gas	D
Reversal parameter ($F(a) = B_t(a)/ < B_t > (a)$)	$0 \div -0.12$
Limiter insertion	$0 \div -0.12$ mm

Table 5.4.2: Plasma parameters

Different plasma conditions have been explored to maximize the parameter range taken into account, as shown in table 5.4.2. Please note that the values shown are averaged during the current plateau of the discharge, single frame values may vary very much from the ones reported but are not significant for the subsequent analysis.

5.4.3 IR camera setup

Model	FLIR A655sc
Pixel resolution	640x120
Field Of View	25°x19°
Focal distance	12 mm
Frame rate	200 Hz
Detector pitch	17 μm
Spectral range	7.5÷14 μm
Accuracy	±2%
Temperature range	<2000 °C
Spatial resolution	1 mm

Table 5.4.3: IR camera parameters

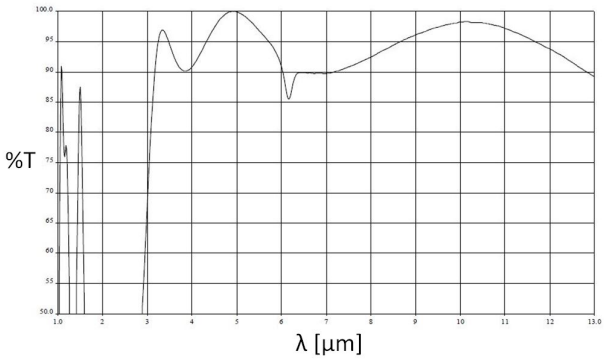

Figure 5.4.2

Infrared camera parameters are shown in table 5.4.3. The camera sees the plasma through a ZnSe window, Se is transparent to IR light but Zn overlayers needed to be applied to reduce the reflectance and enhance its transmittance in the IR spectrum, shown in fig. 5.4.2 as a function of the incident wavelength. When considering the impact that this added window has on the measurement, it can be absorbed by the atmospheric term of eq.

5.2.10 since no distinction can be made between the plasma and the window from an experimental point of view.

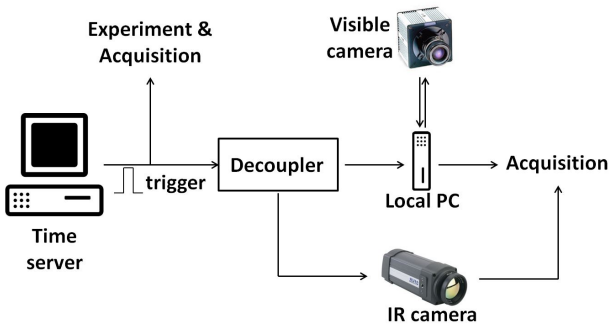

Figure 5.4.3: Schematic of the trigger and acquisition system

The camera starts recording images upon arrival of the TTL signal, which is split by an optical decoupler also to the visible camera, that triggers the experiment and the acquisition system and streams its output directly to the acquisition server through a dedicated 1 Gb ethernet connection. The camera and global measurement parameters as the temperature range, acquisition times, object emissivity, environment temperature, etc. can be set from a remote computer using a graphical sotware interface.

5.4.4 IR camera calibration

The IR camera has been received calibrated with a blackbody source from manufacturer. An adequate calibration for the experimental conditions experienced would require heating the graphite up to temperatures of the order of the 1000 °C reached in the experiments which are far above the thresh-

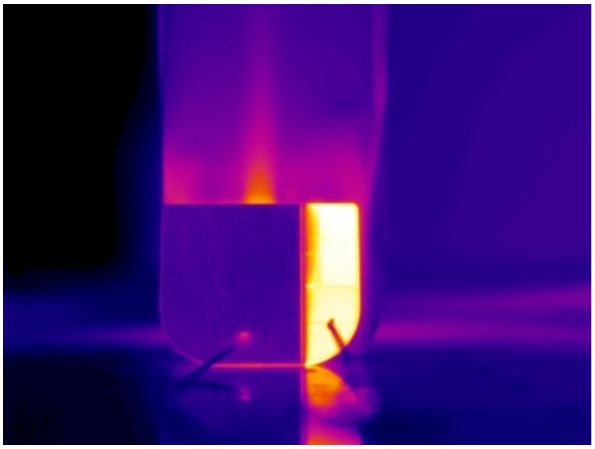

Figure 5.4.4: IR calibration using a LISA sample

old at which it oxides in an air environment. Therefore a dedicated vacuum chamber was required along with a heating system able to reach the dictated sample's surface temperature, or alternatively to insert a blackbody emitter in the RFX-mod vacuum chamber instead of the samples and perform an in situ calibration. Unfortunately such calibrations have not been possible due to experimental time constraints and the lack of dedicated instumental supplies. However, the camera has been widely tested in laboratory conditions before its employment.

A set of measurements has been performed using a LISA sample to sperimentally determine the emissivities of the deposited tungsten and of the graphite, being the same of the RFX-mod first wall and of one limiter sample. A heater was used to increase the sample's surface up to $\sim 120\,^{\circ}\mathrm{C}$, temperature at which it was removed and two thermocouples were put in contact with the two portions of the surface, as shown in fig. 5.4.4. Temper-

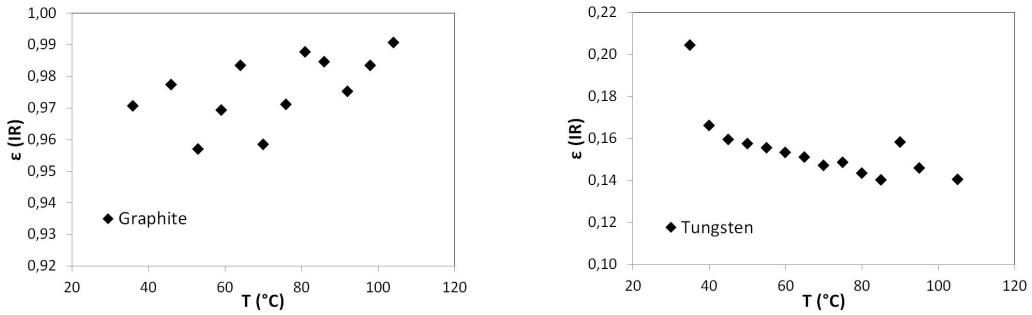

(a) Graphite (b) Tungsten

Figure 5.4.5: Measure of the emissivities of LISA sample

ature was recorded in the cooling phase at equal intervals of 5 °C and the emissivity was calculated backwards taking the temperature recorded by the thermocouples as input. This calculus was performed inverting the formula used by the camera to calculate the temperature, that takes into account the absolute measured value, atmospheric parameters as the air temperature and humidity and all the internal parameters of the camera useful to this calculation. Since the emissivity of tungsten is expected to be low, as seen in table 5.2.3, a high reflectance value is expected so particular attention was paid to avoid possible reflections of external heat sources as the human bodies.

The resulting emissivities are presented in fig. 5.4.5 for the temperature range considered. The emissivity of the graphite is roughly constant around an average of about 0.98, while the values for the tungsten are around 0.15 and both cases show an uncertainty of ± 0.01. In the tungsten case it is possible to see a slight increase in the emissivity at the lowest temperatures due

to the fact that, despite all experimental precautions, at temperatures close to the environmental one, the reflection from the surroundings constitues a large portion of the sample's radiated power and a slightly smaller precision is to expected. This effect is not seen in graphite because, with an emissivity of 0.98, only the 2% of the power coming from the surrounding can be reflected resulting in a negligible contribution. In experimental conditions, the temperature difference between the limiter and the rest of the wall can be of hundreds of degrees, allowing the neglect of reflections from other parts of the wall.

5.5 Data analysis

The IR images recorded during the experiments were post-processed using a number of software tools that tackled different aspects of the analysis. The main steps involved are:

- access to data in the data server;
- synchronization of the diagnostic used;
- reconstruction of plasma position using magnetic diagnostics;
- conversion from surface temperature to heat flux;
- computation of heat fluxes on the limiters and heat decay length;

- evaluation of correlations between IR measurements and plasma parameters both during single shots and across the database.

5.5.1 Software tools integration

Ad hoc IDL routines have been written in order to integrate all the available software tools. The first step was running the routine (described in section 5.5.3) that reconstructs the plasma position during the entire disharge in the toroidal geometry. After this, a main program was run to perform the following steps one disharge a time:

1. import the pre-saved output of the magnetic reconstruction routine;
2. access the server data and import the signals of the relevant diagnostics (IR and visible images, plasma current, density, ohmic power, etc.) relative to the selected discharge;
3. select the optimal time window to be considered (plasma current $>$ threashold = 30 kA) - needed because all shots can have different time lengths;
4. call THEODOR code (described in section 5.3.1) to perform the inverse heat calculation for the limiter area;
5. calculate heat fluxes for relevant areas and heat decay lengths;
6. compute the distance between the plasma and the limiter at any time;

7. save all the extracted data and parametes on an output file for further analysis.

5.5.2 Time synchronization

One of the very first steps is to homogenise the time scales of the signals coming from different diagnostics to make them comparable ($\Delta t(n_e) = 2{\cdot}10^{-6}$ s, $\Delta t(I_t) = 5 \cdot 10^{-5}$s, etc.).Since the 200 Hz sampling rate of the IR camera is the lowest among all the diagnostics, all the other measures have been averaged in time intervals of 5 ms coincident to those of the camera. The relative low framing rate of the camera is also reflected in an issue with the trigger: when the camera is switched on, it is continuously capturing images and the square wave signal that triggers the start of the recording can arrive at any time inside the 5 ms window of a frame. The acquisition of the camera can thus start with up to a 5 ms delay with respect to the trigger, resulting in a random time mismatch with the other diagnostics that has to be handled on a case by case basis. The problem is solved comparing the IR signal with the visible camera that has a five times higher sampling rate: considering the average values of a small area, peaks of interaction with the plasma should be coincident and that gave the correct time shift with respect to the trigger, as shown in fig. 5.5.1. Of course, the delay can have any value from 0 to almost 5 ms so the two signals have been correlated for the whole discharge in order to determine if a delay had to be applied.

A routine was written in order to compute correlations between diagnos-

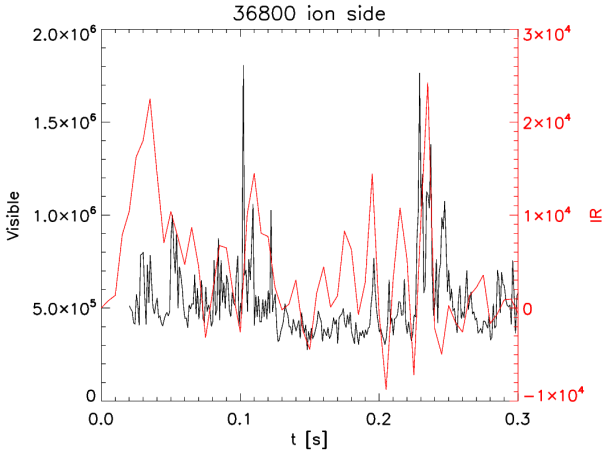

Figure 5.5.1: IR (red) vs visible (black) signals: a ∼5 ms shift can be seen on the same peak as measured by the two diagnostics

tics data during a shot, such as the plasma distance from the limiter with the heat flux, while a second program calculated the averages of these values during the shots to make correlations across the database. All the data extracted correspond to a time interval where the plasma current is larger than a threashold value of 30 kA, while when considering shot averages this interval is further reduced in order to avoid unstable phenomena which may affect the beginning or the end of a discharge, roughly correspondig to the time interval between 50 and 250-300 ms.

5.5.3 Magnetic reconstruction

Plasma position is a key parameter to be estimated when considering plasma-wall interactions, because it allows the correlation and validation of events seen by other diagnostics with plasma dynamics. This task has been per-

formed by routines developed and commonly used at RFX-mod [73, 74, 75, 76].

The physics treatment of the problem starts considering a force-free equilibrium model to describe an RFP plasma, to which a perturbative approach is applied considering that all quantities are constituted by the sum of a zeroth-order dominant axisymmetric component and a non-axisymmetric one as:

$$\mathbf{J} \times \mathbf{B} = 0 \qquad \nabla \times \mathbf{B} = \mu_0 \mathbf{J} \qquad \nabla \cdot \mathbf{B} = 0 \tag{5.5.1}$$

$$\mathrm{X}(\mathrm{r}, \theta, \phi) = \mathrm{X}_0(\mathrm{r}, \theta) + \mathrm{x}(\mathrm{r}, \theta, \phi) \tag{5.5.2}$$

where the coordinates refer to the zeroth-order magnetic surfaces, so r is the radius of the magnetic surface, θ the poloidal-like angle and ϕ the toroidal angle coincident with the one described by machines coordinates. Fig. 5.5.2 illustrates this coordinate system for a magnetic surface (solid line) inside the first wall (dotted line).

Adopting a convenient gauge, it is possible to write a simplified equation for the magnetic field $\mathbf{B}$ as a function of the toroidal and poloidal covariant components, F and Ψ, of the vector potential:

$$\mathbf{B} = \nabla \mathrm{F} \times \nabla\theta - \nabla\Psi \times \nabla\phi \tag{5.5.3}$$

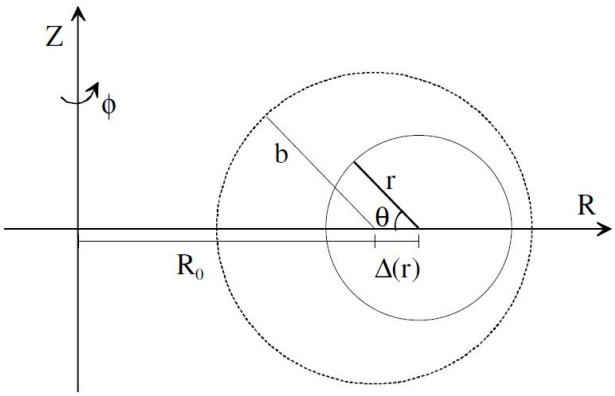

Figure 5.5.2: Magnetic surfaces coordinate system

$$\Psi(r,\theta,\phi) = \Psi_0(r) + \sum_{n\neq 0,m} \psi^{m,n}(r) e^{i(m\theta - n\phi)} \tag{5.5.4}$$

$$\mathrm{F}(\mathrm{r},\theta,\phi) = \mathrm{F}_0(\mathrm{r}) + \sum_{n\neq 0,m} f^{m,n}(r) e^{i(m\theta - n\phi)} \tag{5.5.5}$$

where Ψ_0 and $\mathrm{F}_0$are the toroidal and poloidal flux (referred to the zeroth-order magnetic surfaces) divided by 2π, and $\psi^{m,n}$ and $f^{m,n}$ are the perturbation components. The local shifts from equilibrium are derived from a linear approximation of ideal MHD equations and are linked to the computed fluxes by the relation:

$$\xi_a^{m,n} e^{i\varphi^{m,n}} = \left[\frac{n f^{m,n} - m\psi^{m,n}}{m - nq} \frac{1}{\Psi_0'} \right]_{r=a} \tag{5.5.6}$$

where $\xi_a^{m,n}$ is the (m,n) harmonic of the radial shift at the plasma edge, which is given by the sum of all of its components as:

$$\xi^r(a,\theta,\phi) = \sum_{n>0,m} 2\xi_a^{m,n} \cos(m\theta - n\phi + \varphi^{m,n}). \tag{5.5.7}$$

For the purpose of this analysis, magnetic reconstruction has been performed using cylindrical coordinates instead of the toroidal ones because they produce very similar results but the computational time is much shorter using the cylindrical approximation. The routines described above have been used being aware of the limitations imposed for this specific case of study, that will be briefly discussed.

The first issue is that eq. 5.5.6 can diverge because the denominator tends to zero when considering $m = 0$ modes with shallow reversal parameter $F \simeq 0$, which is precisely the most common situation met in experimental conditions. During the analysis it has been noted that there were numerical problems that resulted in inconsistent values of the plasma position so the only possible solution was excluding $m = 0$ modes from the calculation and so taking into account only $m = 1$, introducing an unmeasurable source of error into the analysis.

The second issue is a geometrical one because the routines solve the above equations in a toroidal (or cylindrical) geometry, where no limiters or other solid objects can be inserted. Furthermore, a working hypotesis at the roots of the code is that the plasma is supposed to be in contact with the wall in one single point a time, which is the starting point from which the entire plasma surface is reconstructed. While this is not true in general as there could be

more contact points, it is certainly not true in the case of an inserted limiter that can not be taken into account in the reconstruction or in the geometrical boundaries, so at any time the plasma is assumed to be touching the wall *somewhere else* instead that on the limiter. The solution adopted on this case is subtracting the limiter insertion from the plasma-wall distance computed from the routine, for example in a shot where the limiter has been inserted 10 mm, this value is subtracted from the whole magnetic reconstruction output in the point where the limiter is present. A major drawback of this patch is that the calculated distance can be smaller that the limiter insertion, yielding a *negative* plasma-wall distance.

An alternative solution was explored to overcome this issue, considering only the poloidal cut of the plasma column at the limiter toroidal angle. The condition of contact with the wall was imposed only on that section by expanding (or contracting) the plasma LCMS until a single contact point was found, always considering the distance reduced by the limiter insertion. This approach has shown to be the less effective because every information on the correlation between the distance and the objects of the investigation as the heat loads and the decay length had been leveled out.

For these reasons an exact distance between the plasma and the limiter could not be obtained, but the values obtained still allowed some more general considerations of plasma proximity to the limiter.

5.5.4 Parallel heat flux properties

The heat flux computed by the codes THEODOR and TtoP3D, q_{dep}, is the total power density incident to the limiter and it is computed without taking into account the system geometry. In a purely toroidal geometry, with no limiters inserted, the total power deposited on the first wall would equal the input ohmic power for equilibrium reasons. This heat flux is due to diffusion along the direction perpendicular to the magnetic field at the edge that defines the LCMS and can be estimated dividing the ohmic power P_Ω by the plasma surface but since this is not known, it can be approximated by the area of the first wall, obtaining:

$$q_{dep,\perp} \approx \frac{P_\Omega}{A_{FW}} \approx \frac{P_\Omega}{40m^2}. \tag{5.5.8}$$

Standard values during a discharge are $P_\Omega = 10 \div 20$ MW, leading to an estimate for the perpendicular heat flux of $q_{dep,\perp} = 200 \div 500\,\mathrm{KW/m^2}$. This component is the one associated to power losses because it is directed "outside" the plasma.

When a limiter is inserted, it changes the plasma shape forcing the LCMS to be at the position of contact with it. The perpendicular component remains equal to the previous case, but now the limiter intersects also the flux of particles travelling in the direction parallel to the magnetic field at the edge which are those with the highest energies that contribute to sustain the magnetic configuration.

The intensity of the heat parallel component can be obtained from Pitagora's theorem:

$$q_{dep,\parallel} = \sqrt{q_{dep}^2 - q_{dep,\perp}^2} \tag{5.5.9}$$

where $q_{dep,\perp}$is the one calculated above and q_{dep} is the one obtained from IR measurements. In an average discharge, heat depostion has been found to be of the order of $q_{dep} \sim 10\,\mathrm{MW/m^2}$, allowing to neglect the perpendicular term since it is more than an order of magnitude smaller, and obtaining:

$$|q_{dep,\parallel}| \approx |q_{dep}|. \tag{5.5.10}$$

Finally these values must be corrected by the angular tilt of the limiter because the heat flux hits the surface with an angle that corresponds to α=10° for the angular sample while for the curved sample it runs in the range $0° \leq \alpha \lesssim 15°$ and is taken into account according to the formula:

$$q_{\parallel} = \frac{q_{dep,\parallel}}{sin\alpha} \tag{5.5.11}$$

The ratio on the right hand side diverges for $\alpha \to 0°$ so, even if correctly computed by the codes, angles smaller than $\alpha < 2°$ are not considered during the analysis. The underlying physical reason for this limit is that for $\alpha \to 0°$ the heat flux is almost parallel to the limiter surface and so only a very small fraction of it will be deposited onto the surface, resulting in an infinite flux incident on an infinitesimal surface, considering the parallel heat flux as only

heat source. In this limit the perpendicular heat flux can be studied as it is the relevant quantity to be considered, along with heat diffusion from the near peak heat load.

An important property to be studied about how the plasma-wall interaction is the behaviour of the power heat load that exits the plasma and is deposited on the FW. Its euristic description found in literature is an exponential decay of the heat from the incident point on the wall, this being the vertex of the limiter for the present case or the strike point in a divertor scenario (see for example [77]), given by:

$$q_{\parallel}(r) = q_{\parallel}(r_0) \exp\left(\frac{r - r_0}{\lambda_q}\right) \tag{5.5.12}$$

where r is the radial distance from the plasma, $q_{\parallel}(r_0)$ the maximum if the heat flux that is computed at $r = r_0$ and λ_q is the heat decay length. λ_q is a key phisical parameter to be studied because it is the one that defines how fast the heat flux decays, and is also linked to physical properties of the plasma edge as the diffusion coefficient.

5.6 Results

Data analysis has been performed on the database to correlate results obtained during the RFP deuterium campaign at RFX-mod. It has been a demanding task because this was the first attempt to measure the heat decay length of an RFP plasma using an IR camera, so experimental conditions

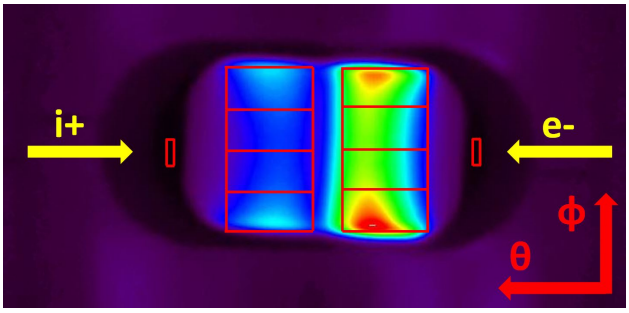

Figure 5.6.1: Sub-division of the limiter surface

Symbol	Description	Range [mm]
d	Distance between the plasma edge and the limiter	$-5 \div 20$
d_rscl	Rescaled distance between the plasma edge and the limiter	$0 \div 5$
r	Radial distance from the limiter vertex towards the FW	$0 \div 6$
x	Distance from the limiter vertex towards its edge along the poloidal direction	$0 \div \pm 40$
ins	Distance between the limiter vertex and the FW	$4 \div 12$

Table 5.6.1: Symbols table

were not yet optimized and almost all software tools were developed at the need.

A particular effort was on the analysis of the heat decay length and the (a-)symmetries in the heat deposition pattern and in the attempt of finding correlations with main plasma parameters as the electron density and the plasma position. Most discharges were performed at reversal parameter $F \approx 0$, where the edge magnetic field is purely poloidal and the sample was in the best conditions to act as a limiter, allowing a field line impinging on

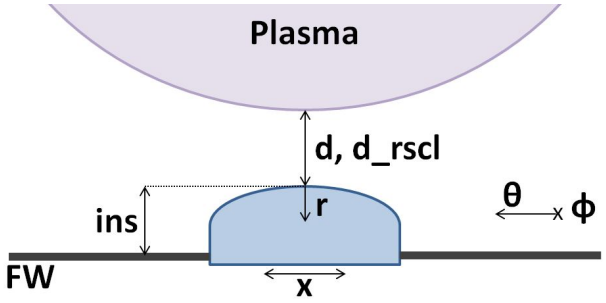

Figure 5.6.2: Graphic representation of the symbols used

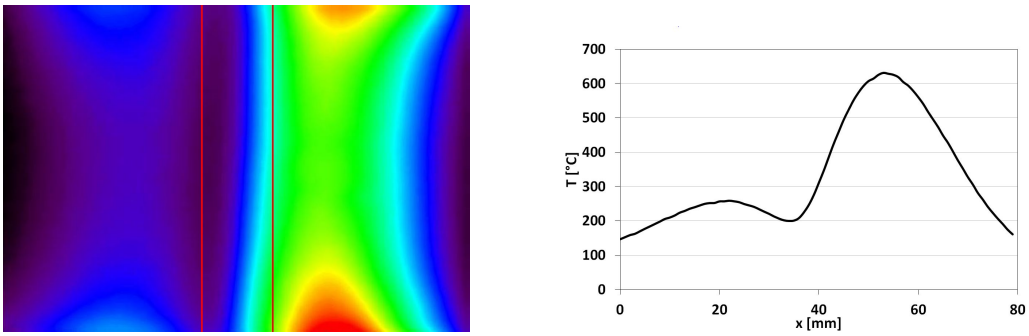

(a) Temperature map on the entire surface

(b) Typical temperature profile along a poloidal line

Figure 5.6.3: Temperature on the limiter from IR measurement

one side to hit also the other side when trying to close on itself. Due to the small dimensions of the sample, this was unlikely to happen at larger of F, where a field line would hit the sample diagonally on one side and never close on the other side. The drawback of this choice is that $F \approx 0$ implies large numerical uncertainties in the plasma position, as described in section 5.5.3. In addition, the instabilies that characterize the plasma edge origin large local displacement of the plasma column from its equilibrium, causing non-constant interactions between the plasma and the samples and

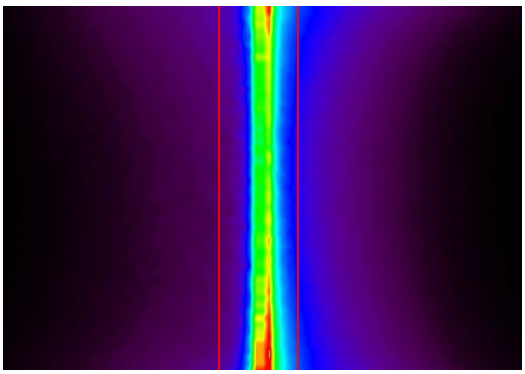

Figure 5.6.4: $Q_{\parallel}$ conversion

so preventing the limiter from acting as such.

In order to have a more detailed analysis, the sample IR image has been divided into 8 areas as shown in fig. 5.6.1. Temperature and heat fluxes have been averaged in these areas and compared for asymmetry analysis, while the heat decay length has been computed on every line in both the ion and the electron drift side. The direction of the particle flux and the toroidal coordinates are also presented in the image. The background value, obtained from the two small areas near the sample, has been subtracted from the measurement in order to take into account the background measured by the camera and plasma emission, and it has been corrected for the sample emissivity and the window transmittance.

As a reference for the results of the analysis discussed in the following sections, table 5.6.1 and fig. 5.6.2 describe the symbols used, along with the ranges they spanned.

The conversion from temperature to heat fluxes, computed according the

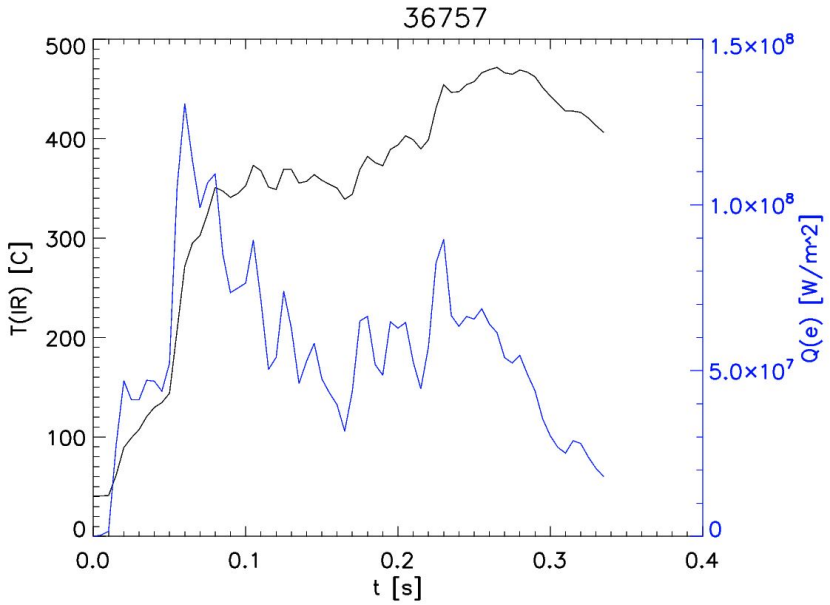

Figure 5.6.5: T(e) and Q(e) during discharge #36757

description in section 5.5.4, is now presesented. As a starting step, the perpendicular component of the heat flux has not been taken into account because it is negligible according to the discussion presented in section 5.5.4. In the conversion from temperature to the parallel component of the heat flux, the central slice of the limiter has been excluded from the analysis because the flux and the surface are parallel at the vertex of the limiter, causing eq. 5.5.11 to diverge as the angle α between them tends to zero. For this reason, the part of the sample corresponding to values of $\alpha < 2^\circ$ have been excluded from calculation, which is the area between the two red lines in fig. 5.6.3a and fig. 5.6.4.

Fig. 5.6.3 shows a frame from the IR camera representing a typical temperature map on the limiter and a relative temperature profile along

a poloidal (horizontal in the picture) line. The relative $Q_{\parallel}$ calculated for that instant is presented in fig. 5.6.4. Due to the changing incident angle along the sample, such a peaked parallel heat load can originate a completely different temperature pattern on the limiter, which is maximized when an appropirate ratio between the heat flux and the angle is found. A comparison between the temperature and the incident heat flux during a discharge is shown in fig. 5.6.5 where the quantities have been averaged over the electron side area of the limiter. In the following discussion, only graphs relative to the electron side will be presented for conciseness because tipically the same behaviour characterizes also the ion side. Should this condition no longer hold, it would be shown.

5.6.1 Plasma position

In this section a discussion on the estimate of plasma position is presented. The exact values could not be calculated due to the issues already discussed in section 5.5.3, nevertheless the output of the magnetic reconstruction routines gave important information that can be used in this discussion being aware of the errors that affect such numbers.

The sampling rate of the magnetic coils used for plasma reconstruction is 1 kHz, so for every frame of the IR camera 5 points had to be mediated. Fig. 5.6.6 shows the distance d of the plasma edge from the limiter vertex during an entire discharge, the error bars represent the range explored by d in the 5 ms averaging time of every point. The example shot is #36745, that

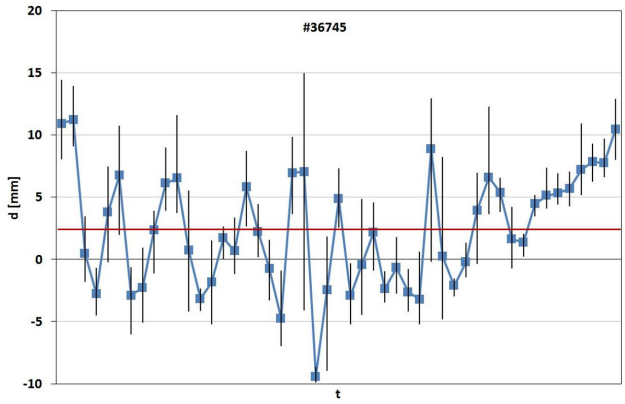

Figure 5.6.6: Plasma distance from the limiter during a discharge with its average in red

is a 800 kA discharge in which the limiter was inserted by 10 mm.

It can be noted that the plasma is very much oscillating and even if the average distance calculated is d =2.4 mm, the plasma touches the limiter in almost half of the times. This further increases the uncertainty if the plasma studied is a truely limited plasma or not, raising the need for further investigation.

The experimental parameters spanned from low limiter insertion and low plasma current discharges to high insertion and high current ones and clear examples were found at the far ends of these ranges showing that both limited and non-limited plasmas are present in the database. Shot #36698 is a 600 kA discharge with 4 mm insertion that shows almost no interaction between the plasma and the limiter (fig. 5.6.7a), while a negative average distance is calculated for shot #36758 (fig. 5.6.7b), a 900 kA discharge with 12 mm insertion, meaning that the limiter has been wetted by the plasma for almost

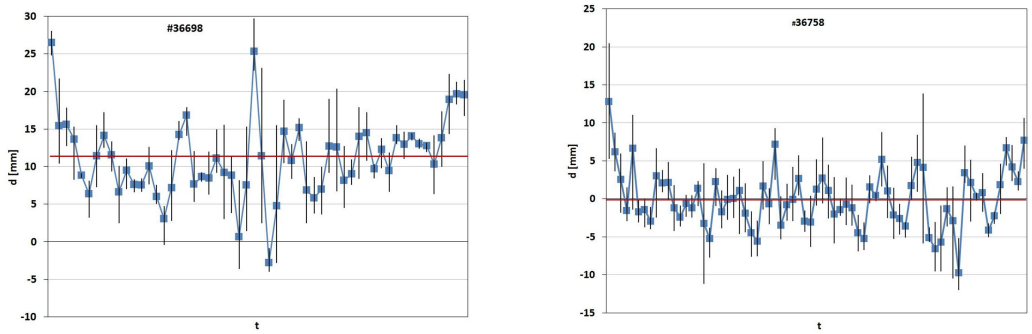

(a) #36698 (b) #36758

Figure 5.6.7: Distance between the plasma and the limiter in two opposite situations

all the duration of the discharge.

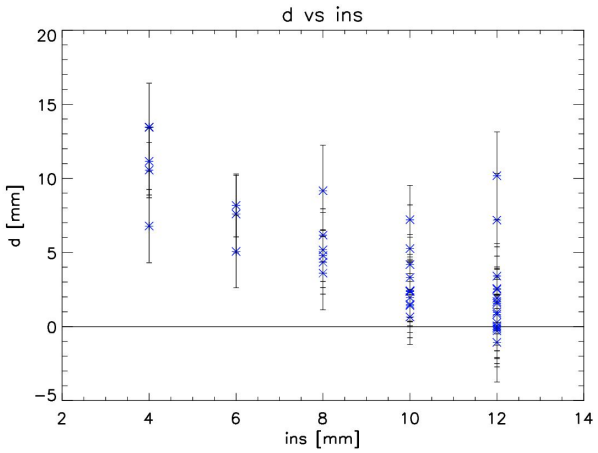

Figure 5.6.8: Discharge averaged d as a function of limiter insertion

The dependence of the average distance from the limiter insertion, averaged during a shot, is shown in fig. 5.6.8, while a comparison between the two ways of computing the distance d and d_rscl, as discussed in sec. 5.5.3, is presented in fig. 5.6.9. It is possible to note that d is not constant but

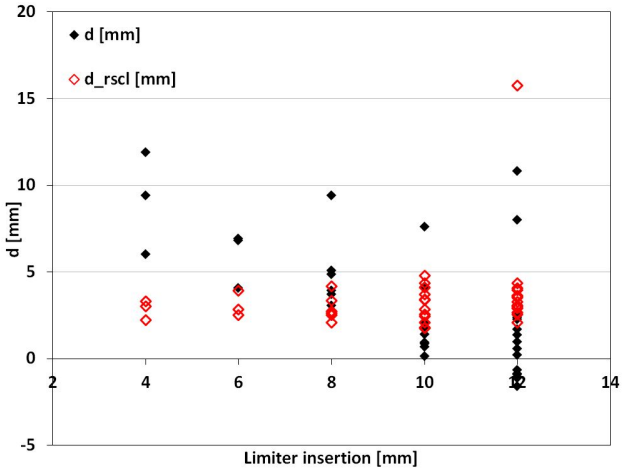

Figure 5.6.9: Comparison of d and d_rscl as a function of limiter insertion

decreases almost linearly with the limiter insertion, which is a possible indication that for the lowest values the sample is not inserted enough to actually limit the plasma since there is a finite distance between them preventing the sample from forcing the position of the LCMS. It is also possible to recognize the loss of information of d_rscl compared to d because it is almost constant across the entire database: this is probably due to the calculation method ford_rscl that forces the plasma diameter to be of almost the same dimension of the vacuum chamber's, not allowing a non-touching plasma in the considered poloidal section, and thus preventing larger distances from being calculated.

A more complete discussion on the distinction between the limited and non-limited plasma cases and on the comparison between d and d_rscl will be found in the following paragraphs where a more complete data analysis is presented about the physic parameters studied.

5.6.2 Heat decay length

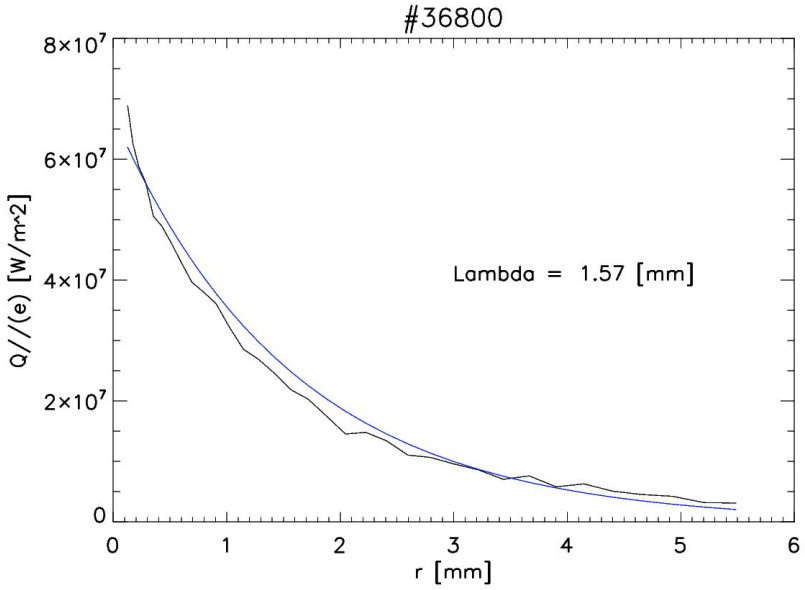

Figure 5.6.10: Exponential interpolation (blue) of heat along r from experimental data (black)

One of the most important parameters of the plasma edge related to heat fluxes is the heat decay (or e-folding) length, introduced in section 5.5.4. It describes the exponential decay of the parallel component of the heat flux from the LCMS to the wall in the radial direction. An example is shown in fig. 5.6.10, where the parallel heat flux impinging on the electron side of the limiter si plotted as a function of the radial distance r from the magnetic axis. An exponential fit has been performed to extract the value of λ_q for this case and it has been plotted on the graph to show the goodness of the interpolation.

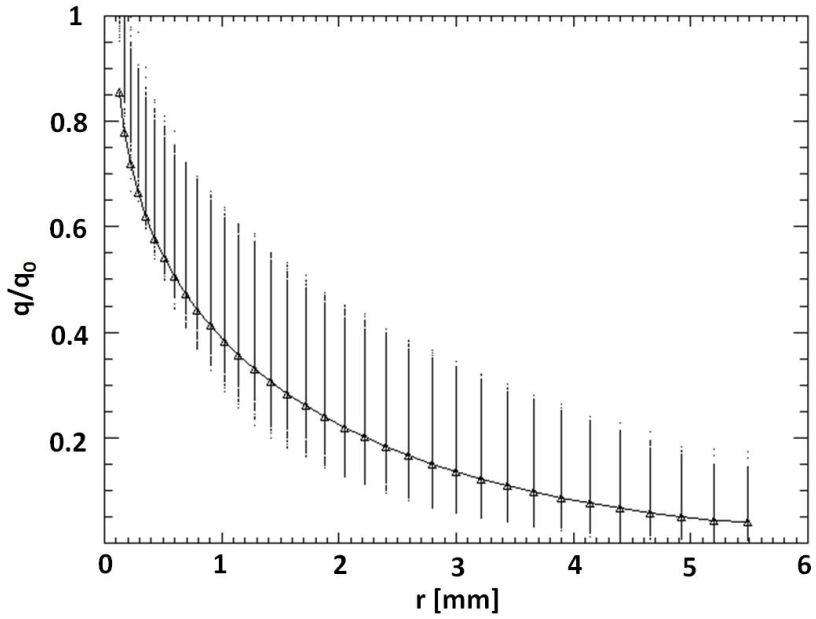

Figure 5.6.11: Average value of $\lambda_q(e)$ during shot #36757

The behaviour of λ_q has been investigated across the available parameters because the heat decay length has never been studied in the case of an RFP plasma before.

In order to obtain a single value for λ_q (one for the electron and one for the ion side) for an entire discharge, all the values have been averaged on the sample area and on all time frames. This is shown graphically in fig. 5.6.11 where the normalized heat flux on the electron side is plotted against r and the average curve, corresponding to the average $\lambda_q(e)$, is drawn as a solid line. The vertical alignement of the points is due to the pixel discretization of the camera.

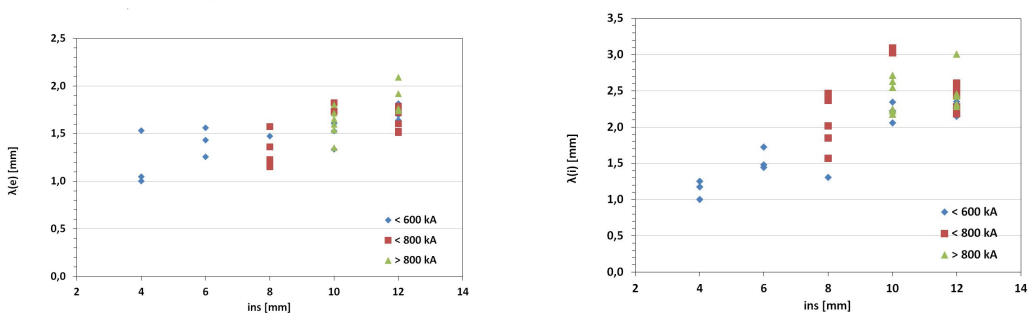

(a) $\lambda_q(e)$ vs limiter insertion

(b) $\lambda_q(i)$ vs limiter insertion

Figure 5.6.12: Heat decay length vs limiter insertion for the electron and ion side

Different values of λ_q have been found depending on the side considered and the limiter insertion, in particular it has been found to increase with the insertion and to be larger in the ion side, as shown by fig. 5.6.12. The dependence from density normalized to the Greenwald one has also been analysed and is show in fig. 5.6.13. λ_q has been found to be constant with respect to the density, but it has different values depending on the limiter insertion: for the largest values (ins=10-12 mm) $\lambda_q(e) = 1.69 \pm 0.16$ mm and $\lambda_q(i) = 2.44 \pm 0.27$ mm, while for smaller values (ins=4-8 mm) $\lambda_q(e) = 1.31 \pm 0.20$ mm and $\lambda_q(i) = 1.64 \pm 0.46$ mm.

The transition between the two cases happens abruptly and the threshold is evidently represented by the value of ins = 8 mm, as shown by fig. 5.6.13b. Furthermore, the fact that in one case $\lambda(e)$ and $\lambda(i)$ are clearly separated while in the other they seem to even overlap suggests the possibility thaet a different underneath physical situation is being considered.

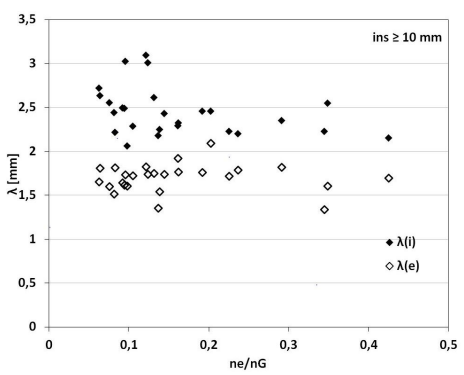

(a) λ_q vs n_e/n_G for limiter insertion $\geq$10 mm

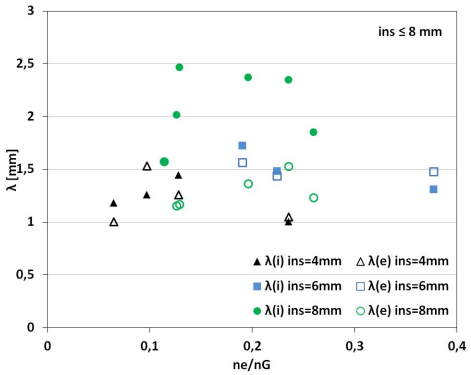

(b) λ_q vs n_e/n_G for limiter insertion $\leq$8 mm

Figure 5.6.13: Heat decay length vs normalized density

A duble decay length is a well known fact for tokamaks (see for example [78, 79, 80]) and the transition point is around $d = 5$ mm, but this does not seem to be the case of the present analysis for two reasons. The first is that the relative slopes of $\lambda_{q,near}$ and $\lambda_{q,far}$ are switched for tokamaks, in fact it is shown in literature that $\lambda_{q,near} < \lambda_{q,far}$, while the second reason deals with geometrical consideration of the experimental conditions. The radial extension of the limiter surface (i.e. the heigth of its vertex from the border) is of only 6 mm, which is smaller than the space needed for seeing a double λ_q as that reported for tokamaks. In addition, it has been previously shown that for the lowest insertions there is a strong indication that the plasma is not being limited by the sample, implying that the interactions recorded by the camera are with some random portion of the plasma edge that cannot be defined with the instrument used. Nonetheless the result obtained gives the

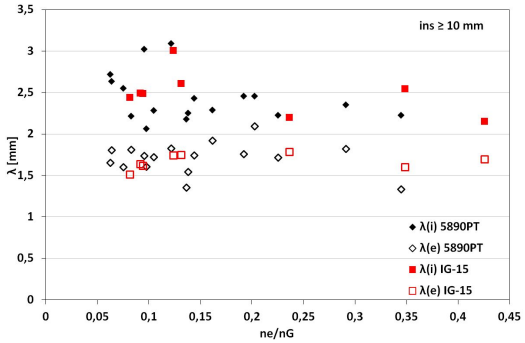

Figure 5.6.14: λ_q for the two graphites

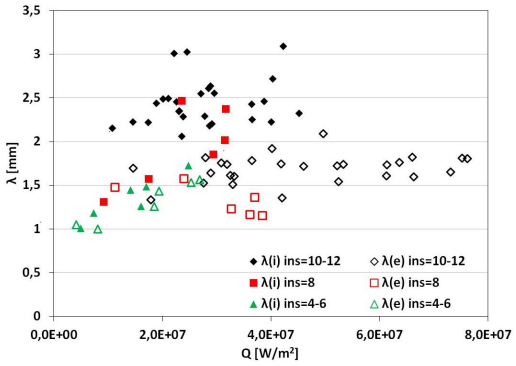

Figure 5.6.15: Dependence of λ_q from the heat flux

information that away from the LCMS the heat decay length of the electron and the ion side seem to average to the same value.

The plot of λ_q versus density has been also used for comparing the behaviour of the two graphites; IG-15 has only been tested for ins = 10, 12 mm due to experimental time constraints. No difference is found between the two materials because the short discharge duration ($<$ 400 ms) does not allow an appreciable surface diffusion, that would otherwise result in a flatter heat pattern for longer experimental times.

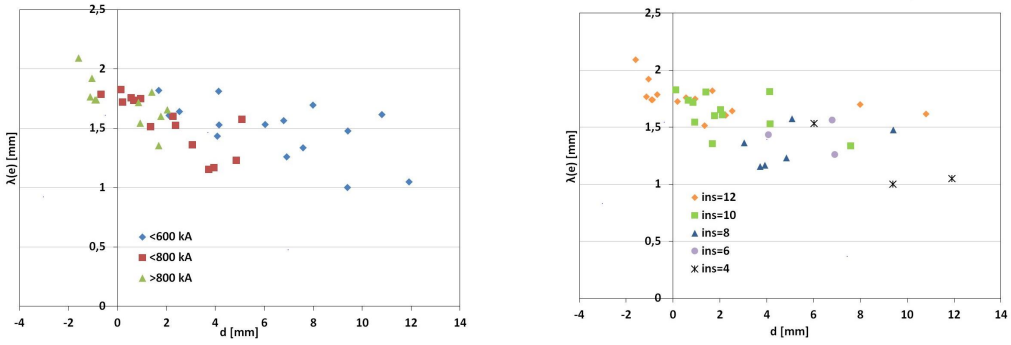

(a) Grouped by plasma current (b) Grouped by insertion

Figure 5.6.16: λ_q vs d

Fig. 5.6.15 shows the depence of λ_q from the incident heat flux, that is more pronounced for ins ≤ 8, while for higher values seems that the two quantities are unrelated. Fig. 5.6.16 shows the dependence from the distance, the two different values of λ_q can be seen as already discussed. A thing to be noted is that there are few shots that have an average negative d, this is due to the numerical approximations already discussed in section 5.5.3.

A weak dependence is found for λ_q from plasma current I_t and the total ohmic power P_{ohm} injected into the plasma, as shown in fig. 5.6.17a and 5.6.17b.

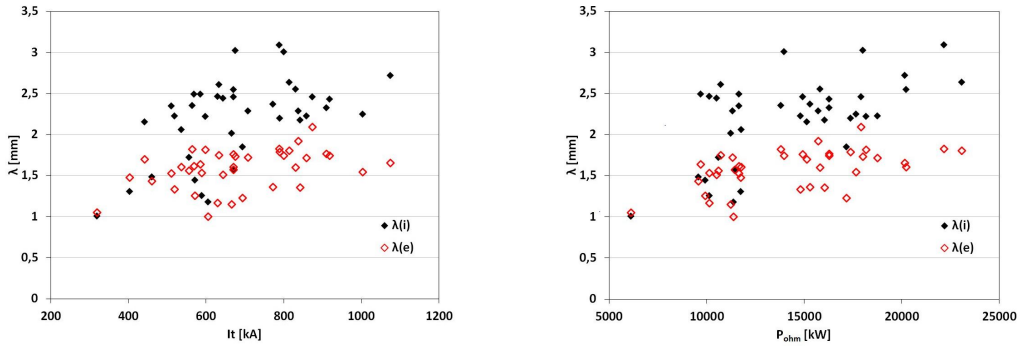

(a) λ_q vs I_t (b) λ_q vs P_{ohm}

Figure 5.6.17: Heat decay length vs plasma parameters

5.6.3 Heat fluxes

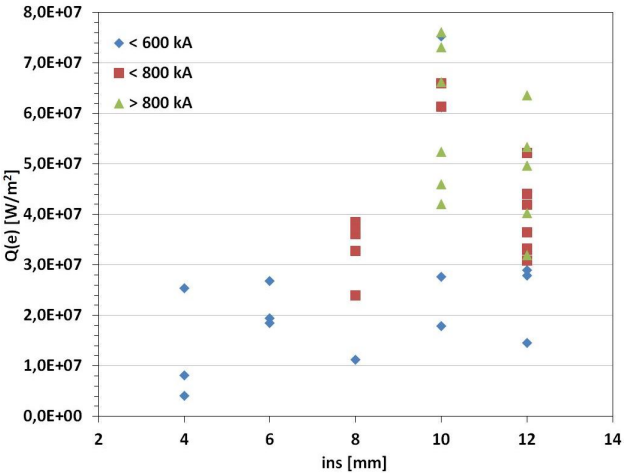

Figure 5.6.18: Dependence of the heat flux on the limiter insertion

The dependence of the heat flux on other experimental parameters has been investigated, finding an almost linear correlation with the plasma current (fig. 5.6.19a) and the total ohmic power (fig. 5.6.19b). Another correlation has been found between the average heat load deposited during a

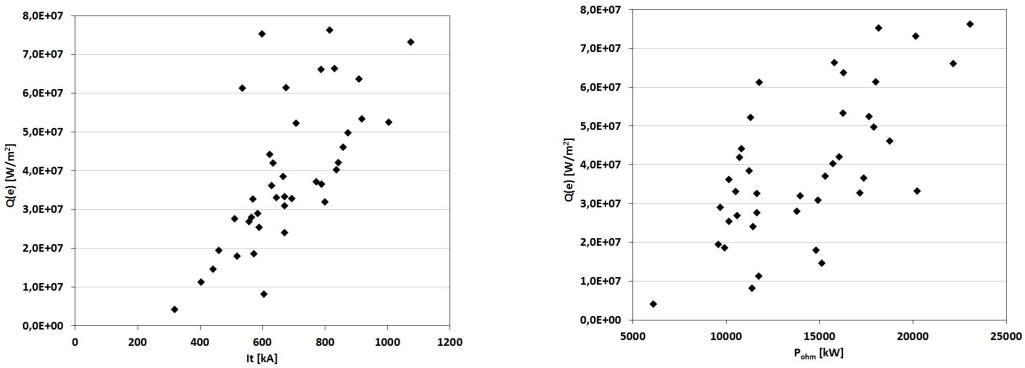

(a) Q(e) vs I_t (b) Q(e) vs P_{ohm}

Figure 5.6.19: Dependence of the heat flux on other parameters

discharge and the limiter insertion, as shown in fig. 5.6.18. This plot shows that the heat flux increases with the insertion suggesting, in agreement with fig. 5.6.8, that two different plasma scenarios may be considered for different insertions.

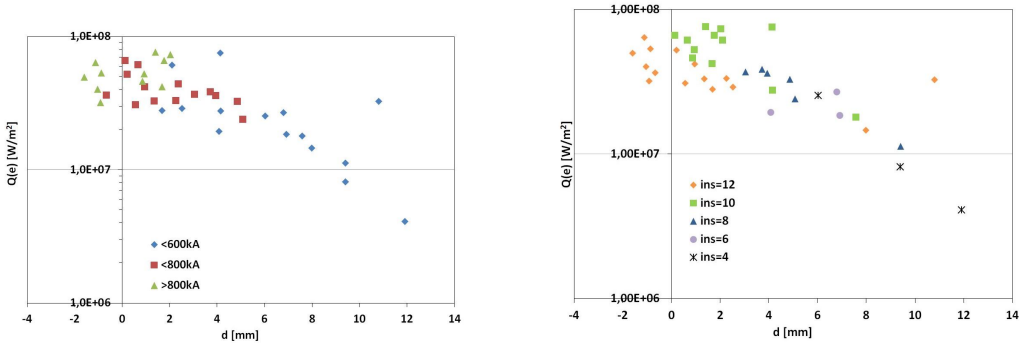

(a) Q(e) vs d, grouped by plasma current (b) Q(e) vs d, grouped by insertion

Figure 5.6.20: Dependence of the heat flux on d

Similarly to the analysis done for the decay length, the average heat flux has been plotted against the average plasma-limiter distance, as shown in

fig. 5.6.20a and fig. 5.6.20b. As to be expected, the discharges with smaller d are also the ones which have a higher heat load on the limiter because they are closer to the plasma and therefore undergo a more intense interaction, while the points at the highest d are the ones with the lowest insertion and correspond to low current discharges (small ins, small I_p $\rightarrow$small Q). Consistently with what already discussed about the possibility of a double λ_q, points seem to be divided into two groups depending on d, which can be interpolated by two different lines yielding two different heat decay lengths. The interpretation of this plot is in line with that given in the previous section.

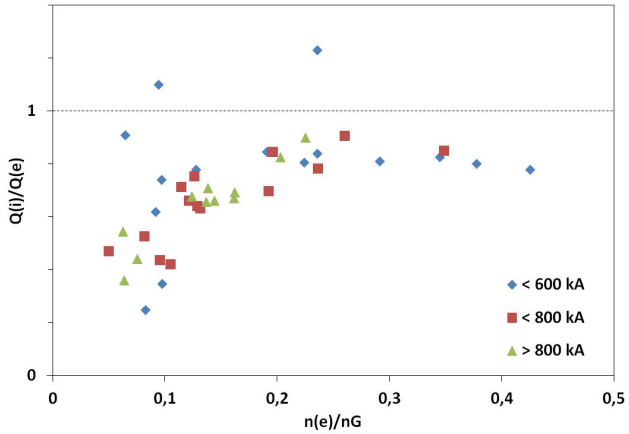

Figure 5.6.21: Dependence of the heat flux asymmetry on the normalized plasma density

Experimental evidence has been found in a strong asymmetry of the interaction between the ion and the electron drift side: the electron side was always been the most interacting with the plasma, with the highest surface temperatures. Comparing the averaged heat loads on the two sides with plasma parameters. a clear dependence has been found on the normalized

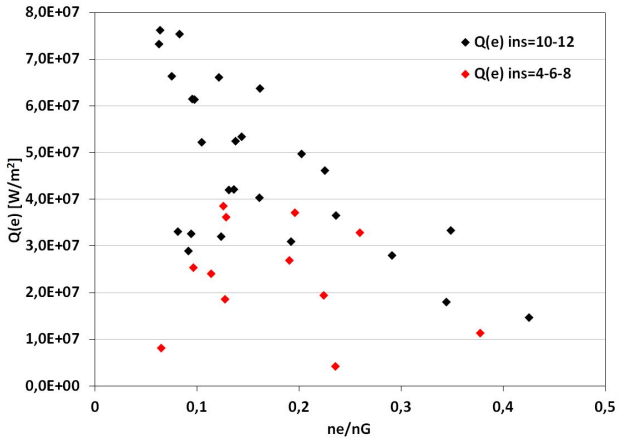

Figure 5.6.22: Q(e) vs n_e/n_G

plasma density n_e/n_G, as shown in fig. 5.6.21. The electron side almost always undergoes higher heat loads:\ while the asymmetry is small ($< 20\%$) for values of $n_e/n_G \gtrsim 0.2$, it grows as the density decreases reaching a maximum ratio of $q_i/q_e \sim 0.2$ at $n_e/n_G \sim 0.1$. There are three points that drop out of the collective behaviour but they fall in the category of low insertion and low current discharges so could be excluded from this first step analysis.

This strong asymmetric behaviour is caused by superthermal electrons, introduced in section . In the present experiment, the ratio of the heat flux along the parallel direction to the anti-parallel has been found to be $q_e/q_i \sim 1 \div 3$ at low densities, which is slightly lower than the literature range of $3 \div 12$. Fig. 5.6.22 confirms the inverse dependence of the heat flux on the electron side (the one due mainly to superthermal electrons) on the reduced density; once again the difference between the two limiter insertion ranges is shown, highlighting the different behaviour depicted.

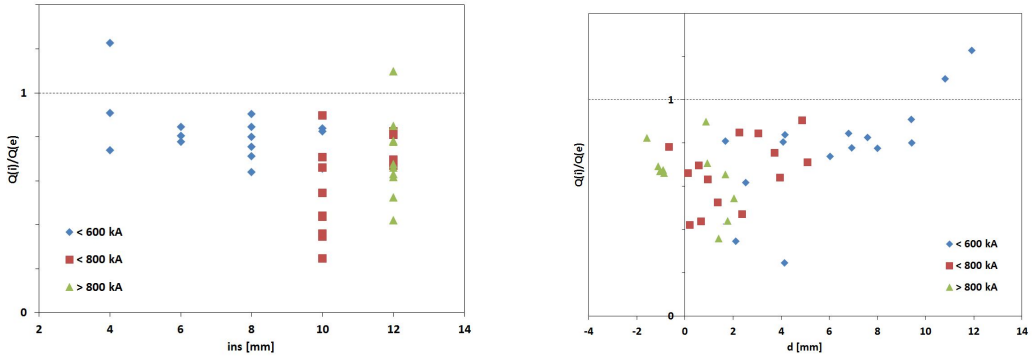

(a) Q(i)/Q(e) vs ins (b) Q(i)/Q(e) vs d

Figure 5.6.23: Dependence of the heat flux asymmetry on other parameters

The heat flux asymmetry increases with the limiter insertion (fig. 5.6.23a) and shows a consistent behaviour when plotted against the distance (fig. 5.6.23b), recalling that higher insertions imply smaller distances (fig. 5.6.8).

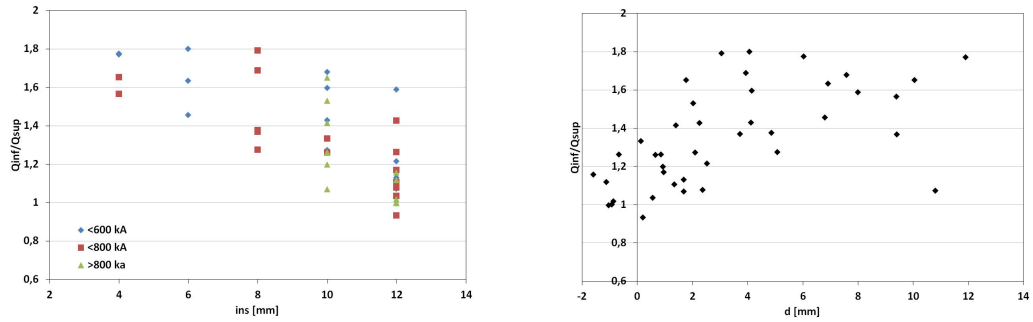

(a) Toroidal asymmetry vs ins (b) Toroidal asymmetry vs d

Figure 5.6.24: Dependences of the toroidal asymmetry

An heat flux asymmetry along the toroidal direction has also been noticed and investigated, as shown in fig. 5.6.24 and fig. 5.6.25, where the electron and ion side are averaged together. A dependence has been found on limiter

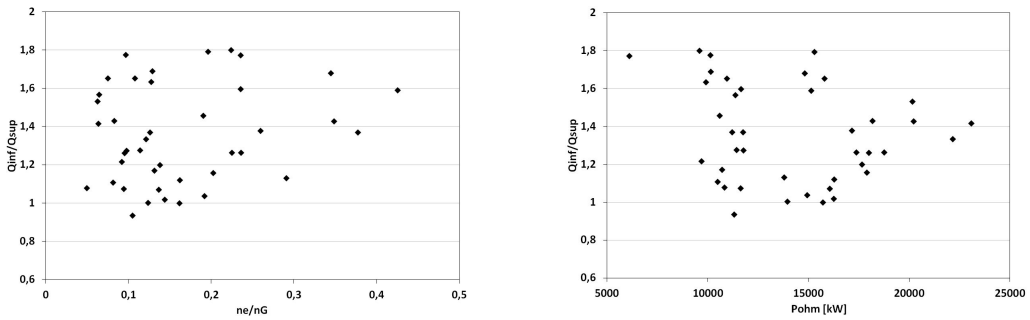

(a) Toroidal asymmetry vs n_e/n_G (b) Toroidal asymmetry vs P_{ohm}

Figure 5.6.25: Non influent parameters for toroidal asymmetry

insertion and plasma distance, while it does not correlate with the density or the ohmic power. For these reasons, this asymmetry is probably to be explained with geometrical factors instead of physical ones, allowing to think to a slight tilt on the position of the limiter. If this is the case, this asymmetry would be reduced to the minimum when the largest interaction takes place (high ins, small d) becuase the plasma interacts with almost all the surface, while it would increase as the distance is increased because then one side would be closer to the plasma than the other, having a much higher relative interaction. This assumption is also acceptable from an experimental point of view as the sample is fixed at the end of the arm a remote handling tool that can in theory allow such a tilt.

Fig. 5.6.26 shows the heat toroidal asymmetry plotted against the rescaled distance, showing an information loss (compared to fig. 5.6.24b) also in this context.

The comparison between the two graphites has been completed consider-

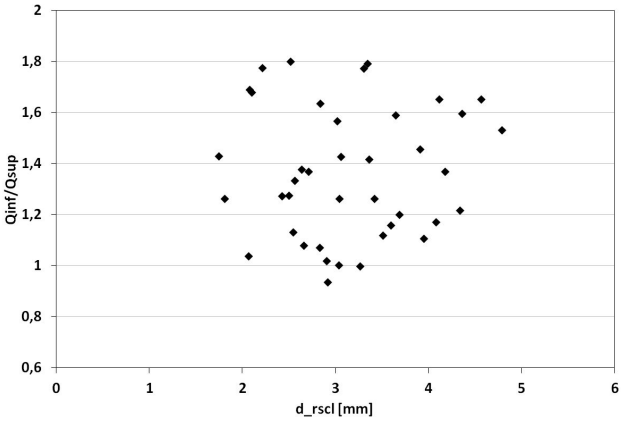

Figure 5.6.26: Toroidal asymmetry vs d rescaled

ing the impinging heat loads normalized to the total ohmic power, as shown in fig. 5.6.27. The two samples show an analogous behaviour but graphite IG-15 has the lowest values, highlighting the difference in conductivity between the them. Combining this analysis with the one done for the heat decay length, the information that can be obtained is that, even if both graphites are isotropic, a different conductivity enhances only the heat transport along the limiter depth while it does not seem to modify the behaviour of the heat distribution on the surface.

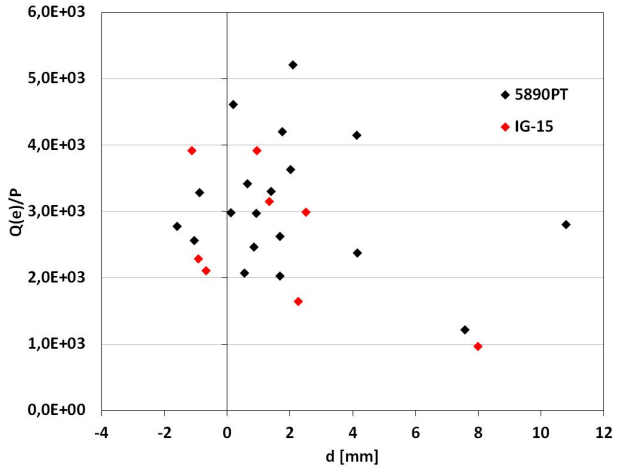

Figure 5.6.27: Q(e)/P_{ohm} vs d for the two graphites

5.7 Conclusions

One of the main issues concerning next generation fusion devices is the control of the intense heat loads that are deposited on the first wall. The heat flux properties of the plasma edge have been studied during an exprimental campaign at RFX-mod measuring the heat distribution on graphite samples exposed to a RFP deuterium plasma in a limiter configuration by means of an infrared camera. These samples were mounted on a remote handling tool so they could be inserted up to 12 mm closer to the plasma than the rest of the first wall. They were also made of two different graphites: RFX-mod standard and one with enhanced heat conductivity.

The conversion from temperature to heat flux is not direct and has been tackled numerically. A widely diffused code, THEODOR, has been used for these calculations while the alternative software TtoP3D has been developed

to overcome some limits of THEODOR relevant to the case of study, as the bidimensional treatment of the heat analysis. The codes have been benchmarked giving an agreement within the 10% for the heat fluxes computed from the same temperature map. Such heat fluxes have been imposed on a model of the sample in ANSYS to evaluate how the resulting temperature would compare to the measured one. The results show a good agreement between resulting computed temperature and experimental ones, with the newly developed 3D code TtoP3D having a discrepancy from the camera temperature of less than the 2%, comparable to the instrumental accuracy.

Magnetical reconstruction routines have been used to estimate the plasma position during the discharges in order to correlate it with the heat fluxes calculated on the sample. Some limits of the application of these routines to the present case have been discussed and tackled, obtaining relevant information for the rest of the analysis. An important result highlighted in this part is a strong indication that the plasma and the samples are in contact only when the samples are inserted the most, suggesting that the plasma is actually limited only in these conditions while it is a normal circular plasma for low samples insertions.

The heat distribution on the samples has been analysed and found to decay exponentially along the radial distance from the plasma edge, allowing the measurement of the heat decay length for the first time in an RFP, both for the electron and the ion drift sides. Two different values for λ_q were found: for deep insertions ($10 \div 12$ mm) $\lambda_q(e) = 1.69 \pm 0.16$ mm and $\lambda_q(i) =$

2.44 ± 0.27 mm, while for smaller insertions ($4 \div 8$ mm) $\lambda_q(e) = 1.31 \pm 0.20$ mm and $\lambda_q(i) = 1.64 \pm 0.46$ mm. This distinction seems to be related only to the limiter insertion and is interpreted as confirming the hypothesis that the samples are acting as limiters only when inserted the most. λ_q is also found to increase with plasma current and input ohmic power while it seems independent of density and impinging heat flux.

The correlation between heat fluxes and plasma parameters has been explored, showing a dependence on the plasma current, input ohmic power and an inverse dependence on the density and the limiter insertion. This last shows two separate trends for different insertions, confirming the results and considerations done for the heat decay length. The analysis of heat flux asymmetries highlighted the presence of superthermal electrons resulting in a heat flux on the electron drift side up to three times higher than the one on the ion side. Also a toroidal asymmetry was measured, but its only dependence on the distance from the plasma suggests that it can be related to a slight tilt in the positioning of the sample and not to other physical effects.

Finally the two different graphites have been compared. The one with enhanced heat condictivity has shown reduced heat deposition on the surface when compared to the standard RFX-mod graphite under the same external conditions. The heat diffusion on the surface has been found to be negligible due to the short time of the discharge that does not allow an appreciable diffusion.

Conclusions

One of the most relevant issues for future fusion reactors is how the plasma interacts with the first wall of the machine, in particular from the point of view of particle and power exhaust. This is a broad field of research inside which three topics have been studied in the framework of this thesis:

- numerical simulations for advanced divertor geometries;
- experimental analysis of plasma-wall interactions of tungsten covered samples exposed to the plasma compared to present graphite;
- experimental measurement of heat flux properties of the plasma edge of the RFP.

Innovative divertor geometries are required because the heat loads foreseen in a fusion reactor are too high for divertors now in use. A possible alternative is the snowflake configuration which allows lower heat loads and smaller power densities on the divertor targets. This configuration is obtained modifying the magnetic field generated by the magnetic divertor coils in order to obtain a second order null of the poloidal magnetic field on the X-point.

Since the snowflake is an unstable configuration and is difficult to realize from a technological point of view, a quasi-snowflake has been studied and compared to a standard X-point divertor in the context of preliminary studies for the proposed FAST tokamak. Numerical simulations have been performed with the well known EDGE2D/EIRENE code that allows a multi-fluid bidimensional treatment of the plasma edge combined with a kinetic description of neutrals dynamics.

The comparison between the quasi-snowflake configuration and the standard divertor has been carried out varying plasma density, recycling coefficient and Ne impurity puffing. Results show power load mitigation up to 60% and increase of volume losses up to 40% with respect to the standard divertor, confirming the snowflake configuration as a viable improvement for power exhaust handling. Ne puffing does not show the expected benefits as it does not contribute to a power mitigation on the target, the reason in probably in the low input flux set for cases studied.

The activity carried out at RFX-mod was devoted to the analysis of plasma-wall interactions with visible and infrared cameras. The visible camera has been used to investigate surface properties of graphite and tungsten samples exposed to the plasma, in the context of possible machine upgrades. Tungsten is being widely studied because is the material forseen for a large part of the ITER first wall due to its significant capabilities of handling the plasma power and particle exhaust.

A good indicator of the intensity of plasma-wall interactions is the H_α emission of neutral atoms extracted from the surface materials, which is the quantity that can be measured by the visible camera and that is used to evaluate the relative recycling properties of tungsten and graphite. A method has been introduced to properly take into account all components of the light intensity measured by the camera, overcoming the problem of the high reflectivity of tungsten.

The samples exposed on the inner side of the torus were found to undergo more intense interactions than those on the outer side. Comparing the two materials, tungsten is found to be up to four times more interacting than graphite, meaning a larger neutrals emission from the tungsten surface than from graphite. This behaviour is in contrast with what is reported in literature and the reason of this discrepancy has not been understood yet. It is possibly due to intense and localized interactions that often caused layer delamination and material ablation from the surface, with consequent more intense light emission from those atoms that could interfere with the normal neutrals emission. This work could be improved by testing the goodness of the method used for subtracting non-local emission in controlled conditions, for example in a laboratory where only light reflections from known sources are to be measured; other samples could also be exposed to the plasma in order to extend the database.

Finally, a method is presented to estimate the average length travelled by the neutrals in the direction parallel to the wall. This calculation could be

extended to the entire database of images obtained during this campaign in order to get to a mean value with statistical meaning and correlations with other plasma parameters. It will be also possible to compare the results with numerical simulations of neutrals dynamics.

The last topic dealt with the investigation of heat flux properties of the plasma edge. An infrared camera was used to measure the heat deposition on graphite samples inserted in limiter configuration in an RFP plasma. These samples were made of two different graphites, RFX-mod standard graphite and one with enhanced heat condictivity, and could be inserted up to 12 mm closer to the plasma than the rest of the first wall.

The analysis required several steps such as camera set up and calibration, solution of the inverse heat conduction problem, estimation of plasma position and its correlation to the interactions with the samples, extrapolation of heat profiles and correlation of data with plasma parameters.

The inverse heat conduction problem has been solved numerically by the code THEODOR. A new code, TtoP3D, has been developed to tackle the same problem in a 3D geometry. The codes have been benchmarked against one another showing a good agreement on the heat fluxes computed from the same temperature map. Such heat fluxes have been imposed on a model of the sample in ANSYS and the resulting temperature has been compared to the one measured by the IR camera. The agreement is good but it is notable that the newly developed 3D code TtoP3D shows a a discrepancy from the

camera temperature of less than the 2%. This comparison between the two codes could be extended to a larger variety of external conditions to confirm the relative agreement; TtoP3D could be used with a real geometry mesh in order to exploit all of its possibilities.

Plasma position has been estimated using magnetical reconstruction routines, taking into account their limits in the considered case. A strong indication emerged that the plasma and the samples are in contact only when the samples are inserted the most, suggesting that the plasma is actually limited only in these conditions while it is a normal circular plasma for low samples insertions.

The heat distribution on the samples has been analysed and found to decay exponentially along the radial distance from the plasma edge, allowing the measurement of the heat decay length for the first time in an RFP, both for the electron and the ion drift sides. Two different values for λ_q were found for each side depending on the limiter insertion, and thus confirming that the samples are acting as limiters only when inserted the most: for deep insertions ($10 \div 12$ mm) $\lambda_q(e) = 1.69 \pm 0.16$ mm and $\lambda_q(i) = 2.44 \pm 0.27$ mm, while for smaller insertions ($4 \div 8$ mm) $\lambda_q(e) = 1.31 \pm 0.20$ mm and $\lambda_q(i) = 1.64 \pm 0.46$ mm. λ_q is also found to increase with plasma current and input ohmic power while it seems independent of density and incident heat flux.

The analysis of heat fluxes confirmed the presence of superthermal electrons, causing a poloidal asymmetry of the heat flux at low density, that

resulted up to three times larger on the electron drift side than on the ion side. The dependence of the heat flux with the limiter insertion showed once again the two separate trends discussed for the decay length.

Finally the comparison between the two different graphites shows that an enhanced heat conductivity effectively results in a reduced heat load on the surface of the sample.

Future work on this topic could be done by extending the available database with optimized plasma discharges and limiter conditions to have better statistics for correlations with plasma parameters. Other edge diagnostics as Langmuir probes and electron energy analyzers could be used together with the IR camera to increase the parameters analyzed and compared during the discharges.

Bibliography

[1] Chen, F. "Plasma Physics, Introduction to Plasma Physics and Controlled Fusion, Vol. 1." (1984): 13.

[2] Goldston, Robert J., and Paul Harding Rutherford. Introduction to plasma physics. CRC Press, 1995.

[3] Freidberg, Jeffrey P. Plasma physics and fusion energy. Cambridge university press, 2007.

[4] Lawson, John D. "Some criteria for a power producing thermonuclear reactor." Proceedings of the Physical Society. Section B 70.1 (1957): 6.

[5] Wesson, John, and David J. Campbell. Tokamaks. No. 118. Oxford University Press, 2004.

[6] Artsimovich, L. A. "Tokamak devices." Nuclear Fusion 12.2 (1972): 215.

[7] Taylor, J. Brian. "Relaxation of toroidal plasma and generation of reverse magnetic fields." Physical Review Letters 33.19 (1974): 1139.

[8] Ortolani, Sergio, and Dalton D. Schnack. Magnetohydrodynamics of plasma relaxation. Vol. 156. Singapore: World Scientific, 1993.

[9] Boozer, Allen H. "What is a stellarator?." Physics of Plasmas (1994-present) 5.5 (1998): 1647-1655.

[10] http://www.pppl.gov/about/history

[11] Baker, W., et al. "Design of a new toroidal shell and support structure for RFX." Fusion engineering and design 63 (2002): 461-466.

[12] Sonato, P., et al. "Machine modification for active MHD control in RFX." Fusion engineering and design 66 (2003): 161-168.

[13] Rostagni, G. "RFX: an expected step in RFP research." Fusion Engineering and Design 25.4 (1995): 301-313.

[14] https://www.iter.org/

[15] Campbell, D. J. "The physics of the international thermonuclear experimental reactor FEAT." Physics of Plasmas (1994-present) 8.5 (2001): 2041-2049.

[16] Fundamenski, Wojciech. Power exhaust in fusion plasmas. Cambridge University Press, 2010.

[17] Bohm, David. "Qualitative description of the arc plasma in a magnetic field." The Characteristics of Electrical Discharges in Magnetic Fields. A. Guthrie and RK Wakerling, editors. McGraw-Hill, NY (1949).

[18] Ingraham, J. C., et al. "Energetic electron measurements in the edge of a reversed-field pinch." Physics of Fluids B: Plasma Physics (1989-1993) 2.1 (1990): 143-159.

[19] Stoneking, Matthew Randall. Fast electron generation and transport in a turbulent, magnetized plasma. Diss. University of Wisconsin, Madison, 1994.

[20] Yagi, Yasuyuki, et al. "Measurement of fast electron velocity distribution function in a reversed field pinch plasma." Japanese journal of applied physics 35.7R (1996): 4064.

[21] Yagi, Y., et al. "Measurement of superthermal electron flow and temperature in a reversed-field pinch experiment by an electrostatic electron energy analyser." Plasma physics and controlled fusion 39.11 (1997): 1915.

[22] Yagi, Yasuyuki, et al. "Movable limiter experiment on tpe-1rm15 reversed field pinch machine." Journal of Nuclear Materials 162 (1989): 702-709.

[23] Antoni, V., et al. "Energy flux investigation in the outer region of the ETA BETA II experiment." Plasma physics and controlled fusion 34.5 (1992): 699.

[24] Antoni, V., et al. "Stochastic magnetic and ambipolar electric fields in the plasma edge region of RFX." Nuclear fusion 36.4 (1996): 435.

[25] Martines, E., R. Bartiromo, and M. Shoucri. "On the origin of superthermal electrons in the edge of RFP plasmas." Plasma physics and controlled fusion 44.4 (2002): 439.

[26] Jacobson, Abram R., and Ronald W. Moses. "Nonlocal dc electrical conductivity of a Lorentz plasma in a stochastic magnetic field." Physical Review A 29.6 (1984): 3335.

[27] Giruzzi, Gerardo, and E. Martines. "Kinetic modeling of fast electron dynamics and self-consistent magnetic fields in a reversed field pinch." Physics of Plasmas (1994-present) 1.8 (1994): 2653-2660.

[28] Ji H, Almagri A F, Prager S C and Sarff J S 1994 Phys. Rev. Lett. 73 668

[29] Garzotti, L., et al. "Investigation of electron-distribution function and dynamo mechanisms in a reversed-field pinch by analysis of hydrogen-pellet deflection." Physical review letters 84.24 (2000): 5532.

[30] Yoshida, Z., A. Hasegawa, and M. Wakatani. "Production of superthermal electrons and ion cyclotron waves in a reversed-field-pinch plasma." Physics of Fluids B: Plasma Physics (1989-1993) 5.9 (1993): 3261-3266.

[31] Erba, M., et al. "Magnetic reconnection as a mechanism for the generation of fast electrons." Nuclear fusion 33.10 (1993): 1577.

[32] Ryutov, D. D. "Geometrical properties of a “snowflake” divertor." Physics of Plasmas (1994-present) 14.6 (2007): 064502.

[33] Umansky, M. V., et al. "Analysis of geometric variations in high-power tokamak divertors." Nuclear Fusion 49.7 (2009): 075005.

[34] Pizzuto, A., et al. "The Fusion Advanced Studies Torus (FAST): a proposal for an ITER satellite facility in support of the development of fusion energy." Nuclear Fusion 50.9 (2010): 095005.

[35] Ridolfini, V. Pericoli, et al. "Simulations of the SOL plasma for FAST, a proposed ITER satellite tokamak." Fusion Engineering and Design 86.9 (2011): 1757-1761.

[36] Ridolfini, V. Pericoli, et al. "Comparative study of a conventional and snowflake divertor for the FAST (Fusion Advanced Studies Torus) tokamak." Journal of Nuclear Materials 438 (2013): S414-S417.

[37] http://www.fusione.enea.it/PROJECTS/FAST/index.html.en

[38] Viola, B., et al. "Preliminary Comparison of the Conventional and Quasi-Snowflake Divertor Configurations with the 2D Code EDGE2D/EIRENE in the FAST Tokamak." Contributions to Plasma Physics 54.4-6 (2014): 459-463.

[39] Ridolfini, V. Pericoli, et al. "Preliminary 2D code simulation of the quasi-snowflake divertor configuration in the FAST tokamak." Fusion Engineering and Design 88.9 (2013): 1677-1681.

[40] Coda, S. T. T. T. "Overview of recent and current research on the TCV tokamak." Nuclear Fusion 53.EPFL-ARTICLE-191260 (2013): 104011.

[41] Hill, D. N. "DIII-D research towards resolving key issues for ITER and steady-state tokamaks." Nuclear Fusion 53.10 (2013): 104001.

[42] S. A. Sabbagh and NSTX Team, “Overview of physics results from the conclusive operation of the National Spherical Torus Experiment,” Nucl. Fusion 53, 104007 (2013).

[43] Zagórski, R., and H. Gerhauser. "Numerical Modelling of Marfe Phenomena in TEXTOR Tokamak." Physica Scripta 70.2-3 (2004): 173.

[44] Zagórski, R., et al. "Modelling with TECXY code of lithium limiter experiments on FTU." Czechoslovak Journal of Physics 56.2 (2006): B182-B184.

[45] Zagórski, R., J. P. Gunn, and I. Nanobashvili. "Numerical investigations of edge plasma flows in the Tore Supra tokamak." Plasma Physics and Controlled Fusion 49.7 (2007): S97.

[46] Pełka, G., et al. "TECXY Code Simulation of Snowflake Divertor Configuration in DEMO Reactor." Contributions to Plasma Physics 54.4-6 (2014): 464-468.

[47] Calabrò, G., et al. "EAST alternative magnetic configurations: modelling and first experiments." Nuclear Fusion 55.8 (2015): 083005.

[48] Simonini, R., et al. "Models and Numerics in the Multi-Fluid 2-D Edge Plasma Code EDGE2D/U." Contributions to Plasma Physics 34.2-3 (1994): 368-373.

[49] Taroni, A., et al. "The Multi-Fluid Codes Edgeid and Edge2D: Models and Results." Contributions to plasma Physics 32.3-4 (1992): 438-443.

[50] Coster, D. P., et al. "Benchmarking Tokamak edge modelling codes." Journal of nuclear materials 337 (2005): 366-370.

[51] Reiter, D. "Randschicht-Konfiguration von Tokamaks. Entwicklung und Anwendung stochastischer Modelle zur Beschreibung des Neutralgas-transports." (1984).

[52] Reiter, D. "The EIRENE code user manual." (2005).

[53] Norris, James R. "Markov chains." (No. 2008). Cambridge university press, 1998.

[54] Loarte, Alberto. "Effects of divertor geometry on tokamak plasmas." Plasma physics and controlled fusion 43.6 (2001): R183.

[55] Pitts, R. A., et al. "Physics basis and design of the ITER plasma-facing components." Journal of Nuclear Materials 415.1 (2011): S957-S964.

[56] Roth, Joachim, et al. "Recent analysis of key plasma wall interactions issues for ITER." Journal of Nuclear Materials 390 (2009): 1-9.

[57] Brezinsek, S., et al. "Fuel retention studies with the ITER-like wall in JET." Nuclear Fusion 53.8 (2013): 083023.

[58] Mayer, M., et al. "Carbon balance and deuterium inventory from a carbon dominated to a full tungsten ASDEX Upgrade." Journal of Nuclear Materials 390 (2009): 538-543.

[59] Sugiyama, K., et al. "Deuterium inventory in the full-tungsten divertor of ASDEX Upgrade." Nuclear Fusion 50.3 (2010): 035001.

[60] Smith, Warren J. Modern optical engineering. Tata McGraw-Hill Education, 1966.

[61] Rowan-Robinson, Michael. Night vision: exploring the infrared universe. Cambridge University Press, 2013.

[62] Kirchhoff, Gustav. "Ueber das Verhältniss zwischen dem Emissionsvermögen und dem Absorptionsvermögen der Körper für Wärme und Licht." Annalen der Physik 185.2 (1860): 275-301.

[63] Planck, M. K. E. L. "The theory of heat radiation, translated by M." Masius, P. Blackiston's Son & Co, Philadelphia, reprinted by Kessinger (1914).

[64] Wolfe, William L., and George J. Zissis. "The infrared handbook." Arlington: Office of Naval Research, Department of the Navy, 1978, edited by Wolfe, William L.; Zissis, George J. 1 (1978).

[65] Madding, Robert P. Thermographic Instruments and systems. University of Wisconsin-Extension, Department of Engineering & Applied Science, 1979.

[66] Wolfe, William L. Handbook of military infrared technology. Michigan Univ Ann Arbor, 1965.

[67] Bramson, Mikael Abramovic. "Infrared radiation. A handbook for applications." Optical Physics and Engineering, New York: Plenum Press, 1968 1 (1968).

[68] Hadamard, Jacques. "Sur les problèmes aux dérivées partielles et leur signification physique." Princeton university bulletin 13.49-52 (1902): 28.

[69] Eich, T., et al. "ELM resolved energy distribution studies in the JET MKII Gas-Box divertor using infra-red thermography." Plasma Physics and Controlled Fusion 49.5 (2007): 573.

[70] Gardarein, J-L., et al. "Thermal quadrupoles approach for two-dimensional heat flux estimation using infrared and thermocouple measurements on the JET tokamak." International Journal of Thermal Sciences 48.1 (2009): 1-13.

[71] Herrmann, A., and ASDEX Upgrade Team. "Limitations for divertor heat flux calculations of fast events in tokamaks." 28th EPS Conference on Controlled Fusion and Plasma Physics. European Physical Society, 2001.

[72] Riccardo, V., W. Fundamenski, and G. F. Matthews. "Reconstruction of power deposition profiles using JET MkIIGB thermocouple data for

ELMy H-mode plasmas." Plasma physics and controlled fusion 43.7 (2001): 881.

[73] Zanca, Paolo, and David Terranova. "Reconstruction of the magnetic perturbation in a toroidal reversed field pinch." Plasma physics and controlled fusion 46.7 (2004): 1115.

[74] FC-NT-65-rev3

[75] FC-NT-59

[76] FC-NT-81

[77] Eich, T., et al. "Inter-ELM power decay length for JET and ASDEX Upgrade: measurement and comparison with heuristic drift-based model." Physical Review Letters 107.21 (2011): 215001.

[78] Arnoux, G., et al. "Scrape-off layer properties of ITER-like limiter start-up plasmas in JET." Nuclear Fusion 53.7 (2013): 073016.

[79] Carpentier, S., et al. "Study of heat flux deposition on the limiter of the Tore Supra tokamak." Journal of Nuclear Materials 390 (2009): 955-958.

[80] Vondrácek, P., et al. "Parallel Heat Flux Decay Length Study in the COMPASS Tokamak Using MWIR and LWIR Cameras." WDS '14 Proceedings of Contrib. Papers - Physics, 227-232, 2014